

Katrin Koren, BSc

**Towards Entirely Solution-processed
Flexible Organic Light Emitting Diodes:
Solution-based Processes for Anode
and Cathode Formation**

MASTER THESIS

For obtaining the academic degree
Diplom-Ingenieurin

Master Programme of
Technical Physics



Graz University of Technology

Supervisor:

Ao.Univ.-Prof. Dipl.-Ing. Dr.techn. Emil J. W. List-Kratochvil

Institute of Solid State Physics

in cooperation with NanoTecCenter Weiz Forschungsgesellschaft mbH

Graz, Mai 2014

Deutsche Fassung:

Beschluss der Curricula-Kommission für Bachelor-, Master- und Diplomstudien vom 10.11.2008

Genehmigung des Senates am 1.12.2008

EIDESSTATTLICHE ERKLÄRUNG

Ich erkläre an Eides statt, dass ich die vorliegende Arbeit selbstständig verfasst, andere als die angegebenen Quellen/Hilfsmittel nicht benutzt, und die den benutzten Quellen wörtlich und inhaltlich entnommenen Stellen als solche kenntlich gemacht habe.

Graz, am

(Unterschrift)

..

Englische Fassung:

STATUTORY DECLARATION

I declare that I have authored this thesis independently, that I have not used other than the declared sources / resources, and that I have explicitly marked all material which has been quoted either literally or by content from the used sources.

date

(signature)

..

ABSTRACT

Now that organic light emitting diodes (OLEDs) are on their way to enter the market at a grand scale, processing issues get extremely important. All of them have one thing in common: reducing cost. Polymer based organic semiconductors are widely accepted due to the advantage of solution based processing, yet when it comes to actual device manufacturing solution based electrode processing needs to be taken into account. Therefore solution-based electrode deposition as well as the according interlayer processes and materials, necessary for a good energy level alignment, need to be developed. Such an approach will pave the way for large area and industrial scale fabrication of OLEDs on flexible substrates. This work focuses on the development of solution-based anode and cathode deposition processes for OLEDs.

The first part of this thesis deals with an ITO free, low cost approach for an anode deposition process. Instead of ITO, which not only suffers from high processing costs but may also be regarded a rare material, inkjet printed metal grids are used in combination with highly conducting PEDOT:PSS. Therefore an so called honeycomb structure was designed and deposited using inkjet printing. Here the line width and honeycomb dimensions have been optimized to ensure a proper sheet resistance, comparable to ITO along with a as high as possible transparency. At the same time the structure was optimized for minimal surface roughness. To ensure optimal performance the printed silver grid was embedded into a transparent photo-resist. Devices were tested and optimized following the development of the anode deposition process.

The second part of this thesis focuses on solution processed materials for the low work function electrode side, demanding good electron injection capabilities. The chosen approach was based on using cesium stearate as the interlayer. At first a basis analysis of solubility and film formation study was done using an AFM as well as an optical microscope. The influence of cesium stearate on the device performance was first tested using a commercially available polymer, in single and multilayer device assemblies. For obtaining a better understanding of the interface behaviour of cesium stearate, UPS measurements have been performed and analysed. Finally, cesium stearate was combined with an inkjet printed top cathode using a standard polymer material again.

KURZFASSUNG

Nachdem Organische Leuchtdioden (OLED) den Sprung zur Anwendung geschafft haben, erlangen prozessrelevante Themen, fokussierend auf einer Reduktion der Kosten, zunehmend große Relevanz. Die Lösungsprozessierung stellt einen großen Vorteil von polymerbasierten organischen Halbleitermaterialien dar, wenn es um die der Bauteilfabrikation geht, ist aber auch die lösungsbasierte Elektrodenherstellung zu berücksichtigen. Deshalb müssen lösungsbasierte Prozesse zur Elektrodenfabrikation, sowie passende Zwischenschichten und Materialien, die notwendig für eine gute Anpassung der entsprechenden Energieniveaus sind, entwickelt werden. Mit Hilfe solcher Prozesse wird eine großflächige OLED Fabrikation auf flexiblen Substraten im industriellen Maßstab möglich.

Der erste Teil dieser Arbeit beschäftigt sich mit einer alternativen kostengünstigen Anodenfabrikation ohne die Verwendung von ITO (Indium Zinn Oxid). An Stelle von ITO, das kostenintensiv in der Herstellung und aufgrund der limitierten Indium Ressourcen nur beschränkt verfügbar ist, wurden gedruckte Metallgitter in Kombination mit extrem leitfähigem PEDOT:PSS verwendet. Es wurde eine Bienenwabenartige Struktur entworfen und mittels Tintenstrahldruckes aufgebracht. Dabei wurden die Gitterstrukturen derart optimiert, dass ein geringer Flächenwiderstand, vergleichbar mit ITO, sowie eine gute Transparenz erreicht werden konnten. Zusätzlich wurde Bedacht darauf genommen, durch entsprechende Strukturoptimierung, die Oberflächenrauigkeit zu reduziert. Dazu wurden die Silbergitter in einem transparenten Photolack eingebettet. Außerdem wurden die Bauteile getestet und bezüglich des Anodenfabrikationsprozesses optimiert.

Der zweite Teil der Arbeit beschäftigte sich mit lösungsprozessierten Materialien für die Kathodenfabrikation, wobei kathodenseitig eine geringe Austrittsarbeit notwendig ist, um eine gute Elektroneninjektion zu ermöglichen. Im gewählten Ansatz wurde Caesiumstearat als Zwischenschicht verwendet. Zunächst wurde mit Hilfe von AFM und optischer Mikroskopie die Löslichkeit und Filmformation von Caesiumstearat charakterisiert, sowie der Einfluss von Caesiumstearat auf die Leistung von Ein- und Mehrschichtbauteilen untersucht. Zum besseren Verständnis des Zwischenschichtverhaltens von Caesiumstearat wurden PES Messungen durchgeführt und analysiert. Abschließend, wurde Caesiumstearat in Kombination mit tintenstrahldruckten Silberkathoden prozessiert.

Contents

1	INTRODUCTION	1
2	FUNDAMENTALS	2
2.1	Organic semiconductors	2
2.1.1	Small molecules	4
2.1.2	Conjugated polymers	5
2.1.3	Fundamental excitations	5
2.1.3.1	Polarons	6
2.1.3.2	Excitons	6
2.1.4	Transition between electronic states in organic semiconductors	8
2.1.4.1	Absorption and the Franck-Condon-Principle	8
2.1.4.2	Fluorescence	9
2.1.4.3	Phosphorescence	9
2.1.4.4	Photoluminescence and Electroluminescence	9
2.2	Organic light emitting diodes	10
2.2.1	Architecture	11
2.2.2	Working principle	11
2.2.3	Charge injection and charge transport	12
2.2.4	Energy level alignment at the interface	14
3	EXPERIMENT METHODOLOGY	16
3.1	Device fabrication	16
3.1.1	Substrate preparation	16
3.1.2	Layer deposition techniques and used facilities	18
3.1.2.1	Spin coating	18
3.1.2.2	Photolithography	18
3.1.2.3	Vacuum deposition	20
3.1.2.4	Inkjet printing	21
3.1.3	Reference device assembly	22
3.2	Device characterization	25
3.2.1	Current density-voltage-luminescence characterization	25
3.2.2	Electroluminescence spectra	26
3.3	Interface Investigations	27
3.3.1	Photoelectron spectroscopy	27
4	GRID SUPPORTED ANODE UTILIZED IN SINGLE AND MULTILAYER DEVICES	30
4.1	Introduction and Grid design	30

4.2	Photolithographic grids	33
4.2.1	Fabrication	33
4.2.2	Organic light emitting diodes utilizing grid-PEDOT:PSS double anode . .	33
4.3	Printed grids	38
4.3.1	Fabrication	38
4.3.2	Grid investigations	39
4.4	Embedding the silver grid lines	41
4.4.1	Introduction and used material	41
4.4.2	Results	42
4.5	Conclusion	46
5	CESIUM STEARATE AS SPIN COATED CATHODE INTERLAYER	47
5.1	Introduction and layer formation	47
5.2	Device performance of a polymer light emitting diode utilizing cesium stearate aluminum (evaporated) double cathode	51
5.2.1	Device fabrication	51
5.2.2	Device performance of single layer and multilayer devices	53
5.2.3	Comparing the device efficiencies	57
5.3	Device performance of a dendrimer based light emitting diode utilizing cesium stearate aluminum (evaporated) double cathode	60
5.3.1	Introduction to dendrimer materials	60
5.3.2	Photophysical properties and device performance for PYCAB	61
5.3.3	Device performance of multilayer devices	62
5.3.4	UPS studies on PYCAB cesium stearate interface	66
5.4	Influence of cesium stearate on polyfluorene color stability	70
5.4.1	Different polyfluorene materials and there properties	70
5.4.2	Device performance for the different polymers utilizing cesium stearate aluminum (evaporated) double cathode	71
5.5	Conclusion	76
6	INKJET PRINTED TOP CATHODE	78
6.1	Layer formation of the silver ink on top of the device stack	79
6.2	Device performance utilizing a fully solution processed bilayer top cathode with cesium stearate and silver	81
6.2.1	Influence of different curing conditions	81
6.2.2	Reduced solvent penetration of the active layer using a smaller top cathode patterning	84
6.3	Conclusion	85
7	CONCLUSION	86

1 INTRODUCTION

More than 25 years passed since Tang and Van Slyke [63] reported the first organic light emitting diode based on small molecules. Only some years later, Friend et al. reported on the electroluminescence of polymers [12]. Back then, a large academic as well as industrial interest in organic semiconductors has started and is still going on. Reasons for this large interest are the good material properties (high brightness, good contrast ratio) of organic semiconductors and the easy manufacturing in the case of organic polymers (solution processable). Nevertheless, regarding display manufacturing, liquid crystal displays are still the dominating technology today. The two main challenges in order to enter the large area low cost market up to industrial level [10] are the encapsulation of the devices (in order to guarantee a long lifetime) as well as the optimization of the electrode materials. Besides these, also the lagging efficiencies and lifetimes of solution processed active layers, especially blue emitters, are a big issue. The scope of this thesis is focused on the fabrication and optimization of low cost electrodes.

After a short introduction to the basic theoretical concepts in chapter two, chapter three summarizes the experimental methodology of the device fabrication and characterization. A solution processed low cost alternative for ITO consisting of a silver honeycomb grid covered with spin coated PEDOT:PSS is presented in chapter four. OLEDs using lithographically structured silver in combination with PEDOT:PSS as anode structure are demonstrated to exhibit good device performances. In order to use a low cost fabrication process, the silver grid lines are also inkjet printed on top of flexible and rigid carrier substrates. The anode bilayer is then further improved in terms of surface roughness by embedding the inkjet printed silver lines into a transparent photo resist. Chapter five focuses on the modification of the cathode. By using a cesium stearate interlayer, the device efficiencies are demonstrated to improve significantly. The devices incorporating the cesium stearate interlayer are then analyzed in terms of layer formation. The electrical interfaces were then investigated using UPS measurements. Moreover, cesium stearate was also combined with a new dendrimer material. Besides this, the influence of cesium stearate on the device performance of polyfluorene devices is reported. Finally chapter six combines spin coated cesium stearate with an inkjet printed silver top cathode and the corresponding device results are reported.

2 FUNDAMENTALS

Within this chapter, the fundamentals of organic semiconductors are explained shortly. Moreover the transition between electronic states and here especially optical transitions, which are important in OLEDs are discussed. Finally, an overview on the architecture and working principle of OLEDs is given.

2.1 Organic semiconductors

Basically, the term organic semiconductors is self-explanatory. The term organic is generally defined as an umbrella term for all materials that incorporate carbon. The semiconducting properties of some organic materials are the result of a specific structure they have. In order to explain this in more detail, one first needs to take a closer look on the electronic structure of carbon. The location of carbon in the periodic table explains the electronic structure. Carbon consists of 4 electrons in the outermost shell and 6 electrons all together. The electron configuration of the ground state with two unpaired electrons in the 2p orbital is depicted on the left of figure 2.2. As the difference in energy between the 2s and the 2p orbital is relatively small, one electron from the 2s orbital can be promoted into the 2p orbital, for the excited configuration 4 energetically equal orbitals are available for the formation of chemical bonds. The electron configuration for this case is depicted in figure 2.2 (second configuration from the left side). This situation in the orbital picture is illustrated on the left side of figure 2.1. In this figure also the concept of hybridization is introduced. In 1931 Pauling first formulated this theory [54]. Depending on the number of involved p orbitals, sp, sp² and sp³ hybrid orbitals can be formed. The electronic structure of these different hybridizations are depicted in figure 2.2.

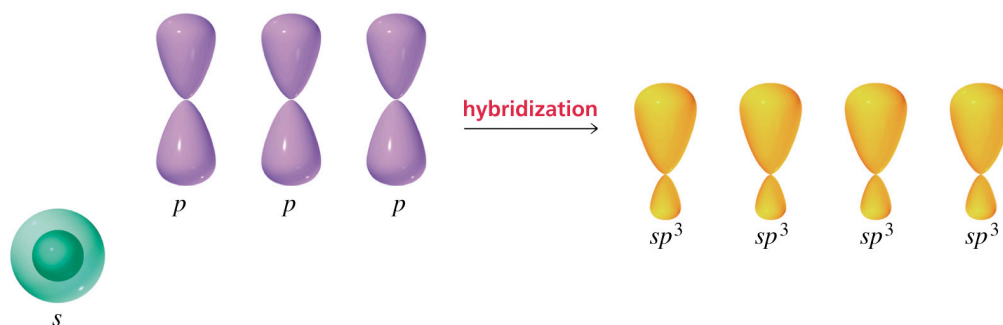


Figure 2.1: Visualization for the formation of four sp^3 orbitals upon hybridization. Taken from [2].

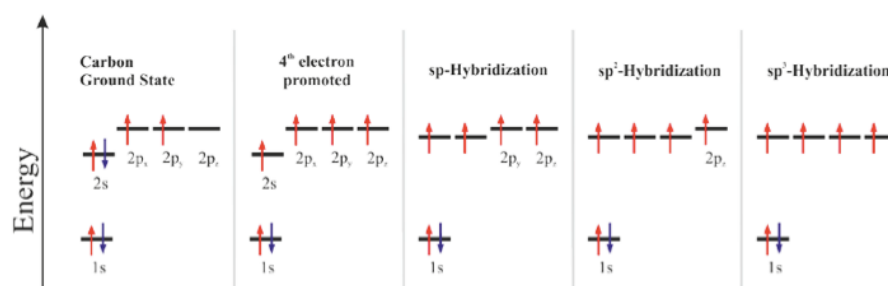


Figure 2.2: Energy level diagrams of carbon: ground state, one electron promoted, sp -hybridized, sp^2 -hybridized and sp^3 -hybridized (from left to right). Taken from [67].

For carbon, a sp^2 hybridization results in three sp^2 orbitals and one p_z orbital. This is for one single carbon atom depicted in figure 2.3. On the right side of figure 2.3, the binding behavior for the case of ethylene is depicted. There also the different binding behavior of the sp^2 and the p_z is obvious when looking at the carbon-carbon double bond. The sp^2 orbitals, which are energetically equal, form σ bonds. In general, σ bonds are formed by the overlap of plane orbitals where individual orbitals are located in the same plane. These bonds are very strong chemical bonds. In contrast, π bonds are formed when parallel orbitals overlap. In the case of sp^2 hybridized carbon, these are the p_z orbitals that are perpendicular to the sp^2 orbitals. The π bond is relatively weak, therefore the electrons in it are rather delocalized.

As introduced when discussing the carbon-carbon double bond for ethylene, the two bonds are extremely different in their behavior. When considering more carbon atoms to be bound together, the carbon bonds are alternating between double and single bonds. This repetitive change of the bond between the individual carbon atoms is the basic principle of organic semiconductors. The two main types of organic molecules that exhibit a semiconducting behavior are small molecules and conjugated polymers.

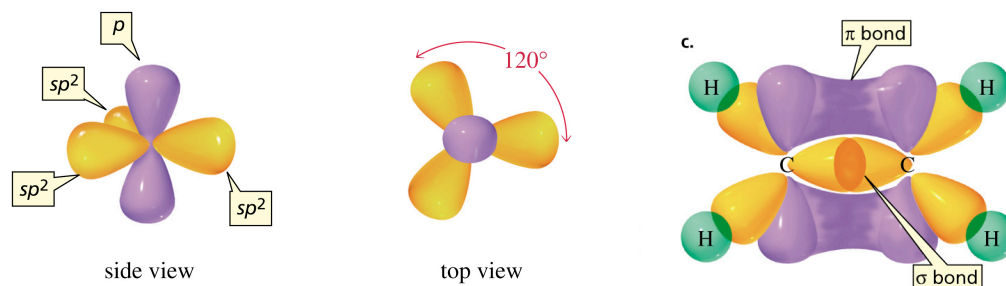


Figure 2.3: Visualization of the sp^2 hybridization of carbon and the carbon double bond. Orbital picture of one carbon atom in side (left) and top view (middle). Orbital picture of a carbon double bond for the example of ethylene (right). The difference between π and σ bonds can be clearly recognized. Whereas a π bond is formed by the overlap of the p-orbitals of the individual carbons, the overlap of the sp^2 orbitals of the carbons and the carbon-hydrogen bond are all σ bonds. Taken from [2].

2.1.1 Small molecules

The semiconducting behavior of small molecules can be explained best taking benzene, a simple example of an aromatic hydrocarbon, as a representative. There again localized strong σ bonds between the sp^2 hybrid orbitals and weak delocalized π bonds are formed. This is depicted in figure 2.4. In fact, the π bonds form a molecular orbital over the whole system.

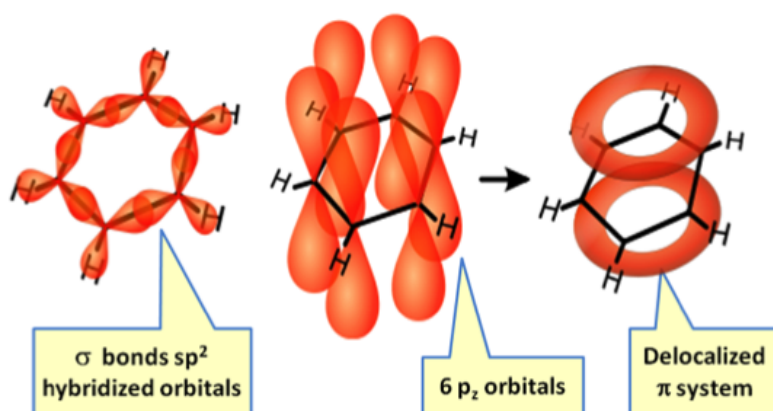


Figure 2.4: Visualization of orbitals of benzene. The strong σ bonds for the sp^2 orbitals (left) and the delocalized π system formed by the 6 p_z are illustrated (right). Taken from [1].

As a consequence of the molecular orbital theory, the molecular orbitals are a linear combination of the involved atomic orbitals. Therefore the π bond (of course also the σ bond) is splitted into a binding (π) and an antibinding (π^*) orbital, which are only separated by a small energy gap. The π^* orbital is higher in energy and is better known as the LUMO (Lowest unoccupied molecular orbital) level in organic electronics. The π orbital is the filled orbital at lower energy or HOMO

(Highest occupied molecular orbital) level. The low energy gap between HOMO and LUMO level is the origin of the semiconducting behavior of organic molecules. The size of the band gap correlates with the emission color of the OLED. As the band gap can be influenced by the structure of the molecule, the color can be tuned as well.

2.1.2 Conjugated polymers

An other way for semiconducting behavior arises from long conjugated polymer chains, consisting of a n-time repeated C-H unit. This repeated unit is called monomer. If the molecule consists of more than one monomer the used term is copolymer. Changing the monomer unit, the length of the polymer chain, or attaching different side chains or endcapping units influences the optical behavior as well as the processability of the polymer (i.e. solubility, polarity). In conjugated polymers again π bonds are formed between the individual p_z orbitals. This is schematically depicted in figure 2.5 using poly(acetylene) as an example.

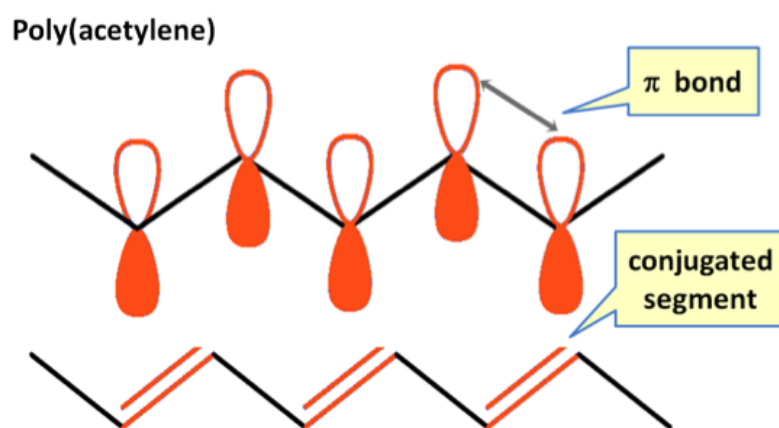


Figure 2.5: Poly(acetylene) as an example for a conjugated polymer. Taken from [1].

So in principle it works nearly the same as for small molecules. An important difference between the two classes of materials lies in the way how they are processed to form thin films. Whereas small molecules are usually deposited from the gas phase by sublimation or evaporation, conjugated polymers can only be processed from solution, e.g. by spin-coating or printing techniques [76].

2.1.3 Fundamental excitations

As organic semiconductors exhibit a strong electron lattice coupling, excited states in organic semiconductors are described by quasiparticles. The two important kinds of quasiparticles when

talking about OLEDs are polarons and excitons.

2.1.3.1 Polarons

Polarons are charged quasiparticles. They describe the situation in an organic semiconductor when an electron is removed from the HOMO or added into the LUMO including the structural relaxation of the polymer according to this event. Therefore, electronic states within the bandgap of the material are possible. Polarons are localized states, this is a result of the previously mentioned strong electron lattice coupling. It is a huge difference to inorganic semiconductors, where within the valence and conduction band the charges can move freely. All types of polarons important in semi conduction materials are depicted in figure 2.6. As can be seen, a missing electron in the HOMO is named positive polaron, an additional electron in LUMO is called negative Polaron. For completeness also bipolarons are depicted in figure 2.6, a bipolaron defines the situation where two electrons are missing respectively added.

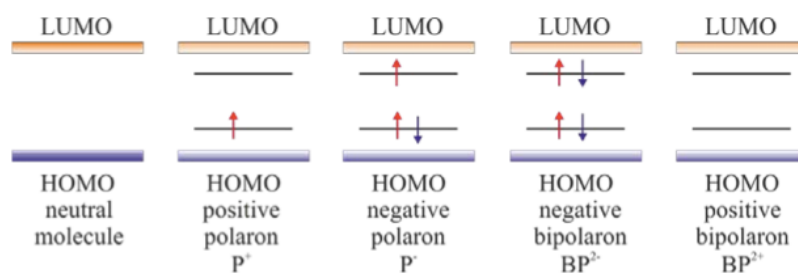


Figure 2.6: Schematic picture of the energy levels for the different types of polarons compared to a neutral molecule. Taken from [67].

2.1.3.2 Excitons

Excitons are neutral quasiparticles, consisting of an electrostatically bound pair of polarons with opposite charge. In general, excitons are elementary excitations. Excitons are electrically neutral and can therefore transport energy through the polymer, without any charge transport. There are two types of excitons that can be defined, depending on the distance between the polarons. If the distance is low ($< 5\text{\AA}$), they are called Frenkel excitons. For large distances ($40 - 100\text{\AA}$) they are named Mott-Wannier excitons. For organic semiconductors Frenkel excitons are important.

The polarons, that form an exciton, are characterized by Fermi-Dirac statistics and possess a spin of $\pm \frac{1}{2}$. Due to basic quantum mechanics, these quasiparticles must obey Pauli's principle.

This means that the total wavefunction needs to be asymmetric upon exchange of two identical particles. Therefore either the spatial or the spin part of the wavefunction needs to be antisymmetric. Altogether, there are four possible spin wavefunctions for the case of two bound fermions left:

$$\text{singlet state: } |\Phi_s\rangle = \frac{1}{\sqrt{2}}(|\uparrow\downarrow\rangle - |\downarrow\uparrow\rangle) \quad (2.1)$$

$$\text{triplet states: } |\Phi_t\rangle = |\uparrow\uparrow\rangle \quad |\Phi_t\rangle = \frac{1}{\sqrt{2}}(|\uparrow\downarrow\rangle + |\downarrow\uparrow\rangle) \quad |\Phi_t\rangle = |\downarrow\downarrow\rangle \quad (2.2)$$

If the spatial part is antisymmetric, there are three different possibilities for the spin part. This state is three times degenerated and is therefore called triplet state. The other way round, the spatial part is symmetric and the spin part must be antisymmetric. In this case there is just one possibility left, the state is called singlet state. A schematic picture of spin statistics for single and triple excitons is depicted in figure 2.7. For the single exciton, the spin direction of the excited electron stayed the same. In the case of a triplet exciton, the excited electron changed its spin direction between ground and excited state.

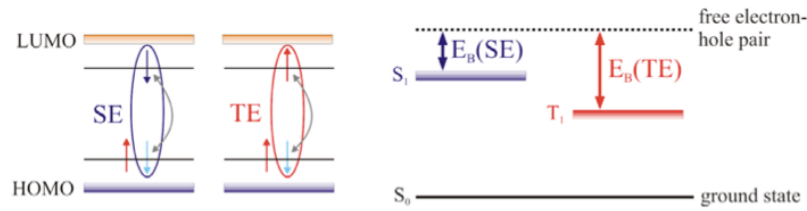


Figure 2.7: Schematic picture of the spin statistics of the single (SE) and triple excitons (TE) (left); schematic comparing the energetic level for the singlet and triplet state to a free electron-hole pair. Taken from [67].

2.1.4 Transition between electronic states in organic semiconductors

The Jablonski diagram, as depicted in figure 2.8, illustrates all possible processes that can happen in a molecule in an easy and compact way. S_0 and S_1 represent the ground state and the first excited singlet state. T_1 represents the first excited triplet state. Other excited states with higher energies are also possible, but are excluded in figure 2.8 for better readability. Moreover the individual electronic states are illustrated including their individual vibrational levels. The vibrational relaxation in to the lowest vibrational state takes place within a fast period of time (10^{-15} s) and is illustrated using diagonal arrows in figure 2.8. In general all diagonal arrows in figure 2.8 represent non radiative transitions. The absorption, illustrated with blue arrows, or in the case of OLED rather named excitation, takes place within 10^{-15} seconds. These excitations for OLEDs are excitons, they relaxate into the ground state according to the Jablonski diagram.

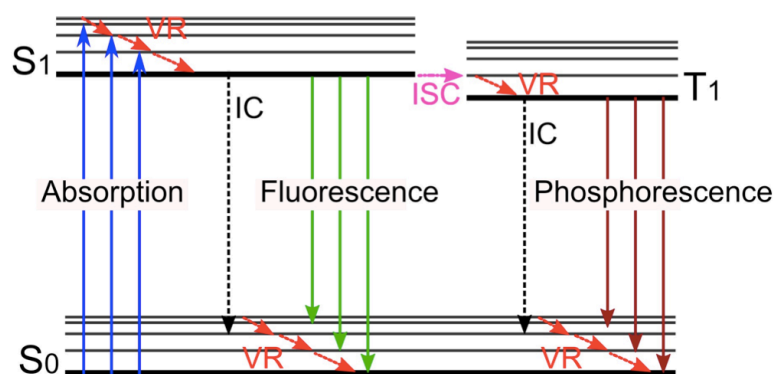


Figure 2.8: Jablonski diagram illustrating all possible radiative and non-radiative processes in a molecule. ISC: intersystem crossing; IC: internal conversion; VR: vibrational relaxation. Taken from [44].

2.1.4.1 Absorption and the Franck-Condon-Principle

Another important result of the excitation process taking place in a molecule is the structural response of the lattice. This response is a rather slow one, taking place within 10^{-10} to 10^{-13} seconds. The fact that the electronic transitions is fast compared to the lattice response is causal for the Frank-Condon-principle [18], [23]. According to the Frank-Condon-principle, the excited electron populates the vibrational level, of a specific excited state, with the highest integral overlap of the vibrational wave functions. The vibrational relaxation takes place immediately afterwards, from there the radiative transition takes place (Kasha's rule [40]). Depending on the spin statistics of the exciton, this radiative relaxation is called phosphorescence or fluorescence.

2.1.4.2 Fluorescence

An optical transition where an excited state relaxes and the spin remains is called fluorescence. This process is quantum mechanically allowed. The lifetime of a singlet exciton is typically in the range of 1 to 10 ns. In the case of charge injection, it is possible to create singlet as well as triplet excitons. In a fluorescent material, the triplet excitons can not be used for an optical transition. As the triplet state is degenerated three times, in spin statistics it is assumed, that only 25 % of the excitons are singlet excitons.

2.1.4.3 Phosphorescence

If the spin direction flips from excited state to the ground state upon relaxation, this is generally called phosphorescence. Quantum mechanically this process is forbidden as the spin flip needs to be caused by an additional interaction. Therefore a non-radiative interaction takes place. If heavy atoms are present in the molecule, this behavior changes and a delayed optical transition takes place. The absolute quantum mechanical prohibition is abolished by the increasing spin-orbit coupling of heavy atom. The lifetime of a triplet exciton is therefore relatively large and can even be seconds. The probability of an intersystem crossing from the singlet to the triplet state also increases when heavy atoms are present. Intersystem crossings are represented by pink arrows in figure 2.8.

2.1.4.4 Photoluminescence and Electroluminescence

The photoemission in the case of organic semiconductors is differentiated between photoluminescence and electroluminescence. The two processes are different in the way the excitons are generated. The process is called photoluminescence, when the excitons are created by an excited electron upon photoabsorption. In the case of electroluminescence, the excitons are generated by a recombination of two injected oppositely charged polarons. In the case of OLEDs, therefore one is always talking about electroluminescence, as the charged polarons are injected from the electrodes into the organic semiconductor.

Electroluminescence quantum yield

The quantum efficiency of an organic light emitting diode can therefore be expressed by the electroluminescence quantum yield (η_{EL}):

$$\eta_{EL} = \eta_{PL} \cdot r_{st} \cdot \gamma \cdot k \quad (2.3)$$

where γ denotes the number of excitons formed per injected charge carriers. A balanced charge carrier injection on both electrode sides improves γ . Additional injection and/or blocking layers on cathode and/or anode side can be applied in order to get an appropriate charge carrier balance.

r_{st} is the ratio of singlets formed per exciton. In the case of fluorescent emitters, this is equivalent to the singlet-triplet ratio. According to basic spin statistics, 1/4 of the excitons are singlets. This is up to now still a widely discussed topic within the scientific community [24], [78].

η_{PL} is the photoluminescence quantum yield and defines the efficiency of the light emitting material itself. As described with the Jablonski diagram, an excited state of a molecule can relaxate to the ground state by various radiate as well as non-radiative ways. According to this, η_{PL} is the ratio of photons emitted over the number of photons absorbed. All non-radiative transitions limits the photoluminescence quantum yield.

k is the proportionality factor of several loss mechanisms, like for example quenching effects or losses during the light outcoupling from the device.

2.2 Organic light emitting diodes

Ever since Tang and Van Slyke [63] reported on a successfully fabricated low voltage OLED, utilizing evaporated small molecules as emissive layer, the basic device structure stayed the same. From a historical point of view another important development that needs to be mentioned, is the first report on the electroluminescence of polymers [12], as described in detail in section 2.1. Whereas over the years the device assembly got more complex by the application of more and more active layers (multilayer approach) for obtaining a better charge injection amongst others, the basic functionality stayed the same. Therefore, the following explanations of the architecture and working principle are explained for the single layer architecture. The term single layer device refers to the number of light emitting layers only. Besides this, also the electrodes can be fabricated

from multiple layers for obtaining a better energy level alignment at the interfaces to the active material. This is going to be discussed in more detail in the experimental section of this thesis.

2.2.1 Architecture

The basic architecture of a single layer OLED is depicted in figure 2.9. In general, an organic light emitting device consists of at least, an emissive layer sandwiched between two electrodes, built on an a carrier substrate (e.g. glass). In order to outcouple the generated photons, one of the two electrodes needs to be transparent. In most cases the anode of the device is transparent and ITO (indium tin oxide) is used. ITO is a so-called TCO (transparent conductive oxide). As cathode material metals are used, this also has the advantage, that the cathode is reflective, so the outcoupling losses are minimized. In standard procedures the cathode is evaporated via a shadow mask.

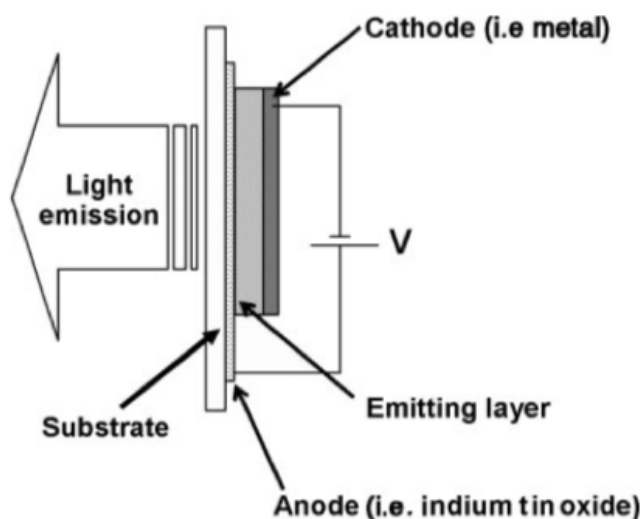


Figure 2.9: Basic OLED device structure. Taken from [30].

2.2.2 Working principle

The working principle of an OLED can be explained best when taking a look at the energy levels of the individual materials. This can be seen in figure 2.10. On the left hand side the work function of the two electrodes as well as the energy level of LUMO and HOMO of the organic semiconductor are depicted. Here no voltage is applied. On the right side, the same single layer

device design is depicted, this time an external bias is applied in forward direction. In order to inject the charge carriers into the organic semiconductor, electrodes are placed on both sides of the active material. Without an applied voltage, there are energy barrier for the charge carrier (E_h and E_e). When an external voltage is applied in forward direction, the electrons from the top cathode get injected into the LUMO of the organic semiconductor and the holes get injected into the HOMO of the semiconductor. (More accurately the electrons get extracted from the HOMO of the organic semiconductor by the anode.). This is possible because the HOMO and LUMO levels get tilted as a consequence of the applied voltage. The charge carrier can overcome the resulting triangle shaped injection barriers. The formed polarons move in to the organic semiconductor as a result of the applied voltage. If two polarons with opposite charge get attracted by coulomb forces they can form an exciton and decay after a certain time. The decay follows the already presented possibilities (Jablonski diagram).

Hence, the energy barrier between the anode and the HOMO level and between the cathode and the LUMO level, respectively should be as small as possible. Moreover, for a good device efficiency the charge carrier injection should be balanced, or in terms of energy levels, the energy barrier on both sides of the organic semiconductor should be nearly the same. Another issue are the charge carrier mobilities, that of course should not vary to much. Ideally, the recombination zone should be centered in the organic semiconductor. This can be achieved by blocking layers (hole blocking on the cathode side and electron blocking at the anode side).

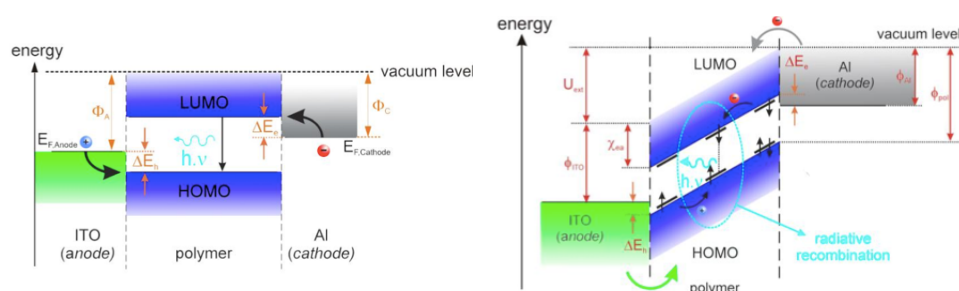


Figure 2.10: Energy levels of electrodes and organic semiconductor: Without applied voltage (left), biased in forward direction (right), with ΔE_h and ΔE_e the hole and electron injection barriers, ϕ_A and ϕ_C the work function of the electrodes and U_{Ext} the external bias. Taken from [66] and modified.

2.2.3 Charge injection and charge transport

As organic semiconductors are normally intrinsic, the influence of the injection barriers is essential for the number of charge carriers injected into the active material. As pointed out, this can be investigated with UPS measurements. Besides this, also the charge transport within the individual

layers is important. An unbalanced charge carrier injection results in a high leakage current (charge carrier pass through the active material without recombining) and should therefore be avoided. When applying a bias in forward direction, a triangle shaped potential barrier forms on both metal/organic contacts, resulting in an increased probability for charge injection. Figure 2.11 shows the energy potential that is left at the metal organic interface, when an external force is applied in forward direction. The effective potential can therefore be rewritten as:

$$V(x) = \phi - eFx - \frac{e^2}{16\pi\epsilon_0 x} \quad (2.4)$$

where ϕ is the difference between the metal work function and the electron affinity of the polymer. The second term represents the electric field due to the applied voltage and the final term describes the image field. The image field arises as image charges build up in the metal electrode when carriers approach the metal-polymer interface.

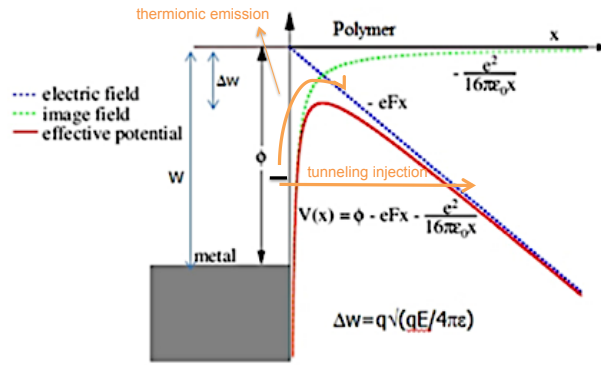


Figure 2.11: Potential diagram at a metal organic interface. The potential barrier that charge carriers need to overcome is reduced to an effective potential (red) by the applied bias (blue) and the image force (green). The two possible charge injection mechanisms are included (orange arrows). Taken from [45] and modified.

The ideal electron injection can be realized when the work function of the cathode is smaller than the LUMO level of the organic semiconductor. This is called ohmic contact. For the hole injection, the HOMO level needs to be smaller than the work function of the anode to get a ohmic contact.

In general, there are two known charge carrier injection mechanisms known: Thermal emission and field emission (quantum mechanically described as tunneling). The current density for thermal emission is described by the Richardson-Dushman equation and the probability of injection increases with increasing temperature of the metal. Within OLEDs, the temperatures are rather low, therefore this mechanism is only important at low energy barriers. The current density for field emission is described by the Fowler-Nordheim equation and the injection probability increases

with increasing electric field. In the case of tunneling, the charge carrier is injected directly into the organic semiconductor and tunnels through the remaining triangle shaped energy barrier. The thinner the energy barrier, the higher probability of tunneling. As the energy barrier is reduced by an increasing electric field (see figure 2.11), this is coherent with the requirement described by Fowler-Nordheim. The charge transport in an organic semiconductor with localized states is described by a hopping between the localized states. The conduction is as afore mentioned field-dependent [45].

2.2.4 Energy level alignment at the interface

Investigating the electrode/organic interface in more detail, it is not enough to simply consider the individual electronic structures. When two materials get in contact, the electronic structure is changed as well. This is depicted in figure 2.12. For an infinite distance between the electrode and the organic semiconductor, one can assume a vacuum level alignment. Here no interaction between the two materials is included. This so called Schottky-Mott-rule gives of a good estimation of the energy barrier behavior of the materials upon contact. This vacuum level alignment according to the Schottky-Mott-rule is once more in an energy level configuration depicted on the left side of figure 2.13. In general, the modification of the surface (more specifically the rearrangement of the electron density distribution [43]) of the materials when they get in contact needs to be considered. This results in a modification of the electronic structure of both materials, also known as "vacuum level shift" or "interface dipole" [43], [38]. The influence of this interface dipoles on the electronic structure can be huge (up to 1 eV). This general case where interface dipoles are also considered is depicted in figure 2.13. UPS measurements are a powerful tool to investigate the influence of these interface dipoles on the electronic structure of a specific device configuration.

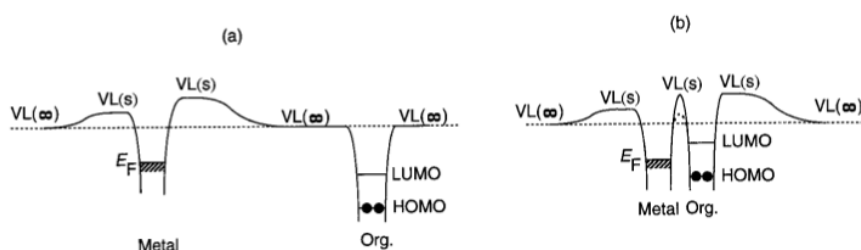


Figure 2.12: Electronic structure of a metal and an organic semiconductor at infinite distance (left image) and in contact (right) according the Schottky-Mott-rule. Taken from [38].

Several processes can be responsible for this vacuum level shift. They are summarized in figure 2.14. Besides the intrinsic dipole of the organic semiconductor (f), a chemical reaction between

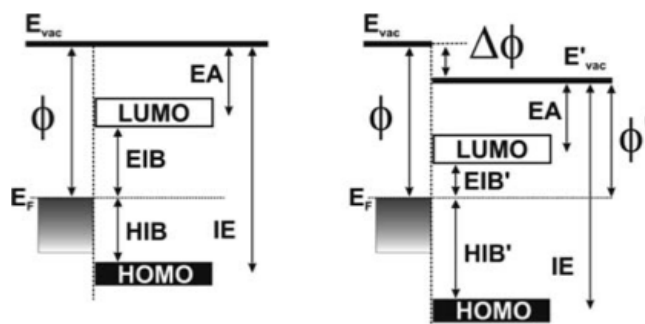


Figure 2.13: Energy levels for an electrode/organic semiconductor interface. In the Schottky-Mott limit (left) and in a more general case (right), where a work function change ($\Delta\phi$) can be observed due to the interface between the electrode and the organic semiconductor. Taken from [43].

the electrode and the semiconductor can also be the reason for a interface dipole formation (d). Moreover a simple charge carrier transfer between the two layers is one possibility (a). A surface rearrangement upon the deposition of one material on top of the other, can also lead to a dipole formation (c). Besides these also a polarization of the electrode cloud can be observed as a result of the attraction by the image charge in the metal (b). Arising interface states when mixing the energy states of both layers can be a further reason for the formation of interface dipoles (e).

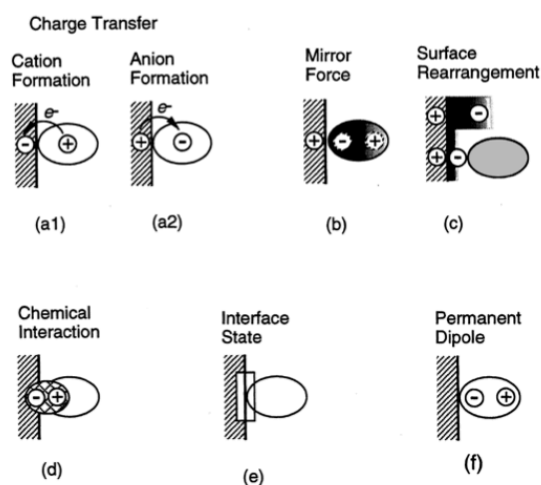


Figure 2.14: Possible interface dipole formations: a1), a2) charge transfer across the interface, b) Polarization of the electrode cloud (due to the attraction by the image charge in the metal), c) rearrangement of the electron cloud as a consequence of the "pushback" effect, d) chemical interaction, e) interface state that serves as buffer of charge carriers, f) permanent dipole of the organic material. Taken from [38].

3 EXPERIMENT METHODOLOGY

In the following section, several layer deposition techniques used within this thesis are described. Besides this, the layer assembly for reference devices is explained. Also the characterization of the fabricated devices is described. Finally, the used set up for investigating the layer interfaces is presented. The used equipment for the device fabrication and characterization is, with the exception of the inkjet printer, placed in an ISO-class 6 clean room or grey room at NTC Weiz. As organic materials are sensitive to oxygen, the device fabrication took place in NTC's glove box cluster once the first organic material was applied. The only exception was made when the top cathode was inkjet printed on top of the device stack. If not mentioned differently within the document, all presented devices have been fabricated according to the now described routine.

3.1 Device fabrication

3.1.1 Substrate preparation

In general, all OLED devices have been fabricated on three different substrates. As a reference system, glass substrates have been used. As flexible substrates, foils purchased at *DuPont*[®] [6] have been used. The chosen polymer films are a Polyethylene terephthalate (PET) film with the product designation *MELINEX*[®] *ST504* and a Polyethylene naphthalate (PEN) film with the product designation *TEONEX*[®] *Q65FA*. From now on, these films are referred to as PET and PEN. A comparison of these two foils, as well as several important values are summarized in table 3.1.

All devices were fabricated on square substrates with an edge length of one inch (25,4 mm). The glass substrates have been purchased at this size, while the plastic substrates have been cut with scissors. For the reference devices, ITO (indium tin oxide) has been used as the transparent conductive anode material. The ITO coated glass substrates (Delta Technologies) have an average sheet resistance of approximately $15 \Omega/\square$ and an average height of 100 nm. ITO coated polymer

foils (coating by Solutia, Polymer films as described previously by Du Pont) show an average sheet resistance in the same range as the used ITO coated glass substrates. Besides this, the rougher surface of the polymer films as well as a high amount of scratches reduces the overall anode performance.

Table 3.1: Important parameters of the two used polymer films. (values taken from [6])

Parameter	Unit	Q65FA	ST504
Thickness	μ	125	125, 175
Transparency	%	87	85
Upper temperature for processing	$^{\circ}C$	220	150
Thermal shrinkage in machine direction 30 min at 150 $^{\circ}C$	%	0,1	0,15

In those cases where ITO coated substrates were used as carrier substrate plus anode layer, the ITO layer was structured by a wet chemical etching process. Therefore the ITO layer was covered with Scotch tape in the center area of the substrate, where the ITO should not be removed. Then the substrate was immersed into hydrochloric acid (37 % HCL) for approximately 25 seconds. Afterwards the substrate was carefully rinsed with deionized water and the tape was removed from the substrate.

Before the device fabrication the substrates were cleaned. This standard cleaning process was the same for plane substrates (foil, glass) and for ITO coated substrates. The cleaning process consists of the following steps (The italicized steps just applied for glass substrates):

- *Substrate was rinsed with toluene*
- Substrate was rinsed with Isopropanol and blown off with N_2
- *Ultrasonic treatment of the substrate in toluene (duration: 15 min) and blown off with N_2 afterwards*
- Ultrasonic treatment of the substrate in Isopropanol (duration: 15 min) and blown off with N_2 afterwards
- Reactive oxygen etching process of the substrate surface in a plasma chamber (duration: 5 min for glass substrates and 0,1 min for flexible substrates)

3.1.2 Layer deposition techniques and used facilities

Subsequent all used layer deposition techniques are described in detail, the advantages and disadvantages of the individual techniques are pointed out and the used facilities are specified.

3.1.2.1 Spin coating

Solution processed polymer films are mainly fabricated by spin coating. The main advantage of spin coating is that a thin uniform coating on a large area can be achieved within a short time period. Besides this, spin coating is a very simple method, which in general consists of three fabrication steps. First, the solution is spread uniformly on a substrate, that is mounted on a chuck. Then a layer formation step occurs, where the solution is spread evenly on the substrate. The third and last step is the evaporation of the remaining solvent. The spin coating of the active materials within this thesis has been performed in a glove box. The individual spin conditions and heating parameters are described in section 3.1.3. Spin coating benefits of several advantages, only patterning the substrate is difficult, this makes a device fabrication only by spin coating processes impossible. Hence spin coating is mainly used for the emissive layer application, whereas the electrodes are fabricated differently. Moreover, the different layers can dissolve one another, if applied from the same solvent. So only a few spin coated layers can be applied one on top of the other. Used strategies to overcome this dissolving problem are described in section 3.1.3.

3.1.2.2 Photolithography

Photolithography is an optical patterning technique with extremely high accuracy (nm-scale). Photolithography consists of several fabrication steps that stay the same no matter what photo resist is used. First the substrate is cleaned and, if necessary, modified in order to guarantee a proper film formation of the subsequent photo resist layer (the substrate surface should be as hydrophilic as possible). Then the photo resist is spin cast on the substrate, afterwards a so called softbake is performed to remove residual solvents. The actual UV exposure of the photo resist is performed using an EVG 620 mask aligner. This mask aligner is suitable for substrate with a diameter up to 4 inches. For the exposure, a proximity mode has been chosen with a remaining distance between substrate and mask of 2 μm . The used mask is a chrome patterned quartz glass. For enhancing the UV induced polymer cross linking process, a so called hard bake is performed after the UV exposure. Finally, the substrate is immersed into a developer and the soluble photo

resist is removed. Then the substrate is thoroughly rinsed with deionized water and dried with a spin coater (5000 rpm (rotations per minute), 100 s).

In general, photo resists can be distinguished in positive and negative resists. For a positive photo resist, those parts exposed to the UV light become soluble in the developer and vice versa for negative resists. Depending on the used photo resist and the purpose of the fabrication, the individual parameters can change dramatically. All chemicals (photo resists, developer, remover) used during the photolithography have been purchased at MicroChemicals. If the photolithography is used as a combined structuring method with metal evaporation, a so called lift off is performed. During the lift off the substrate is immersed into the NMP (1-methyl-2-pyrrolidone) remover at 65 °C in an ultrasonic bath. The substrate is immersed for 5 plus 2 min in order to fully remove the photo resist. Then again, the substrate is rinsed with deionized water and dried with a spin coater (5000 rpm, 100 s).

For the purpose of patterning evaporated structures, a negative photo resist (AZ[®] nlof2035) was taken. The chosen standard parameters are summarized in table 3.2.

Table 3.2: Chosen standard parameters for photolithography with negative photo resist AZ[®] nlof2035.

Parameter	value
Spin parameters	5000 rpm 30 s
soft bake	110 °C 180 s
exposure mode	proximity
exposure dose	100 mJ/cm ²
hard bake	110 °C 80 s (glass) 110 °C 60 s (foil)
used developer	AZ826 MF
developing time	60 s (glass) 40 s (foil)

In a new approach, the photo resist was taken as transparent embedding material. The details on this topic are explained in section 4.4. A thick positive chemically amplified photo resist AZ[®] 40XT was used and the selected fabrication parameters are summarized in table 3.3.

The whole photolithography process was performed in NTC's cleanroom. The substrate cleaning, spin coating and heating steps were performed in a wet bench. Thus the contamination possibility of the substrate during the fabrication process was reduced to a minimum.

Table 3.3: Chosen standard parameters for the photolithography with the positive photo resist AZ[®] 40XT.

Parameter	value
Spin parameters	6000 rpm 40 s
soft bake	110 °C 60 s
exposure mode	proximity
exposure dose	100 mJ/cm ²
hard bake	110 °C 60 s (glass) 110 °C 40 s (foil)
used developer	AZ726 MF
developing time	20 s (glass) 15 s (foil)

3.1.2.3 Vacuum deposition

Vacuum deposition is a standard layer deposition technique. It can be used for structured metal evaporation through a shadow mask and to evaporate organic layers from small molecules. Vacuum deposition is adaptable for nearly all small molecules and metals and the fabricated layers are extremely homogeneous and reproducible. Up to now, vacuum deposition is the most widely used technique in organic electronics. For this deposition technique a source material is heated up within a vacuum chamber. The actual substrate is placed a certain distance (cm-scale) away. In a normal geometry the substrate is placed above the source metal, this is the favorable geometry as it prevents a contamination of the substrate previous to the deposition. As no solvent is used for vacuum deposition, multiple layers can be evaporated on top of each other, without any interaction between the individual layers.

Vacuum deposition also suffers from several drawbacks, especially when thinking about large area manufacturing on flexible substrate. Not only does vacuum deposition require high vacuum conditions, only this way a large mean free path can be achieved, also the occurring mask sagging for larger device areas limits the maximum size that can be produced. The high vacuum conditions are a high cost factor in organic device manufacturing. Besides this, also a high amount of material is wasted when using shadow mask vapor deposition, as it ends up coating the mask.

All vapor deposition was done using a custom made evaporation chamber. The vacuum before the evaporation was around 10^{-6} mbar and the deposition rate was between 1 nm/s and 10 nm/s, depending on the evaporated material (lower evaporation rate for organic layers, higher evaporation rate for metals).

3.1.2.4 Inkjet printing

Inkjet printing is, along all these methods the most promising one. It combines the advantages of all the previous methods. The working principle is actually the same as known from an ordinary office printer.

Within the middle 1980's, drop on demand (DOD) printing was established on a commercial basis [50]. Also for today's lab scale inkjet printers DOD is the mostly used print head technology. With DOD, one differentiates between piezoelectric DOD and thermal DOD. Piezoelectric DOD print heads, as used within this thesis, utilize the piezoelectric effect [50]. The used printhead was a Spectra SE-128 with 128 nozzles with a drop size of 30 pL each. The drop formation is controlled for example by piezoelectric shear elements outside the ink filled membrane. An applied voltage results in a contraction of the membrane and a pressure wave is generated inside, which results in a droplet formation inside the nozzle. Figure 3.1 shows a schematic illustration of the droplet formation in a piezoelectric printhead.

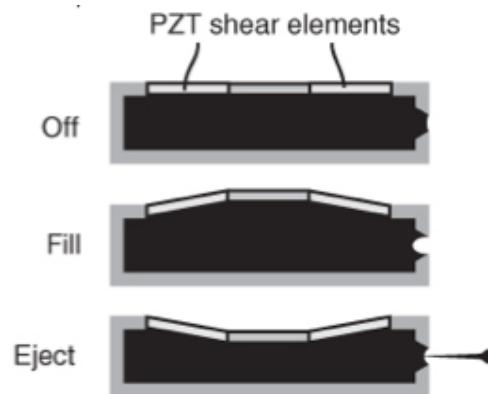


Figure 3.1: Schematic illustration of the droplet formation in a piezoelectric printhead. (taken from [50])

The desired print layout is designed using a graphic editor, in this case CoralDraw, and by using an USB-port, the tagged image file is transferred to the printer. So the resolution pattern is a digital print. For inkjet printing, the material waste is low, no vacuum chamber is necessary and a structured pattern is achieved easily. The drawback of this method is that the materials are dissolved in solvents and afterwards, during a heating step, the remaining solvent is evaporated. Therefore the material properties are lower than in case of pure metal evaporation. Besides this, only a limited number of materials is available on ink basis and moreover, as it is the case for spin coating, just a limited amount of layers can be applied one on top of each other. Due to the solvent input, the layers dissolve each other and reduce the individual material performance. Another limiting point for a large breakthrough of this method is the fact that due to the droplet formation in

the nozzle, the maximum feature size is defined, so down scaling is limited by the used print head.

Inkjet printing was performed using a PIXDRO LP50 printer with a piezoelectric print head. The versatile requirements for the ink are a tricky point as well, values like viscosity and material content need to be optimized. Within this thesis all electrode fabrication was performed using a commercially available silver nanoparticle ink (Cabot CCI 300) [5] consisting of an alcohol solvent with a silver solid content of about 20 wt%.

3.1.3 Reference device assembly

All electrode modifications within this thesis have been compared and benchmarked to so called reference devices. The reference devices consist of the following layers:

- Structured ITO was used as transparent **anode**, afterwards a layer of PEDOT:PSS [poly(3,4-ethylenedioxythiophene) poly(styrenesulfonate)] was spin-cast on top. The PEDOT:PSS was purchased from H.C. Starck (Clevios P VP AI 4083). For the spin coating a speed of 2500 rpm and a time of 40 seconds have been chosen. The wetting time was approximately 10 seconds. These parameters conclude in a layer thickness of approximately 50 nm. The spin-cast process took place in a laminar flow box under ambient conditions. The PEDOT:PSS layer was dried on a hot plate at 200 °C for 5 minutes (respectively 15 minutes at 120 °C in the case of flexible substrates) afterwards. PEDOT:PSS is used as smoothing and hole injection layer on top of ITO.
- The **active layer** consists of one to three layers, depending if additional hole transport layers (HTL) on the anode side and/or electron transport layers (ETL) on the cathode side are applied. The advantage of the so called multilayer approach is described in more detail in the fundamentals.
- The **cathode** is an evaporated bilayer consisting of a 10 nm calcium layer and a consecutive layer of 100 nm aluminium. Both evaporated via a shadow mask.

The devices fabricated within this thesis can be divided into two main groups according to the used active materials:

- **Evaporated active material:** Evaporated devices have the advantage that the individual layers are very homogeneous, which is favourable for anodes exhibiting a rough surface. A 40 nm thick TPD [N,N'- Bis(3-methylphenyl)-N,N'-diphenylbenzidine] layer was used as HTL and a 100 nm Al/q_3 [Aluminium-tris(8-hydroxyquinolin)] layer was the emissive layer,

resulting in a bright green emission. Both materials were purchased from Sigma Aldrich. Figure 3.2 shows the chemical structure of the two used materials. The absorption and photoluminescence spectrum of Alq₃ and TPD are depicted in the figures 3.3 and 3.4.

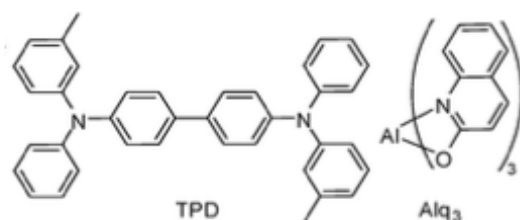


Figure 3.2: Chemical structure of TPD (left) and Alq₃ (right).

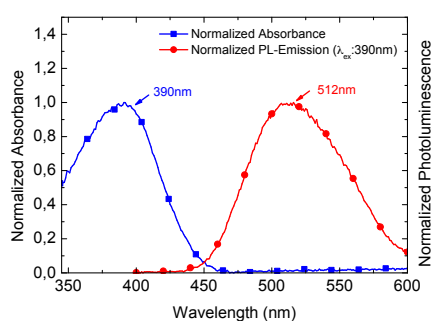


Figure 3.3: Normalized absorption and photoluminescence spectrum of 0,1 g/l Alq₃ in tetrahydrofuran (THF).

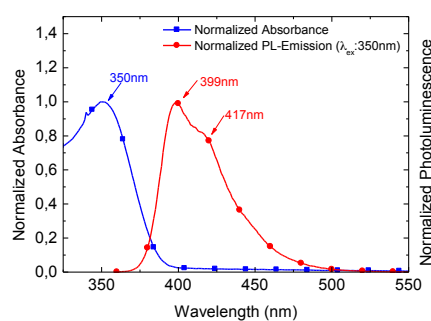


Figure 3.4: Normalized absorption and photoluminescence spectrum of 0,1 g/l TPD in tetrahydrofuran (THF).

- Spin cast active layer:** If an HTL was applied, TFB [Poly[(9,9-dioctylfluorenyl-2,7-diyl)-co-(4,4'-(N-(p-butylphenyl))diphenylamine)]] was used. The standard spin cast emissive layer (EML) used is ADS 232 [Poly[(9,9-dioctylfluorenyl-2,7-diyl)-co-(N,N'-diphenyl)-N,N'-di(pbutylphenyl)-1,4-diamino-benzene)]]]. Both materials were purchased from American Dye Sources INC and have been spin cast on top of each other. TFB was spin cast from a toluene solution with a concentration of 20 g/l. ADS 232 was spin cast from a toluene solution with a concentration of 6 g/l. For solutions spin cast from toluene, a spinning rate of 1000 rpm for 12 s to form the film and a subsequent drying step with 3000 rpm for 40 s have been chosen. The average layer thickness achieved with these spinning conditions for ADS 232 was measured with a Profilometer (VEECO Dektak 150) to be in the range of 50-60 nm. After the spin cast process, the substrate was heated to 80 °C for 30 minutes to dry the coated layer and remove the remaining solvent. During this process, the heating chamber was evacuated ($p < 5 \cdot 10^{-3}$ mbar) and the substrate was left in the evacuated chamber afterwards, until the chamber temperature cooled down to about 50 °C. TFB was also spin

cast from toluene, so the same spin parameters have been chosen. As the TFB is applied underneath the ADS232 layer and both materials are applied from the same solvent, the layers normally would dissolve one another. In order to prevent this, a so-called hard baking step, first described by Kim et. al [41], was used. Therefore the TFB layer was hard baked under inert atmosphere at 200 °C for 60 minutes and cooled down to about 50 °C afterwards. Then the substrate was spin rinsed with toluene (3000 rpm for 40 s). The remaining layer was measured to be about 5 nm thick (measured with an atomic force microscope (AFM)) and is insoluble even if toluene is applied on top again. Figure 3.5 shows the chemical structure of the two used materials. The absorption and photoluminescence spectrum of ADS232 and TPD are depicted in the figures 3.6 and 3.7.

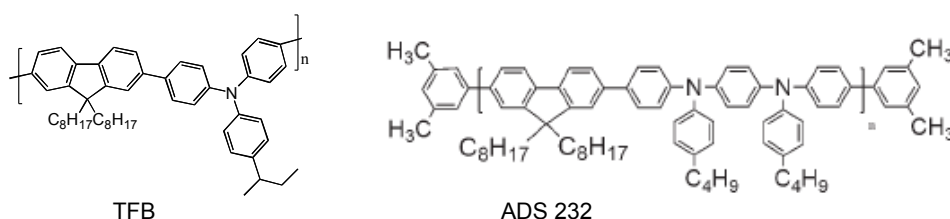


Figure 3.5: Chemical structure of TFB (left) and ADS232 (right).

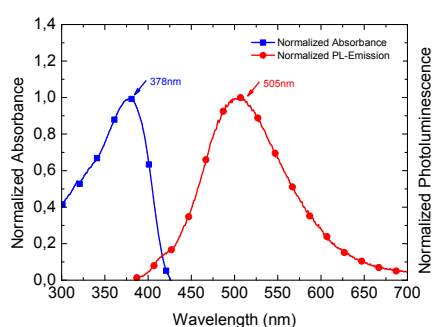


Figure 3.6: Normalized absorption and photoluminescence spectrum of 0,1 g/l ADS232 in tetrahydrofuran (THF). Taken from [11] and modified.

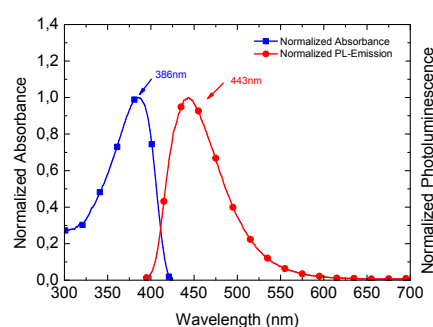


Figure 3.7: Normalized absorption and photoluminescence spectrum of 0,1 g/l TFB in tetrahydrofuran (THF). Taken from [11] and modified.

3.2 Device characterization

The whole device fabrication was performed under argon atmosphere, so that the degradation of the organic material due to environmental influences can be excluded, and a realistic comparison of individual devices was possible. Therefore all device have been mounted into a custom made measurement cell before they were transferred from the glove box cluster to the measurement set up, which is placed in the grey room. The used measurement cell can be seen in the insert of figure 3.8.

3.2.1 Current density-voltage-luminescence characterization

The current-voltage characteristics was measured via a computer controlled KEITHLEY 2612 SMU. The measurement routine was defined by a custom made *Labview*® program. Simultaneously the device luminance under operation was collected. Therefore a Keithley 6485 Picoammeter using a silicon photo diode, was mounted on top of the measurement cell, illustrated in figure 3.8. The measured photocurrent was then attached to the right luminance value. This calibration was done with a MINOLTA LS-100 luminance meter. As the size of the individual device is known to be 10 mm^2 , the current density can simply be calculated by dividing the measured current trough the active area.

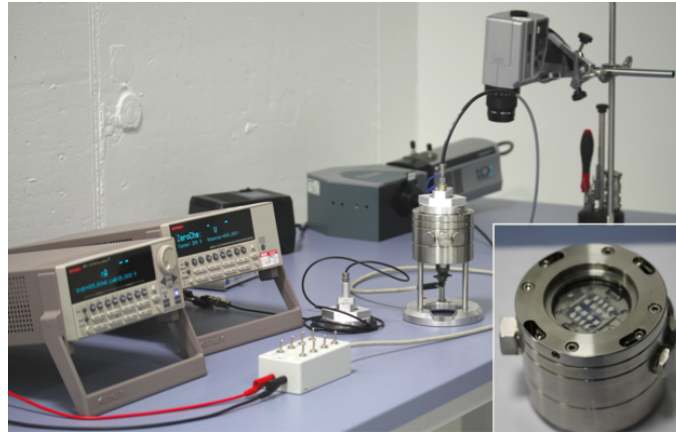


Figure 3.8: Computer-controlled OLED measuring equipment including CCD spectrograph for J-V-L measurements and custom-made measuring cell (inset)

Illustrated in the insert of figure 3.8 one single specimen exists of 8 individual devices. Changing between those devices was done by a switch matrix (center of figure 3.8). The photo diode was placed on top of each device by hand. According to this, several systemic errors are evident and

need to be mentioned for the sake of completeness. First, the position of the fiber optics that guides photons to the photo diode, varies in every single experiment. As the incidence angle of the fiber optic is limited, this is a serious issue. As no additional Ulbrich sphere is used, parts of the generated light are not detected. Besides this, the manual photocurrent to luminance calibration is an error source. The sensitivity of the detector has, especially in the low voltage range, a resolution limit for the detected luminance.

3.2.2 Electroluminescence spectra

The electroluminescence spectra of the light emitted by the investigated OLEDs were measured by an Andor Shamrock 163 spectrometer. The single spectral components are analyzed by a charge-coupled device (CCD). The noise of the sensor chip was reduced by cooling the chip down to -40°C . The sensitivity of the CCD chip is different over the wavelength range with a highest sensitivity for green emission. Therefore the collected spectra were corrected using a detector sensitivity curve.

The electroluminescence spectra were measured for different current densities as well as voltages. Starting from the smallest current density resp. voltage value, where a signal was measurable, the value was increased stepwise and the corresponding spectrum was recorded. In the end, the spectral behavior as a function of time at a constant current density was recorded.

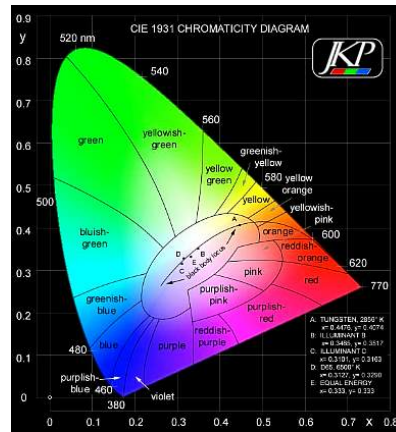


Figure 3.9: CIE 1931 color space chromaticity diagram. Taken from [3].

In order to mathematically define colors, the CIE 1931 color space chromaticity diagram was created in 1931 by the Commission Internationale de l'Eclairage and is going to be used to relate individual spectra of several devices one to another at a same applied current. The initial intention was to set up a relation between (human) color perception and physical color stimulus. In figure

3.9 the color space diagram is depicted and all relevant values are indicated. According to this, a color can be clearly related to a point on this diagram once the x and y value are known.

3.3 Interface Investigations

Interfaces of organic semiconductors can be investigated by various properties. For the evaluation of the surface, a contact angle meter (Krüss DSA 100) was used, optical microscopy was applied using an Olympus BX51, for stereomicroscopy an Olympus SZX-10 was used. The layer formation was also investigated using an atomic force microscope (AFM). In principle, an AFM consists of a sharp tip on a cantilever (works like a string, according to Hooks law), surface variations are measured in terms of differing deflection of the cantilever. With an AFM, resolutions down to sub-nanometer scale can be achieved. Moreover, also different materials can be distinguished, resulting in phase images where the phase margins are visible. The used AFM was a Veeco Dimension V AFM with a Nanoscope V controller, measurements were performed under ambient conditions. For analyzing the energy levels of the different materials on top of each other, photoelectron spectroscopy was used.

3.3.1 Photoelectron spectroscopy

Ultraviolet photoelectron spectroscopy (UPS) is a powerful tool for interface investigation. In order to get information about the material composition on individual materials x-ray photoelectron spectroscopy (XPS) can be used. The difference between those two methods has the origin in the energy of photoelectrons, the UV photoelectrons eject electrons from the valence band due to their energy (10-40 eV) and information about the HOMO level, the work function of the material and an estimation of the density of states (DOS) can be provided. X-ray photons, though eject core level electrons and therefore give information about the elemental composition. For interface investigation especially UPS is interesting. Photoelectron spectroscopy utilizes the external photoelectric effect, explained by A. Einstein in 1905, awarded with the Nobel Prize in Physics in 1921 [22]. The external photo effect states that an electron can be ejected from the surface of a solid due to the interaction of electromagnetic radiation with the material. More precisely, the incoming photon gets absorbed by an electron and if the energy of the incoming photon is higher than the ionization energy of the solid, the ejected electron is emitted. So in general the maximum kinetic energy of an emitted electron can be:

$$E_{kin}^{max} = h\nu - \phi \quad (3.1)$$

with h the Planck constant, ν the frequency of the incident photon and ϕ the work function of the sample.

Nevertheless the ejected electron needs to travel through the sample to the surface before it can leave the solid. Due to collisions between the electrons, the measured kinetic energy of the emitted photons is a continuous spectrum, this spectrum ends with the so called secondary electron cut off (SECO). The SECO is a sharp edge in the spectrum (E_{kin}^{min}), electrons with less kinetic energy can not escape the solid any more. Those electrons that emit without energy losses due to inelastic collisions are clearly visible features in the spectrum.

The emitted photons are measured with an analyzer and therefore the work function of the analyzer and the contact potential needs to be considered [13]. The kinetic energy is then defined as:

$$E_{kin} = h\nu - E_b - \phi_{sys} \quad (3.2)$$

with ϕ_{sys} defining the work function of the system and E_b the binding energy.

As the internal work function of the system is usually not known exactly, absolute values are not measurable. In order to overcome this problem, for metals a so called internal kinetic energy scale relative to the Fermi edge is introduced. By defining that the fastest electrons measured have the kinetic energy of $h\nu$, the hole spectrum measured is shifted. The so defined energy scale is equal to the energy of the electrons right before they leave the sample [59]. Using this scale, the SECO is the point where the electrons have just enough energy to leave the solid. So the binding energy can be determined by:

$$E_b^{max} = h\nu - E_{kin}^{int} \quad (3.3)$$

The binding energy for electrons at the Fermi edge is now set to zero. In the case of semiconductors, the work function can not be determined from the measured UPS spectrum of the semiconductor only. A value of the work function for a semiconductor can only be measured by defining the internal energy scale with the measurement of a known metal prior to the measurement of the semiconductor [59]. Photoelectron spectra are most likely depicted in terms of electron intensity as a function of binding energy.

A typical UPS spectrum of a gold surface is depicted in figure 3.10. There, the valence band features as well as a constant background and the SECO can be seen clearly.

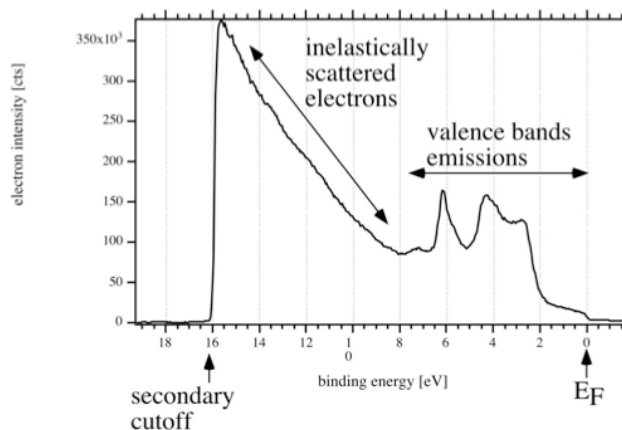


Figure 3.10: Typical UPS spectrum of gold. (taken from [59])

All UPS measurements were performed using the synchrotron light source at BESSY II (Berlin, Germany). The beamline PM4 (end station SurIcat) was used. All measurements were performed using glass substrates with ITO and an additional layer of PEDOT:PSS on top. The investigated materials were spin cast from 1g/l solutions. For UPS measurements, incident light with a photon energy of 35 eV was used, for XPS 650 eV were chosen. The SECO spectra were measured with a sample bias of -10 eV in order to clear the analyzer work function. The error of the reported binding energies is estimated to be less than 0,5 eV.

4 GRID SUPPORTED ANODE UTILIZED IN SINGLE AND MULTILAYER DEVICES

4.1 Introduction and Grid design

The mainly used transparent conductive oxide in organic electronics is and has been ITO (indium tin oxide). Even though ITO benefits from its good optical properties (>80 % transparency) as well as a considerably low sheet resistance down to $10 \Omega/\square$, many current research activities are focusing on replacing ITO as transparent electrode in organic electronics [83], [70], [75]. Multiple drawbacks are the reason for this large interest of the scientific community. The restricted world wide indium supply combined with a increasing indium demand, especially due to the heavy usage of ITO in organic industry, are the reason for an extreme price fluctuation of indium during the last years [71]. Besides this, ITO is generally deposited by vacuum-based, highly energy intensive deposition techniques like sputtering [10]. These two facts are the reason for the high costs arising from the use of ITO in organic electronics. Moreover, the brittleness of ITO is a serious issue concerning flexible devices. As for example reported in 2011 [9], the electrical resistance of an ITO coated PET substrate increases by nearly 100% if an 8 mm wide substrate is bent 10 times with a diameter of 5 mm (using a cycle frequency of 100 cycles/min).

So, alternatives for ITO should not only exceed the electronic properties of ITO exhibiting a comparable transparency, they also should be producible by low cost techniques and should show good stability upon bending. In a recent review on ITO alternatives by Krebs et al. [10], the diagram in figure 4.1 was depicted. It is a good summary of all possible alternatives researchers are currently focusing on. As within this thesis the focus is on low cost solution processed techniques, the right hand side of figure 4.1 is not considered any further.

PEDOT:PSS is the most widely used transparent polymer material in organic electronics. Several

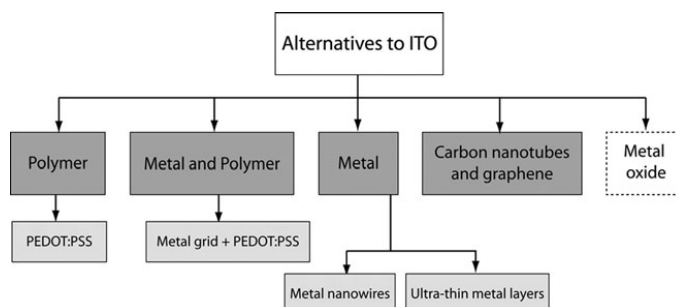


Figure 4.1: Summary of applied alternatives for ITO in organic electronics up to now [10]

attempts have been made in the past in order to increase the conductivity of this polymer, so that it can be used instead of ITO and not as an additional smoothing layer for ITO. The perfect trade off between increased conductivity and remaining high transparency was a key topic when increasing the PEDOT:PSS performance [15], [8]. As the conductivity of highly conductive PEDOT:PSS (HC-PEDOT:PSS) still remains significantly lower than for ITO, in 2004 Aernouts et al. came up with the idea of improving the performance of PEDOT:PSS by supporting it with a metal grid [7]. This double layer transparent electrode was heavily used for organic solar cells within the last years [28], [27]. Several grid designs have been tested within literature, with the objective of getting the best conductivity with still a high degree of transparency, especially focusing on the necessity of this grid support once the attempt is to scale up the device geometry [52], [25], [62]. The used metal grids therefore should exhibit small line width, high conductivity and a close-meshed design in order to obtain quiet constant conductivity over the hole pad.

Within this chapter, the metal grid supported PEDOT:PSS double layer anode structure is used for OLED manufacturing only. First, several results for OLEDs with an anode consisting of a photo-lithographically structured silver grid plus HC-PEDOT:PSS and an evaporated active layer are presented. Then the same anode structure was used with a spin coated active layer, there the problem with spincoating on top of non uniform surfaces was identified as limiting factor for solution processed device fabrication. In a second attempt, the chosen grid design was also applied by ink jet printing on top of glass as well as flexible substrates. The printed grid structures suffer from the line height of 300 nm and more, which is dramatic for the use in solution processed OLEDs. The same problems for the organic solar cell fabrication have also been reported by Galagan et al.[26]. Therefore, within final investigations methods for embedding the grid lines were tested.

The chosen grid design for all presented devices is depicted in figure 4.2. The grid geometry was chosen to be compatible with standard device design as presented in section 3.1.3. The honeycomb structure was chosen according to Galagan et. al because it provides more aesthetic view of the

devices [27], which is especially important if one is thinking about the application in displays. Li et al. [47] showed nice OPV devices using hexagonal grids with a line width of $3\text{ }\mu\text{m}$ and a $130\text{ }\mu\text{m}$ diagonal for each individual hexagon. This grid is nearly invisible for the human eye. For our first approach, a line width of $150\text{ }\mu\text{m}$ and a hexagon diameter of 3 mm have been used.

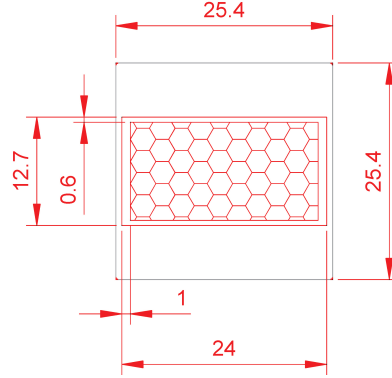


Figure 4.2: Chosen grid geometry (in mm).

All grids were printed using silver ink. This has several reasons, first silver is a widely known, commercially available, easy to handle ink for ink jet printing application. Moreover, the work function of (evaporated) silver with a layer of HC-PEDOT:PSS on top was measured to be 4.8 eV . This is nearly the same work function as for ITO combined with PEDOT:PSS (4.9 eV). Therefore the hole injection barrier into the active material is comparable. In figure 4.3 the corresponding UPS measurements are depicted. The work function of the used silver ink was measured to be 4.7 eV [65], according to this, printed silvers seems to be a ideal candidate.

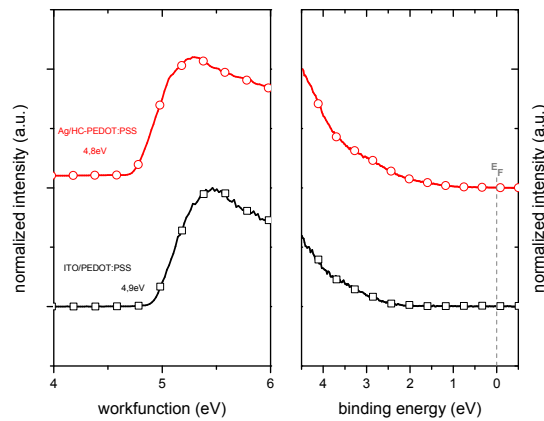


Figure 4.3: Secondary electron cut off (left) and valence region (right) UPS spectra for the standard anode stack - ITO/ PEDOT:PSS (black curves) and the new stack - silver/HC-PEDOT:PSS (red curve).

4.2 Photolithographic grids

4.2.1 Fabrication

Silver metal grids with the design presented in figure 4.2 were structured using photolithography. The applied process is described in section 3.1.2.2, the used negative photo resist was AZ[®] nlof2035, the used parameters are summarized in table 3.2. The structuring was done using a chrome mask with a grid width of 150 μm . The successfully structured silver grid on PET substrate is depicted in 4.4. As can be seen, the average line width of the grid is indeed 150 μm , the silver height was 100 nm, for better adhesion 2 nm of chrome were evaporated between PET foil and silver.

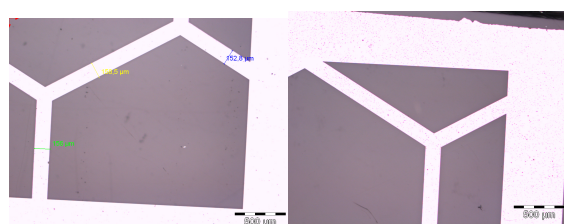


Figure 4.4: Microscope images of the evaporated silver grid structured by photolithography.

After the grid fabrication, the surface was plasma activated as described in section 3.1.3. In order to overcoat the 100 nm high structures, three layers of HC-PEDOT:PSS (*Clevios™* PH1000) have been spincoated on top. For HC-PEDOT:PSS the spin parameters were changed to 1500 rpm for 120 seconds. After 5 minutes drying time, the PEDOT:PSS layer was structured using deionized water and a cotton bun. Then the next layer was spin cast on top. This was done three time in a row before the substrate was dried on a hotplate at 110 °C for 10 minutes. In the end the PEDOT:PSS layer was just on top of the grid, the rest of the PEDOT:PSS layer on the sides of the substrate was removed before the drying step.

Photolithographically structured metal grids on PEN foil failed, as the metal was completely removed during the resist lift off.

4.2.2 Organic light emitting diodes utilizing grid-PEDOT:PSS double anode

On top of this silver grid HC-PEDOT:PSS double layer, the active layer assembly and the cathode have been applied. Parallel to this, also samples with the same active layer and cathode stack have been fabricated on ITO coated PET foil.

Evaporated OLED

A fully evaporated OLED was manufactured according to the previously described standard device assembly using TPD and Alq₃. A comparison of the device characteristics of both substrates is depicted in figure 4.5.

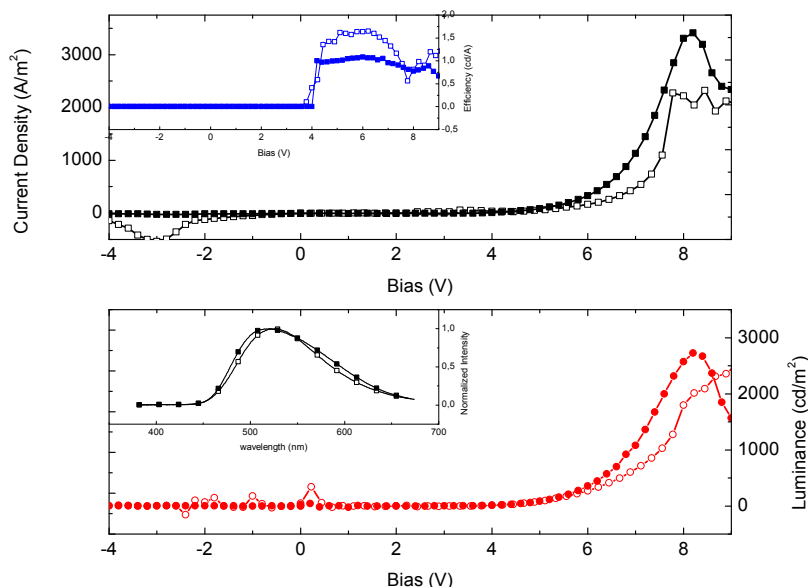


Figure 4.5: Device characteristics of evaporated OLEDs on top of silver grid plus HC-PEDOT:PSS (open symbol) compared to a reference device with ITO anode (closed symbol), both devices fabricated on PET foil. The upper graph shows the current density versus voltage curve for both samples, with a comparison of the overall device efficiency in the insert. The lower graph shows the luminance as a function of voltage for both devices, with the electroluminescence spectra for both devices in the insert.

As depicted in figure 4.5, both devices exhibit comparable spectra, with a peak maximum of 519 nm and 522 nm respectively. The device efficiency for the metal grid PEDOT:PSS anode device (1,65 cd/A) exceeds the achieved efficiency of the reference device (1 cd/A), although the maximum luminance is nearly the same. The reduced current density for the grid supported OLED is a result of the reduced hole injection into the device. The onset is at 3,7 V for both devices, but the gradient of the grid supported device is relatively low in the range of 4-7,5 V increasing dramatically in the range of 7,5 to 8 V. The reference device shows a breakthrough around 8 V, this seems to be a result of the scratchy and inhomogeneous ITO layer. The overall achieved luminance for both devices stayed approximately the same, whereas in contrast the current density is reduced by one third compared to the reference device. It can be concluded that the efficiency enhancement

is a result of the better charge carrier balance for the devices with the silver grid/HC-PEDOT:PSS anode structure.

Moreover, the transparency needs to be considered, as the grid lines reduce the active area. For the current density calculations, previously still the full active area was used. As depicted in figure 4.6, the grid lines, with the chosen linewidth of $150\ \mu\text{m}$, are clearly visible during the device operation. Also the heterogeneous luminance can be seen in figure 4.6, this is a result of higher hole injection from the silver lines then from the HC-PEDOT:PSS.



Figure 4.6: Images of an evaporated OLED with metal grid supported PEDOT:PSS anode under operation. The applied voltage was increased, with lowest applied voltage on the left side of the image (3,5-9 V).

From these results it can be concluded that a metal grid supported PEDOT:PSS anode layer is an appropriate alternative to ITO for flexible substrates. Nevertheless it needs to be mentioned that due to the difficulties of over coating a $100\ \text{nm}$ thick metal grid, the devices easily were shorted, once a voltage of more than $9\ \text{V}$ was applied.

Solution processed OLED

Also standard solution processed OLED (single layer device with ADS 232 as active material, see section 3.1.3) were fabricated on top of a metal grid supported PEDOT:PSS layer. In this case the active layer thickness is only half as thick as the evaporated stack, so a homogeneous film formation is essential for a proper device performance. Moreover it needs to be considered that spin coating is a good technique for a thin and homogeneous layer on top of a smooth surface. On a bumpy surface, like the $100\ \text{nm}$ thick evaporated grid, the uniform spreading of the polymer is crucial.

For a better device performance, the used HC-PEDOT:PSS was additionally modified with 5 %vol. dimethyl sulfoxide (DMSO). For better wetting, 15 %vol. isopropanol have been added. The fabrication was exactly the same as for pure HC PEDOT:PSS. The use of DMSO in order to increase the conductivity of HC-PEDOT:PSS was already performed by Do et al. [19], isopropanol was necessary to overcome the wetting problems, as described there as well.

In figure 4.7, microscope images of the solution processed devices are depicted. As can be seen on

the left side, the wetting of the modified PEDOT:PSS layer on top of the silver grids is sub-optimal, the film also shows different reflecting colors, which can be related to an heterogeneous film formation. The image in the middle shows a top view of one individual device. And still there, the anode grid is clearly visible. So the flattening of the anode structure was not possible, even though on top the active layer as well as the cathode have been applied on top. The left image in figure 4.7 shows the whole sample consisting of 8 individual devices.

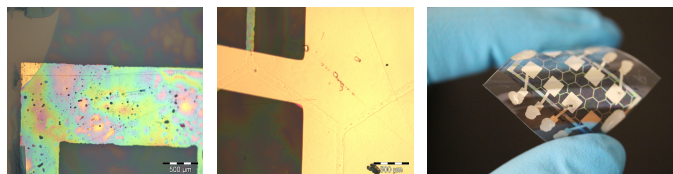


Figure 4.7: Microscope image of the modified HC-PEDOT:PSS on top of the silver grid (left), a microscope top view of one individual device of a solution processed OLED using a grid supported anode structure (middle) and a picture of the whole sample, consisting of 8 individual devices.

In figure 4.8 one fabricated solution processed OLED under operation is depicted, a homogeneous blue color at low operation voltages can be observed with a low luminance. At an operation voltage of 5V (right image in figure 4.8), just before the breakthrough, a homogeneous luminance can be observed, where the grid lines can no longer be identified due to the high intensity of the device. At lower operation voltages (other two pictures in figure 4.8) the anode grid can be clearly observed.

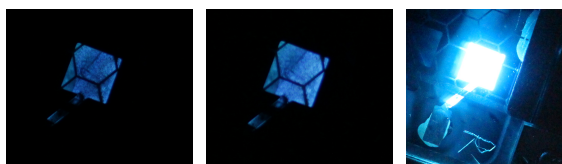


Figure 4.8: Images of a solution processed OLED with metal grid supported PEDOT:PSS anode under operation. The applied voltage was increased, with lowest applied voltage on the left side of the image.

The measured device characteristics for the solution processed OLED using a silver grid combined with modified HC-PEDOT:PSS as anode structure is depicted in figure 4.9. The device was bench marked with an anode structure consisting of modified HC-PEDOT:PSS only. As can be clearly seen in figure 4.9 the additionally used silver grid support increases the maximum luminance of the device by a factor of 100 (from 14,94 cd/m^2 for the device without the silver grid up to 1438,3 cd/m^2). As a consequence, also the efficiency of the LED is increased up to 0,07 cd/A . As already mentioned previously, the influence of the bumpy and heterogeneous surface, as a result of the 100 nm grid lines at the bottom, appeared even more problematic when OLEDs are processed from solution. So the low breakthrough voltage in the range of 5,5 to 6 V is a direct result of this. The low performance of the reference device can be explained by the high sheet

resistance of the modified HC-PEDOT:PSS, which limits the hole injection into the active material. The electroluminescence spectra of both devices exhibit the same shape with a peak maximum of 451 nm, for the reference device the spectrum was first measurable at an operation voltage of 8V.

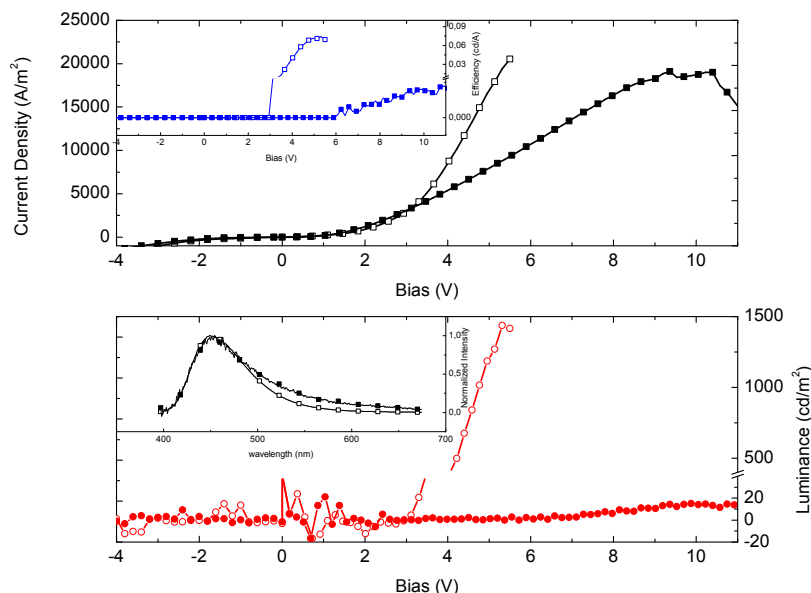
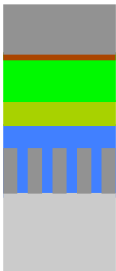





Figure 4.9: Device characteristics of solution processed OLEDs on top of silver grid plus modified HC-PEDOT:PSS, as described within the text (open symbol), compared to a reference device with only modified HC-PEDOT:PSS as anode (closed symbol), both devices fabricated on PET foil. The upper graph shows the current density versus voltage curve for both samples, with a comparison of the overall device efficiency in the insert. The lower graph shows the luminance as a function of voltage for both devices, with the electroluminescence spectra for both devices in the insert (at 5 V respectively 8V for the reference device).

So even though spin coating is difficult on top of the silver grid lines, the usage of an additional grid underneath the modified HC-PEDOT:PSS layer increases the device performance dramatically. Table 4.1 summarizes the key results of the fabricated OLED devices utilizing silver grid lines.

Table 4.1: Key results of the fabricated OLED devices utilizing silver grid lines including reference devices.

Device stack	Key results
 <p>Aluminum (~100nm) Calcium (~10nm) Alq3 (~100nm) TPD (~40nm) HC-PEDOT:PSS (~120nm) Grid (~100nm) PET foil</p>	<p>Onset: 3,7 V Maximum efficiency: 1,65 cd/A Maximum luminance: 2790,4 cd/m² Peak maximum CIE: x= 0,322 y=0,529 (at 5 mA)</p>
 <p>Aluminum (~100nm) Calcium (~10nm) Alq3 (~100nm) TPD (~40nm) PEDOT:PSS (~50nm) ITO (~120nm) PET foil</p>	<p>Onset: 3,7 V Maximum efficiency: 1,00 cd/A Maximum luminance: 2724,6 cd/m² Peak maximum CIE: x= 0,322 y= 0,529 (at 5 mA)</p>
 <p>Aluminum (~100nm) Calcium (~10nm) ADS 232 (~60nm) modified HC-PEDOT:PSS (~120nm) Grid (~100nm) PET foil</p>	<p>Onset: 3 V Maximum efficiency: 0,07 cd/A Maximum luminance: 1438,30 cd/m² Peak maximum CIE: x= 0,156 y= 0,096 (at 4 V)</p>
 <p>Aluminum (~100nm) Calcium (~10nm) ADS 232 (~60nm) modified HC-PEDOT:PSS (~100nm) PET foil</p>	<p>Onset: 6,5 V Maximum efficiency: $1 \cdot 10^{-3}$ cd/A Maximum luminance: 14,94 cd/m² Peak maximum CIE: x= 0,188 y= 0,163 (at 8 V)</p>

4.3 Printed grids

4.3.1 Fabrication

In order to fully solution process the transparent electrode, the same metal grid structure was also applied on the PET and PEN foil by ink jet printing. The used silver ink was purchased at Cabot.

Several printing resolutions have been tested, so that a continuous print image with a line width, as small as possible can be fabricated. The best results have been obtained using a resolution of 700 dpi. The residual solvent was removed drying the substrate in an oven at 150 °C for 2 h. Printing the silver grid on unmodified, standard cleaned PET foil failed, due to an insufficient contact angle the coalescence of the droplets was not achieved. Microscope images as well as a photography of the PET foil with the failed silver grid print are depicted in figure 4.10.

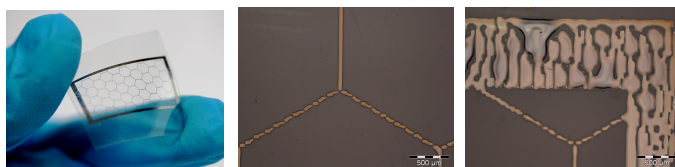


Figure 4.10: Photography of the silver grid printed on PET foil (left), microscopy images of the printed silver grid on PET (middle, left).

When PEN is used as a substrate ink jet printing the silver grid was sufficient. Microscope pictures for this case are depicted in figure 4.11.



Figure 4.11: Photography of the silver grid printed on PEN foil (left), microscopy images of the printed silver grid on PEN (middle, left).

The silver printing was also successful on standard cleaned glass substrate, good results were obtained using a resolution of 600 and 700 dpi, respectively.

4.3.2 Grid investigations

The profiles of the ink jet printed silver structures on PEN and glass were investigated using a profilometer. The average line width and high on several areas have been investigated. Silver grid lines on glass show an average line height in the range of 370 to 380 nm, a typical cross section profile of the silver ink on glass is depicted in figure 4.12. The line width was measured to be about 100 μm . Due to capillary forces, the grid lines connected to the busbar are thinner and show an average height in the range of 240 nm.

On PEN foil a disparate print pattern can be observed. The vertical lines show a nice homogeneous line with smooth edges, unfortunately due to the height amount of silver, the average line height

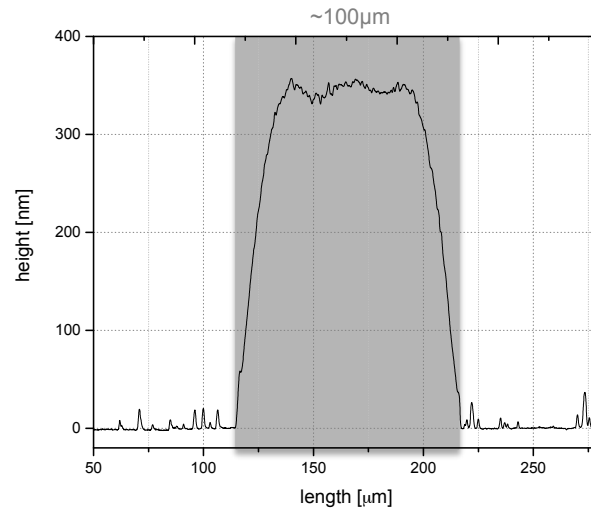


Figure 4.12: Cross section profile of the silver ink printed on glass using a resolution of 700 dpi.

was measured to be about 720 nm. The vertical lines in contrast show corrugated edges and an average line height of 450 nm to 480 nm. Again the lines close to the busbar showed a reduced average height, due to capillary forces. Figure 4.13 shows a microscope image of the silver lines on the PEN foil, there the different line shape between vertical and diagonal lines can be seen easily. A modification of the print file could change the line profile, but would also result in an increased profile height, as width and height of an inkjet printed line can not be changed independently [26]. The increased grid height is not desirable in the case of OLED fabrication and makes a device fabrication on top of the bare ink jet printed silver lines impossible.

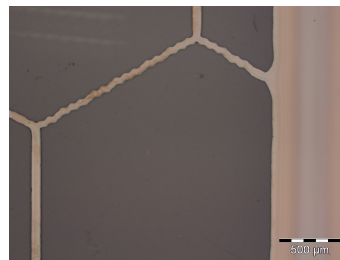


Figure 4.13: Microscope image of the silver ink printed on PEN using a resolution of 700 dpi.

4.4 Embedding the silver grid lines

4.4.1 Introduction and used material

As an average grid height of more than 300 nm is critical according to a good device fabrication on top and the reduction of line height and width is not possible independently, alternative approaches are necessary in order to fully use inkjet printed grid structures in OLED fabrication. Therefore embedding the grid lines is a good approach to address this problem in order to get thin but deep grid lines without significant height differences as well as a good conductivity. Also in literature several other groups were working on this problem. Van de Wiel et al. [72] and Galagan et al. [27] embedded screen printed silver lines with an average height in the range of 2000 to 4000 nm by using an donor substrate from which the silver profile was laminated on to a photo resist on top of a so called acceptor substrate. As this method is rather time consuming, an easier and faster method, that can be easily scaled up to larger dimensions is desirable.

The used embedding process in our approach is schematically depicted in figure 4.14. As can be seen in the scheme, the trench material works as an additional part of the substrate and should not influence the out coupling of the generated light.

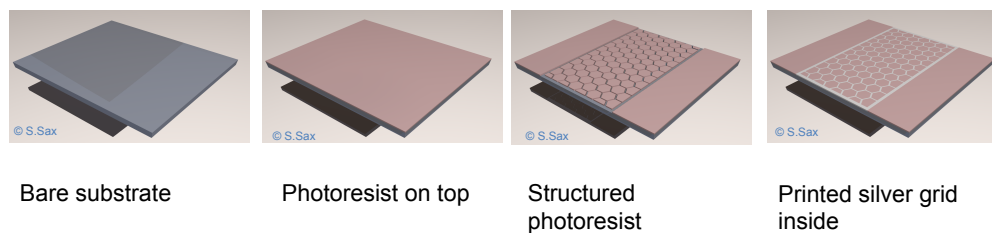


Figure 4.14: Scheme of the used embedding process.

The consequent requirements for a possible trench material are:

- Transparency in the visible range
- Easy structuring method that can be up-scaled to industrial scale
- High film thickness of at least 500 nm
- Long term stability of the transparency
- Good lateral resolution on flexible substrates and glass

The used material that obviously fits the requirements perfectly is the thick positive chemically amplified photo resist AZ[®] 40XT. The transparency of the exposed and unexposed photo resist was investigated using a UV-Vis Spectrometer (Shimadzu UV 1800). A good transmittance in the

visible range was observed, the measured transmittance is depicted in figure 4.15. Also the lateral resolution of the photo resist was tested on PET substrates and was determined with standard processing parameters, as described in the experimental section, to be in the range of $3\text{ }\mu\text{m}$, which is for the purpose of embedding the ink jet printed lines more than sufficiently.

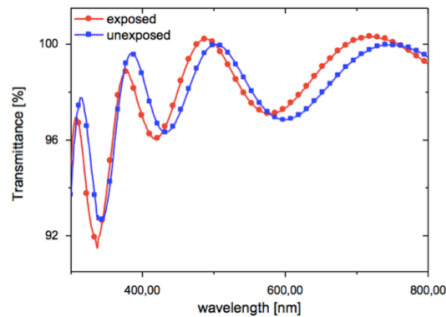


Figure 4.15: Transmittance of a quartz substrate with an approximately 500nm thick layer of 40XT.



Figure 4.16: Microscope picture of test line with minimal lateral resolution, using 40XT as a photo resist on PET foil, with the standard process parameters.

4.4.2 Results

The transparent trenches were fabricated using a custom made mask for the photolithography process. They were fabricated using a honeycomb mask, that is suitable for positive photolithography. Thus, the purchased honeycomb mask suitable for negative photo resists only was inverted, revealing the same average line width of approximately $150\text{ }\mu\text{m}$. The mask inversion was carried out using the positive photo resist (40XT) plus a lift off after an evaporation of a 70 nm thick gold layer, supported by a 3 nm chrome layer underneath for better adhesion. For the lift off, the remover NMP at $65\text{ }^{\circ}\text{C}$ was used, the substrate was immersed for 2 minutes. The resulting mask is depicted in figure 4.17.



Figure 4.17: Inverted photolithography mask for the fabrication of transparent trenches, with an average line width of $150\text{ }\mu\text{m}$.

The first tests all have been performed on glass, a transfer of the used system to PEN can be easily

carried out, as all process temperature are suitable for PEN foil applications. Microscope images of the fabricated trenches are depicted in figure 4.18. As can be seen clearly, due to the self made mask the trenches are interrupted at several places, this can cause problems when subsequently printing into the trenches. Moreover the profile of the trenches was investigated using a profilometer.

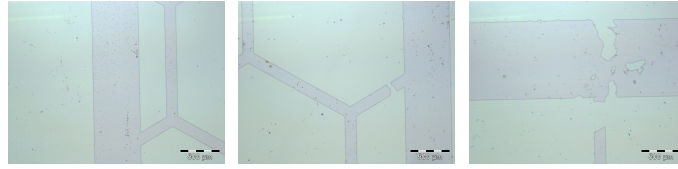


Figure 4.18: Microscope image of the structured trenches on top of glass.

As can be seen in figure 4.19 the line width is in the range of $150\ \mu\text{m}$ as expected due to the used mask. The line height was measured to be about $450\ \text{nm}$, this fits perfectly to the measured line height of silver lines on top of glass and especially PEN.

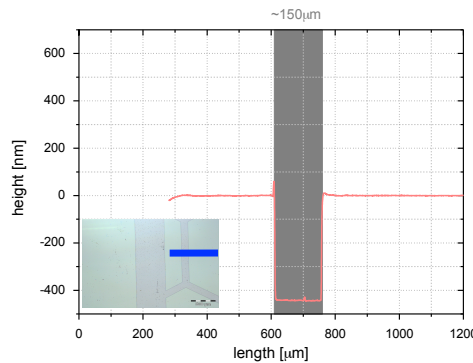


Figure 4.19: Cross section profile of the structured trenches on top of glass. The investigated area is depicted in the insert, the analyzed spot is marked with a blue line.

In order to get an estimation of the behavior of the silver ink combined with this new photo resist trenches, in a first attempt the silver grid was printed twice on the same trench system. Once the silver was printed directly into the trench (marked yellow) and once on top of the trench material (marked green). A microscope image of the resulting print is depicted on the left side of figure 4.20. Clearly the different behavior of the ink on top and inside the trenches can be observed. Moreover the bumpy edges of the printed silver are visible, also several defects in the silver lines (with a blister like shape) can be seen on the microscope image. Moreover it seems, that the silver spills over the edges of the trench system. For a better understanding, a profile of the analyzed system was investigated, the resulting profile is depicted on the right side of figure 4.20. In the profile an "edge effect", as we call the ink spreading over the whole edge, due to wetting behavior and surface tension of the ink, was clearly observed. Fortunately, in the center region the line height was reduced down to $200\ \text{nm}$. This is a reduction of nearly 50 %.

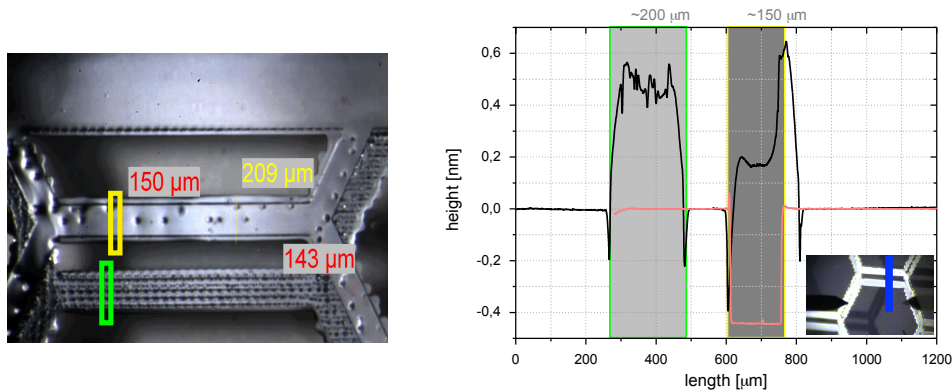


Figure 4.20: Microscope image of the silver ink printed into (marked yellow) and on top (marked green) of the trench structures (left). Profile of the embedded and on top printed silver grids. The analyzed area of the grid is shown in the insert, the investigated area is marked using a blue line. The trench is highlighted in pink (right).

The previously mentioned errors of the trench system have been additionally investigated after the printing process. As can be seen on the left side of figure 4.21, they definitely influence the layer profile. By investigating the profile with the microscope, another undesirable error was found. As depicted on the right side of figure 4.21, the size of the trench system and the print file mismatch. This is a consequence of the analog fabrication of the mask for the photolithography.

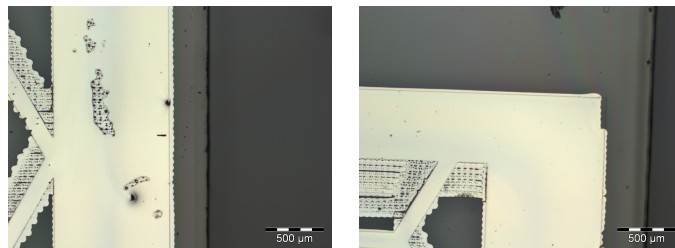


Figure 4.21: Microscope image of defects in the structured trenches (left), and of the upper right corner of the print file, where a mismatching of the file size for trench structure and the print file is noticeable (right).

In order to overcome this systemic error, a new mask was inkjet printed using the silver ink. The resulting mask is depicted in figure 4.22. The average line width of this mask is 200 μm with slightly bumpy edges but without any interrupted lines.

Moreover the file for the silver grid was modified, in order to reduce the individual pixel number, especially on the diagonal lines (lines only consisting of 1 dot) and therefore also to reduce the line width and line height. This was successful, as can be seen in figure 4.23, resulting in an average line width of only 80 μm, which is even less than the printing examples of silver lines on glass only

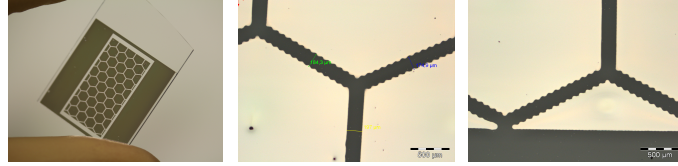


Figure 4.22: Inkjet printed mask for the fabrication of transparent trenches, with an average line width of $200\ \mu\text{m}$.

(see figure 4.12), the line height above the trench was measured to be between 150 and 250 nm. Despite the previously presented silver print in trench structures, this time no "edge effects" were observed, in contrast, this time the silver ink did not fill the whole trench fully.

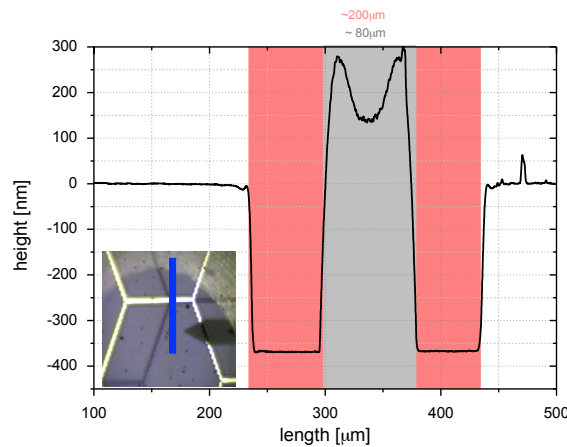


Figure 4.23: Profile of embedded silver grids. The silver printing was performed with 600 dpi using a print file with lines consisting of 1 dot only. The analyzed area of the grid is shown in the insert, the investigated area is marked using a blue line. The trench is highlighted in pink, whereas the silver line is highlighted in light gray.

According to these results, with this new, easy and straight forward embedding idea a good reduction of the line height of printed structures can be observed. However, fine tuning is still tricky, especially the ideal trade off between fully filled trenches and undesired "edge effects" is a key issue. With a good adjustment between printing resolution and trench width it needs to be guaranteed, that no ink spills over the trench. Moreover, partial surface modifications could be a good method to improve the previously explained technique. Another way could be the simultaneous inkjet printing of the trench material and the silver grids. Therefore the behavior of the photo resist upon ink jet printing needs to be tested extensively (i.e. surface tension, viscosity).

4.5 Conclusion

Replacing ITO with a silver grid in combination with HC-PEDOT:PSS was investigated to be an extremely efficient method. For devices using evaporated small molecules as active layer better efficiency was achieved when ITO was replaced by a lithographically structured silver grid. In this case it was found, that the efficiency enhancement is a direct result of the better charge carrier balance. In the case of solution processed conjugated polymer materials as active layer the silver grid anode covered with HC-PEDOT:PSS was compared to an anode consisting simply of HC-PEDOT:PSS. Here again a large increase in the efficiency was observed. The better hole injection was found responsible for the increasing of all important device parameters this time. All relevant device results with or without silver grids on top of PET foil are summarized in table 4.1. Still the spin coating on top of the grid lines was found to be tricky, as a homogeneous film formation is nearly impossible on silver grids with a height of 100 nm. Another important issues according to the device fabrication is the transparency of the anode using silver grids. A reduced grid width with a constant device behavior would be desirable.

When replacing the lithographically structured silver grid by an inkjet printed grid, the fabrication process is simplified and the fabrication costs are significantly reduced. Inkjet printing silver on top of a rigid sample was carried out. Moreover a fabrication on flexible substrates was realized. The print profile was found to be different, when fabricating the inkjet printed silver grid on top of PEN foil instead of glass. Optimizing the inkjet printed grid, by varying the print parameters, a minimal grid height of 370 nm was measured. On PEN foil the minimal grid height was even more than 700 nm. On top of grid structures with a height profile like this, fabricating a device was not possible at all. Therefore in a next step the silver grid was embedded into a transparent trench system. Such thin but deep grid lines can be realized and still a fabrication on top is possible without a bumpy surface. The thick positive chemically amplified photo resist AZ[®] 40XT was found to be perfectly suitable for the fabrication of fine structured and transparent trenches. The trenches fabricated on glass showed an average depth of 350 to 400 nm and a width of 150 to 200 μm . The silver ink was then directly printed into the transparent trenches. Profiles of these embedded silver grids are depicted in figure 4.23 and 4.20. Clearly a reduction of the average line height was investigated. According to these results, the new easy and straight forward embedding idea seems to be a good way to reduce the line height of printed structures. However the fine tuning is still tricky, especially the ideal trade off between fully filled trenches and undesired "edge effects" is a key issue.

5 CESIUM STEARATE AS SPIN COATED CATHODE INTERLAYER

5.1 Introduction and layer formation

As already mentioned in the fundamentals, a good charge carrier injection into the active material influences the device efficiency dramatically. Especially the good electron injection from the cathode into the LUMO of the active material is, due to the higher injection barrier, hard to achieve. In general, the height of the injection barrier for the electrons is determined by the work function of the cathode material, the LUMO level as well as eventually occurring dipole barriers at the interface [21]. Also an ohmic interface is preferable, so that the necessary driving voltage is as low as possible.

Ever since low work function materials and alloys are known for an enhanced electron injection [42], the problem they are unfortunately suffering from is their strong reaction to oxygen and moisture. So in general for OLED fabrication a cathode bilayer with a low work function material or alloy in combination with a thick layer of aluminum or silver is used. First this bilayer concept was introduced by Hung et al. [36]. In the past a lot of different low work function metals (Cs, Na, Mg, Ca, Ba), metal fluorides (LiF, CsF) [36], metal oxides (MgO) [17] and organic metal complexes (Ca(acac)₂, NaSt) [80], [61] were tested.

Recently, evaporated metal salts like cesium carbonate were used as low work function materials, and tremendous efficiency enhancements have been observed, for example by Nau et al. [51]. Even though the results clearly state a large device improvement, when Cs₂CO₃ is used, the electron injecting mechanism is still not clearly understood. Within the scientific community, heavy discussion is still ongoing. Whereas some groups explain the increased electron injection to the formation of a Cs complex [35], others point out that a thermally driven decomposition of the cesium carbonate during the evaporation takes place and some sort of n-doping with free cesium is the reason for the improved performance [46]. In contrast to LiF, where a chemical reaction of the

LiF/aluminum interface was investigated to be the origin of the improved device efficiency [74], cesium carbonate does not require a subsequent aluminum layer for a good electron injection, and therefore also other materials can be used on top [16]. This is especially important when combining with ink-jet techniques, as up to now no aluminum ink is available on the market.

Most of the known cathode materials are fabricated by vapor deposition. Despite this, the key issues to enter the large market of flexible, low cost devices are low material costs and simple processing conditions. Fabricating the cathode from solution is therefore important to reduce the fabrication costs of the devices. The crucial point about this is especially to get a good charge carrier injection from the electrode by a material that can be solution processed.

Cesium carbonate was fabricated in the past from solution as well, due to the good device results when using evaporated cesium carbonate a more than reasonable idea. Unfortunately cesium carbonate only shows proper film formation when spin coated from 2-ethoxyethanol, a toxic solvent[34]. Therefore in 2013 Wetzelaer et al. fabricated OLEDs using cesium stearate and achieved good results by spin coating cesium stearate (CsSt) using ethanol as a solvent. Inspired by these first results, the aim within this thesis was to use cesium stearate (CsSt) as an interlayer and get a deeper understanding of the layer formation and the energy level alignment as well as the compatibility with several active materials. A recent report for other organic metal complexes (NaSt) showed good device results [61] as well. Wetzelaer et al. related the efficiency increase to a LUMO pinning and a resulting ohmic contact. Despite this, for NaSt [61] the performance enhancement was explained by a thin insulation layer and therefore as a superposition of three effects: the increased electron injection (tunneling barrier), the additional hole blocking functionality and the reduced quenching at the Al interface, see Xu et al. [80] for further explanation. By UPS measurements a deeper understanding of this topic was reached.

Cesium stearate was fabricated by the company AGLYCON Dr. Spreitz KG [4] according to the patent by Kanitz et al. [39]. Corresponding to the process description by Kanitz et al. [39] the cesium stearate was produced by adding a mixture of Cs_2CO_3 and stearic acid in the ratio 1:2 to butanol, the mixture was kept at reflux temperature until CO_2 formation stopped. Finally, butanol was separated on the rotary evaporator and the residue was mixed with ether and aspirated [39]. In figure 5.1 the main step of the synthesis is depicted.

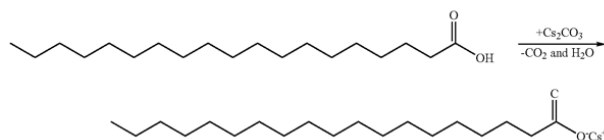


Figure 5.1: Embodiment of the synthesis of cesium stearate. The final chemical structure is already cesium stearate, consisting of a long hydrocarbon chain ($C_{17}H_{35}$) and the polar head (COO^-Cs^+). Taken from [39].

Layer formation

As already described previously, when manufacturing multilayer devices all from solution, the subsequent application of one layer on top of the other is quite a crucial point, especially when two materials are soluble in the same solvent. In order to address these issues, a careful material choice is essential. When spin coating a cathode interlayer from solution as well, the same issue is important. Basically in literature there are four strategies to tackle this issue: Using a hard bake step in order to stabilize the layer (as already described for TFB) [41], the use of cross linkable polymers [53] or buffer layers [69] between two layers spin coated from the same solvent, or the so called orthogonal solvent approach [57], [33], where alternately materials soluble in polar and unpolar solvents are used in order to avoid dissolving. This method was also chosen for cesium stearate. As most active materials are soluble in unpolar solvents, the solution processed cathode interlayer used on top needs to be soluble in a polar solvent. Due to the hydrophilic head and the long unpolar alkyl chain Cesium Stearate perfectly matches these requirements.

Cesium stearate was deluted to a concentration of 2 g/l (according to [77]) in ethanol. In order to estimate the relation between spin parameters and layer thickness the cesium stearate layer was spin coated on top of ordinary polyfluorene with varying spin parameters. The cesium stearate was spin coated using a two-step process. Whereas the spinning rate of the film forming step was modified from 500 rpm up to 3000 rpm (lasting for 12 s each), the subsequent drying step with 3000 rpm for 40s was kept constant. The resulting films have been investigated with an AFM. The measured surface topologies and height profiles of selected spin parameters are depicted in figures 5.2 - 5.4. As can be seen, the cesium stearate coverage on top of polyfluorene increases with increasing spin parameters. Also the average roughness decreases, the RMS-surface roughness for the $25 \times 25 \mu m$ scan reduces from 19,3 nm (for 500 rpm) to 12,2 nm (for 3000 rpm). This can also be explained when looking at the height profiles. In the case of a slow spin rate it seems like the individual cesium stearate flakes are more likely to stack on top of each other. It is coherent that the lowest layer thickness for cesium stearate was achieved using a spin rate of 3000 rpm for 60 seconds.

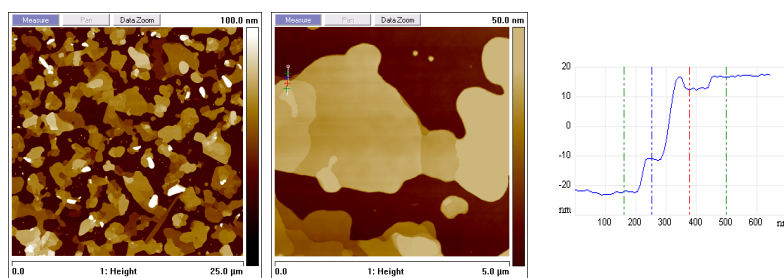


Figure 5.2: AFM surface topography images 25 x 25 μm and 5 x 5 μm measured in tapping mode and measured height profile (right image) for cesium stearate on top of polyfluorene with a spin speed of 500 rpm. The RMS-surface roughness for the 25 x 25 μm amounted to 19,3 nm.

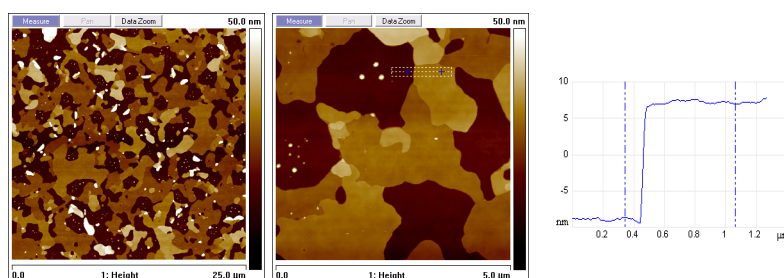


Figure 5.3: AFM surface topography images 25 x 25 μm and 5 x 5 μm measured in tapping mode and measured height profile (right image) for cesium stearate on top of polyfluorene with a spin speed of 2000 rpm. The RMS-surface roughness for the 25 x 25 μm amounted to 12,9 nm.

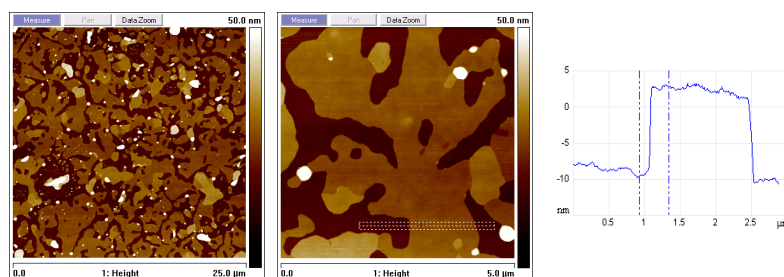


Figure 5.4: AFM surface topography images 25 x 25 μm and 5 x 5 μm measured in tapping mode and measured height profile (right image) for cesium stearate on top of polyfluorene with a spin speed of 3000 rpm. The RMS-surface roughness for the 25 x 25 μm amounted to 12,2 nm.

This is even more evident at the spin curve, which sets up a relationship between spin speed and layer thickness for a constant concentration. The spin curve is depicted in figure 5.5.

According to these results, all cesium stearate layers were spin coated from 2 g/l solution in ethanol with a spin rate of 3000 rpm for in total 52 seconds without any further processing.

5.2 Device performance of a polymer light emitting diode utilizing cesium stearate aluminum (evaporated) double cathode

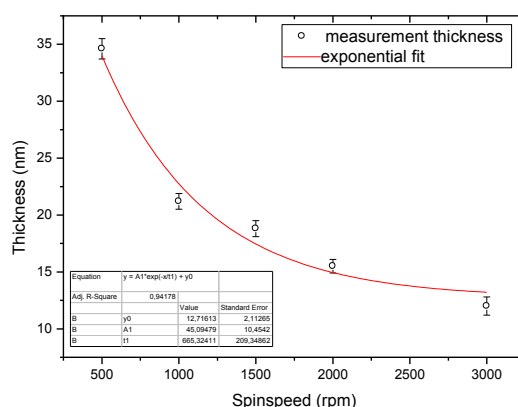


Figure 5.5: Spin curve for 2 g/l cesium stearate solution in ethanol, setting up a relation between spin speed and resulting layer thickness.

5.2 Device performance of a polymer light emitting diode utilizing cesium stearate aluminum (evaporated) double cathode

5.2.1 Device fabrication

Devices using ADS232 as active material were fabricated, as anode ITO with a smoothing layer of PEDOT:PSS was used. On the cathode side a double layer consisting of a thin cesium stearate (spin coated from 2 g/l with the spin parameters as described previously) and an evaporated 100 nm thick Aluminum layer was used. The fabricated devices have been benchmarked with a evaporated standard cathode consisting of 10 nm calcium and 100 nm aluminum.

In order to optimize the anode energy level alignment, an additional layer of TFB was spin coated on top of PEDOT:PSS. The layer formation is explained in the experimental section. For the multilayer approach also an optimized reference cathode was fabricated in order to bench mark the cesium stearate. Therefore a spin coated electron injection layer was applied between the active material and the standard calcium aluminum cathode. A PEG-PF (conjugated polyfluorene with poly(ethylene glycol) side chains) fabricated by the Institute of Professor Müllen (Max-Planck-Institut Mainz, Germany) was used, the chemical structure is depicted in figure 5.6. Figure 5.7 shows the normalized absorption and photoluminescence spectrum of PEG-PF [67]. As previously presented by members of our group [68], PEG-PF is perfectly suitable as electron transport layer. Due to the PEG side chains it is soluble in polar solvents, which allows orthogonal processing.

5.2 Device performance of a polymer light emitting diode utilizing cesium stearate aluminum (evaporated) double cathode

The PF facilitates the electron injection due to its proper energy levels [68]. The PEG-PF layer was spin coated from 1 g/l solution in methanol. The used spin parameters were 1500 rpm for 12 seconds for the layer formation and a subsequent drying step with 3000 rpm for 40 seconds. Prior to the deposition a spin rinsing step with methanol was performed (the substrate was spin rinsed with methanol, before the PEG-PF was spin coated on top) for better wettability. Afterwards the substrate was dried in vacuum at 60 °C for 30 minutes to remove the remaining solvent.

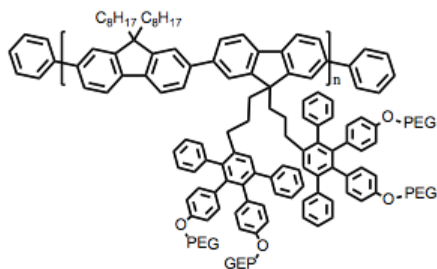


Figure 5.6: Chemical structure of PEG-PF, consisting of a conjugated polyfluorene with PEG (poly(ethylene glycol) side chains. Taken from [67].

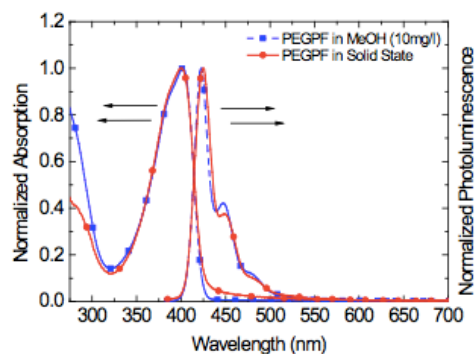


Figure 5.7: Normalized absorption and photoluminescence spectrum of a solid film of PEG-PF (red) and 0,1 g/l PEG-PF in methanol (blue). Taken from [67].

Moreover, the layer formation of cesium stearate on top of ADS232 was investigated with an AFM. As depicted in figure 5.8, again a flake like layer formation without full coverage can be observed. A smoother layer formation was observed when an additional spin rinsing step was performed to reduce possible wettability problems prior to the deposition of the next layer, as depicted in figure 5.9.

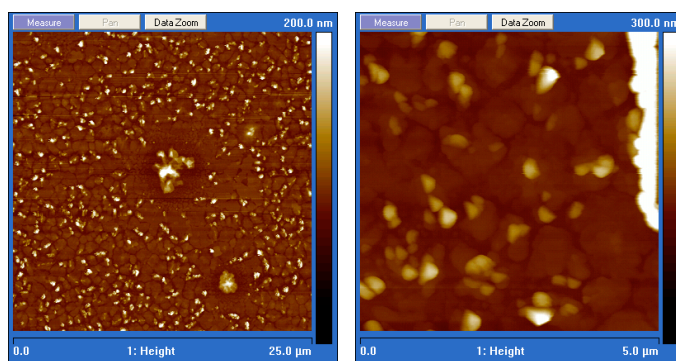


Figure 5.8: AFM surface topography images 25 x 25 μm and 5 x 5 μm measured in tapping mode for cesium stearate on top of ADS232.

5.2 Device performance of a polymer light emitting diode utilizing cesium stearate aluminum (evaporated) double cathode

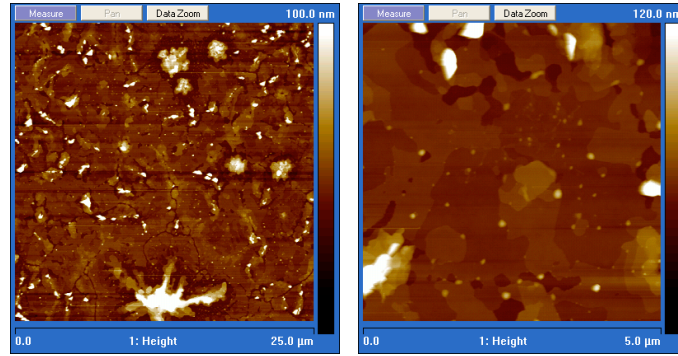


Figure 5.9: AFM surface topography images 25 x 25 μm and 5 x 5 μm measured in tapping mode for cesium stearate on top of ADS232 after an additional spin rinsing to achieve better adhesion and layer formation.

5.2.2 Device performance of single layer and multilayer devices

Single layer devices

First the device performance of single layer devices was investigated. For both devices, the thickness of the emitting layer was measured to be 50 nm. The anode and active layer fabrication of both devices was exactly the same, the only variation was that evaporated calcium was replaced by a spin coated cesium stearate layer. Figure 5.10 presents the J-V-L characteristics, the inset shows the electroluminescence spectrum at a current density of 1 kA/m^2 . The reference device with Ca/Al cathode is depicted on the top of figure 5.10, the device with cesium stearate interlayer is depicted on the bottom. When comparing the two characteristics it is found that the onset of the reference device is lower (3,0 V instead of 3,7 V), moreover the maximum luminance of the standard device is higher than for the bilayer cathode consisting of cesium stearate and aluminum. This would indicate a worse electron injection for cesium stearate than for calcium. As the cesium stearate layer formation for this device was observed to be non uniform, the higher onset and lower luminance in this case are a result of the poor film formation. Nevertheless the current density was extremely reduced when replacing calcium, a result of the better charge carrier injection. For both devices a bright blue emission was observed, the corresponding CIE coordinates for these emissions are depicted in the inset of the efficiency plot (table 5.2). Typically for this material a structureless emission peak around 455 nm is observable in the electroluminescence spectrum, also if cesium stearate is used, so CsSt has no influence on the spectrum of ADS232. The relevant device parameters (electroluminescence peak, onset voltage, maximum luminance) are summarized in table 5.1. Besides this, the efficiency values as a function of bias are depicted separately in table 5.2.

5.2 Device performance of a polymer light emitting diode utilizing cesium stearate aluminum (evaporated) double cathode

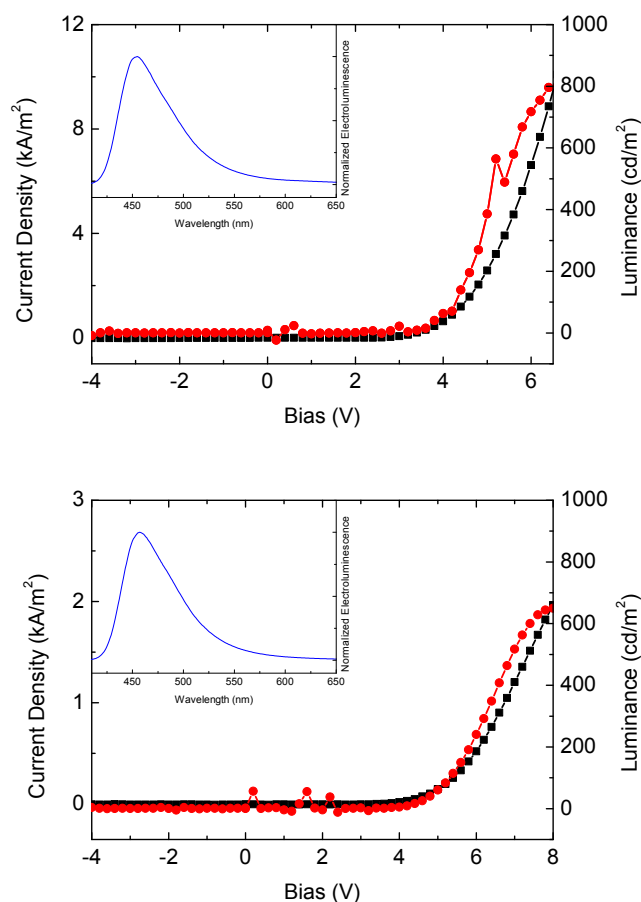


Figure 5.10: Current density (black) / luminance (red) as a function of the bias voltage in a ITO/PEDOT:PSS/ADS232/Ca/Al device (top) and a ITO/PEDOT:PSS/ADS232/CsSt/Al device (bottom). The insets show the electroluminescence emission spectrum of the devices at a current density of 1 kA/m².

The maximum device efficiency was increased by using cesium stearate from 0,180 cd/A to 0,460 cd/A, see also table 5.2. Moreover, a more homogeneous film formation for cesium stearate needs to be achieved by continuously stirring the CsSt before spin coating it.

Multilayer devices

In a multilayer approach also the energy level alignment at the anode side was optimized in order to further increase the device efficiency. Therefore TFB was used as hole transport layer. The layer thickness of TFB and ADS232 was measured to be 60 nm using a profilometer, after the hard bake the layer thickness of TFB was measured to be 5 nm using an AFM (see [67]). The corresponding

5.2 Device performance of a polymer light emitting diode utilizing cesium stearate aluminum (evaporated) double cathode

layer thickness for ADS232 on top of TFB was 55 nm.

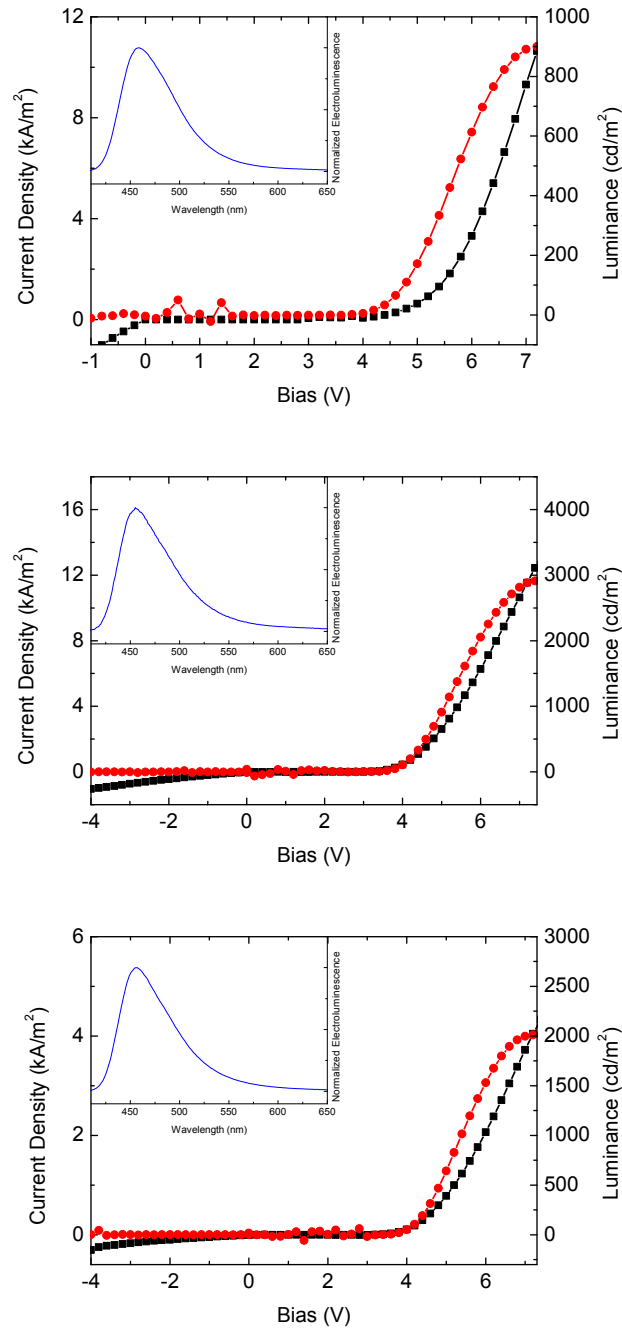


Figure 5.11: Current density (black) / luminance (red) as a function of the bias voltage in a ITO/PEDOT:PSS/TFB/ADS232/Ca/Al device (top), a ITO/PEDOT:PSS/TFB/ADS232/PEGPF/Ca/Al device (middle) and a ITO/PEDOT:PSS/TFB/ADS232/CsSt/Al device (bottom). The insets show the electroluminescence emission spectrum of the devices at a current density of 1 kA/m².

The slightly thicker active layer as well as the insertion of TFB had a dispensable influence on the emission color (CIE coordinates for Ca/Al top cathode at 1 kA/m²: single layer x= 0,160, y= 0,151 multilayer x= 0,153, y= 0,161). In order to get more information on the electron injection from CsSt into ADS232 also a multilayer device using PEG-PF as an additional electron injection layer was inset. For all three multilayer devices, a similar bright blue emission was found, the corresponding CIE coordinates for this emission are depicted in the inset of the efficiency plot (table 5.3). Figure 5.11 presents the J-V-L characteristics for all three device modifications, the inset shows the electroluminescence spectrum at a current density of 1 kA/m². The reference device with Ca/Al cathode is depicted on the top of figure 5.10, the device with an additional PEG-PF electron injection layer is depicted in the middle, the device with the cesium stearate interlayer is depicted on the bottom.

When comparing the reference device with the single layer reference first, a slight increase in the device efficiency is observable (maximum efficiency increased from 0,176 cd/A for the single layer device to 0,271 cd/A for the multilayer device). This can be explained by the increased luminance at a nearly constant current density, a direct result of the slightly better hole injection and/or electron blocking due to the additional TFB layer. When comparing the single layer to the multilayer devices with cesium stearate as cathode interlayer, the unexpected reduction of the onset for the multilayer device (from 3,7 V for the single layer device to 3,5 V), as well as the astonishing increase of the device luminescence (see table 5.1) are recognizable easily. One reason for this, is definitely the non uniform CsSt layer formation for the single layer device.

When comparing the multilayer devices the reference device exhibits by far the worse device performance. For the device with the additional PEG-PF layer, the highest luminance values were observed, still the maximum efficiency is less than half the value measured for the device with CsSt interlayer (0,352 cd/A compared to 0,829 cd/A). When using PEG-PF, the charge carrier injection is extremely unbalanced, revealed by the high value for the current density. The by far lowest current density was measured when cesium stearate was used as interlayer, this indicates an additional hole blocking functionality for CsSt, which would be in perfect agreement with the results observed by Siemund et al. [61]. Moreover the electron injection mechanism for CsSt was found to be worse than for PEG-PF in combination with the Ca/Al bilayer cathode, these results disagree with the results by Wetzelaer et al. [77]. More likely this is explainable following the theory of Xu et al. [80], that for insulation layers the efficiency enhancement is a combination of hole blocking, reduced quenching and enhanced electron injection. Xu et al. [80] explained the increased electron injection as a consequence of the accumulated holes near the active layer electron interface which "pull" the electrons into the active layer. From the first device results, this seems to be a quite realistic explanation for CsSt as well. The layer thickness of about 10 nm

5.2 Device performance of a polymer light emitting diode utilizing cesium stearate aluminum (evaporated) double cathode

for the CsSt layer somehow interferes the theory of electron pulling into the active material, as 10 nm are quite a distance to overcome for holes/electrons, but the noncontinuous CsSt layer might be the explanation why this still could be possible. A similar physical mechanism for CsSt and Cs_2CO_3 can be excluded, only by taking a close look at the device results. A definite explanation can of course only be given when looking at UPS/IPS measurements for a detailed picture of the individual energy layers. Unfortunately, IPS (inverse photoelectron spectroscopy) is hard to accomplish, as the organic layers get destroyed.

The relevant device parameters (electroluminescence peak, onset voltage, maximum luminance) are summarized in table 5.1. Besides this, the efficiency values as a function of bias are depicted separately in table 5.3.

Flexible substrates

Finally, single layer devices using cesium stearate as cathode interlayer have been fabricated on top of an ITO coated PET foil. Figure 5.12 presents the J-V-L characteristics, the inset shows the electroluminescence spectrum at a current density of 1 kA/m^2 . For the device on PET substrate the device characteristic was similar to the one fabricated on glass, the onset was determined to be at 3,5 V, a stable luminescence was achieved up to a bias voltage of 5,8 V. The maximum luminance was only halfe than for the same device fabricated on glass, moreover also the current density was doubled in the case of PET as substrate. Devices on flexible substrates as fabricated within this thesis clearly suffer from poor anode performance due to the high amount of scratches in the ITO on PET, also the film formation when spin coating the active layer is less homogeneous due to the non uniform vacuum exhaust.

Still a bright blue emission was found, the corresponding CIE coordinates for this emission are depicted in the inset of the efficiency plot (table 5.2).

The relevant device parameters (electroluminescence peak, onset voltage, maximum luminance) are summarized in table 5.1. Besides this, the efficiency values as a function of bias are depicted separately in table 5.2.

5.2.3 Comparing the device efficiencies

Next the device efficiencies of ADS232 as active material with and without cesium stearate as cathode interlayer are compared. The efficiency values as a function of bias voltage are compared

5.2 Device performance of a polymer light emitting diode utilizing cesium stearate aluminum (evaporated) double cathode

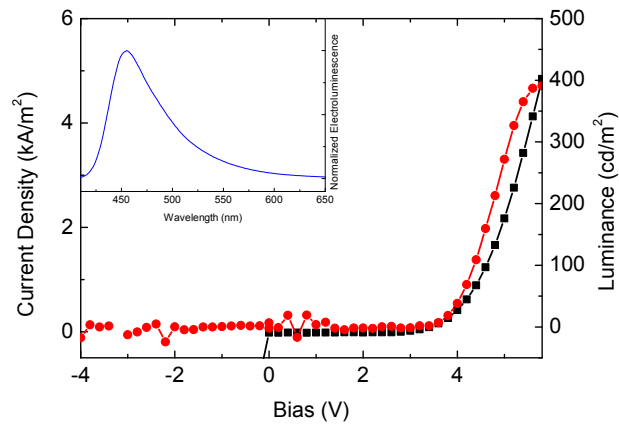


Figure 5.12: Current density (black) / luminance (red) as a function of the bias voltage in a ITO/PEDOT:PSS/ADS232/CsSt/Al device on a flexible PET substrate. The inset show the electroluminescence emission spectrum of the device at a current density of 1 kA/m².

Table 5.1: Comparison of the relevant device parameters (electroluminescence peak, onset voltage, maximum luminance) for all ADS232 devices.

Device stack (substrate/anode/[hole injection layer]/ active layer/[electron injection layer]/cathode)	Onset voltage ^a [V]	Maximum luminance ^b [cd/m ²]	EL peak ^c [nm]
glass/ITO/PEDOT:PSS/ADS232/Ca/Al	3,0	801	455
glass/ITO/PEDOT:PSS/ADS232/CsSt/Al	3,7	650	457
PET/ITO/PEDOT:PSS/ADS232/CsSt/Al	3,5	391	455
glass/ITO/PEDOT:PSS/TFB/ADS232/Ca/Al	3,5	900	455
glass/ITO/PEDOT:PSS/TFB/ADS232/CsSt/Al	3,5	2012	456
glass/ITO/PEDOT:PSS/TFB/ADS232/PEG-PF/Ca/Al	3,0	2912	455

^a voltage at a luminance of 1 cd/m²; ^b value of maximum efficiency; ^c at a current density of 1 kA/m²

to each other in table 5.2 for single layer devices and table 5.3 for multilayer devices. The device efficiency value is important especially from a customers point of view.

In table 5.2 the extreme increase of the device efficiency when cesium stearate is used instead of calcium is depicted. Besides this, also the relatively good results for the device fabricated on PET foil are visible. The best device operation voltage is visible in the range of 4,5-5 V for the Ca/Al cathode and CsSt/Al on PET and about 6 V for CsSt/Al on glass. The reduced ideal operation voltage on PET can be explained by the inhomogeneous film formation of the active layer as well as the scratchy ITO layer. Nevertheless the positive effect of cesium stearate on the device

5.2 Device performance of a polymer light emitting diode utilizing cesium stearate aluminum (evaporated) double cathode

operation of single layer devices with ADS232 as active material are obvious, even though from these results the primary mechanism is not clear, a better electron injection (see [77]) is a likely explanation.

Table 5.2: Comparison of the achieved device efficiency and CIE coordinates for the single layer ADS232 devices utilizing cesium stearate and the reference devices.

Device stack and used symbol	Efficiency and CIE coordinates
glass/ ITO/ PEDOT:PSS/ ADS232/ Ca/ Al	■
glass/ ITO/ PEDOT:PSS/ ADS232/ CsSt/ Al	◆
PET/ ITO/ PEDOT:PSS/ ADS232/ CsSt/ Al	×

When fabricating multilayer devices with cesium stearate, a maximum efficiency of 0,830 cd/A was achieved, this is depicted in figure 5.3. There the efficiency values as a function of bias voltage for the individual cathodes are compared. Here also a multilayer device with calcium aluminum bilayer cathode including an electron injection layer is depicted. Interestingly, the results for the device which uses cesium stearate instead of calcium exceeds the standard multilayer device with an additional electron injection layer by far. Then taking a look at the J-V-L characteristics, this can especially be described by the reduced current density, if cesium stearate is used. According to these results, it is suggested that cesium stearate has an additional hole blocking functionality.

Table 5.3: Comparison of the achieved device efficiency and CIE coordinates for the multilayer ADS 232 devices utilizing cesium stearate and the reference devices.

Device stack and used symbol	Efficiency and CIE coordinates
glass/ ITO/ PEDOT:PSS/ TFB/ ADS232/ Ca/ Al	■
glass/ ITO/ PEDOT:PSS/ TFB/ ADS232/ CsSt/ Al	◆
glass/ ITO/ PEDOT:PSS/ TFB/ ADS232/ PEGPF/ Ca/ Al	▲

5.3 Device performance of a dendrimer based light emitting diode utilizing cesium stearate aluminum (evaporated) double cathode

Starting from the first auspicious results when combining CsSt with ADS232, cesium stearate was now combined with a new dendrimer. First the photophysical properties of this new dendrimer material are summarized, then multilayer device results with and without CsSt are presented and the influence of CsSt on the device performance is discussed. Moreover UPS measurements were performed in order to get a deeper understanding of the efficiency increasing effect CsSt has on the device performance. This section finishes with a short summary as well as a short outlook.

5.3.1 Introduction to dendrimer materials

The basic concept of dendrimers was first developed by D. Tomalia [64] in 1985. In contrast to this, light emitting dendrimers are a relatively new class of active materials for OLED fabrication. Dendrimer materials try to combine the advantages of small molecules and polymers. Whereas small molecules achieve extremely high efficiencies, they suffer from the non solution processable layer application. Unlike small molecules, polymers can be processed from solution but exhibit lower efficiencies, a lower lifetime and large batch to batch variations [20]. So in principle, light emitting dendrimers are an attempt to solution process small molecule materials, they consist of a small molecule material (as a core) one or several generations of dendrons (so called shell) and a final surface group. The charge carrier injection is mostly provided by these surface groups. Due to this layer by layer design, dendrimers are easy to synthesize and a perfect shape-persistent can be achieved, it is also easy to place functional groups, like surface groups, at specific places. The shape-persistence moreover reduces the possibility of agglomerate formation [11]. Dendrimers can be easily fabricated by the so called Diels-Alder cycloaddition. The dendritic architecture used for these materials makes an individual control of the device properties and the material processing possible [11]. An efficient energy transfer from the surface moieties to the chromophore in the core needs to be guaranteed by a proper choice of the used surface groups [11].

5.3.2 Photophysical properties and device performance for PYCAB

The photophysical properties of PYCAB (dendrimer with a pyrene core, one generation of polyphenylenes and carbazole as surface groups) have been analyzed by M. Auer in his master thesis [11] and are depicted in figure 5.14 in order to get an idea what emission is expected. The chemical structure of PYCAB consists of a pyrene core, a shell of polyphenylene and hole transport moieties and is depicted in figure 5.13. From the measured photoluminescence, an emission only from the pyrene core is observed (see [11] for more details). The presented dendrimer was synthesized at the Max-Planck Institute of Polymer Research in Mainz, Germany by the group of Prof. Klaus Müllen.

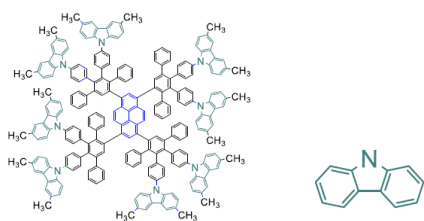


Figure 5.13: Chemical structure of PYCAB, consisting of an emissive pyrene core, one generation of polyphenylene acting as the shell and carbazole surface groups (hole transport moieties, in turquoise). Taken from [11].

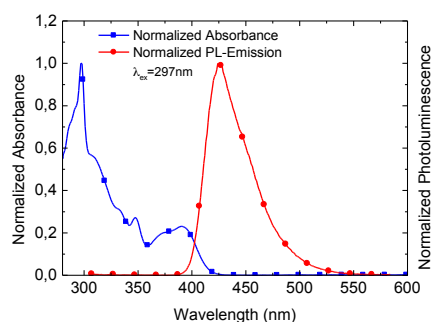


Figure 5.14: Normalized absorption and photoluminescence spectrum of 0,1 g/l PYCAB in tetrahydrofuran (THF). Taken from [11] and modified.

Single layer device

The device performance of PYCAB was tested in a standard single layer device on glass. The PYCAB was therefore spin coated from a 5 g/l solution in THF. The used standard spin parameters for polymers pin coated from THF were 1500 rpm for 12 seconds followed by a drying step with 3000 rpm for 40 seconds. Afterwards the substrate was dried at 80 °C for 30 minutes in vacuum to remove the remaining solvent. For this concentration, the layer thickness was estimated to be about 50-60 nm, which is in the ordinary range. The other layers were fabricated as already described previously. Figure 5.15 presents the J-V-L characteristics, the inset shows the electroluminescence spectrum at a current density of 1 kA/m². The standard single layer device using PYCAB as active

5.3 Device performance of a dendrimer based light emitting diode utilizing cesium stearate aluminum (evaporated) double cathode

material exhibits a low maximum luminance of 336 cd/m^2 at a current density of 16,5 kA/m^2 . A maximum device efficiency of 0,02 cd/A was achieved. Besides the relatively low efficiency, also the onset of the device was undesirably high (5,4 V). The bad charge carrier injection for the single layer is expected to be responsible for this high onset. As PYCAB has some hole transport moieties at the surface groups, the electron injection is expected to be problematic.

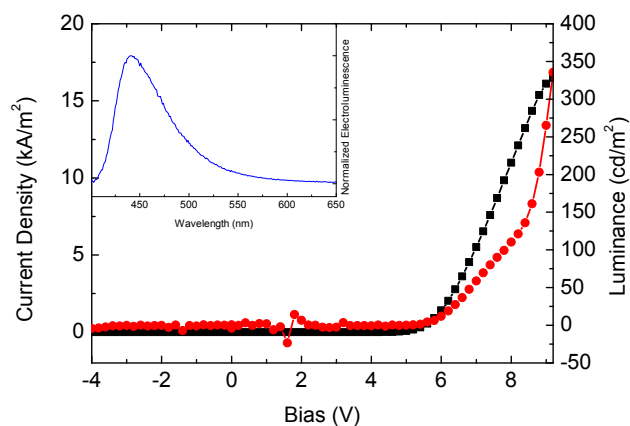


Figure 5.15: Current density (black) / luminance (red) as a function of the bias voltage in a ITO/PEDOT:PSS/PYCAB/CsSt/Al. The inset shows the electroluminescence emission spectrum of the device at a current density of 1 kA/m^2 .

5.3.3 Device performance of multilayer devices

In a multilayer approach, also the anode side was optimized in order to get an indication if the hole injection is problematic, too. Therefore, TFB was used as hole transport layer, with the same layer thickness as described previously. The active layer thickness was measured to be the same as for the single layer device. Nevertheless the insertion of TFB had a small influence on the emission color (CIE coordinates for single layer $x=0,161$, $y=0,114$, for the multilayer $x=0,162$, $y=0,139$), also for the electroluminescence peak a red shift was observed. The peak maximum at a current density of 1 kA/m^2 was increased from 440 nm to 450 nm when inserting TFB, see insets of the figures in 5.16.

Figure 5.16 presents the J-V-L characteristics for all three device modifications, the insets show the electroluminescence spectrum at a current density of 1 kA/m^2 . For a better understanding of the influence of CsSt on the device performance, again a multilayer device using PEG-PF as an additional electron injection layer was fabricated as well. The reference device with Ca/Al cathode is depicted on top of figure 5.16, the device with an additional PEG-PF electron injection layer is

5.3 Device performance of a dendrimer based light emitting diode utilizing cesium stearate aluminum (evaporated) double cathode depicted in the middle, the device with the cesium stearate interlayer is depicted on the bottom.

When comparing the reference device with the single layer reference first, only a small improvement of the device efficiency is observable (maximum efficiency increased from 0,02 cd/A for the single layer device to 0,05 cd/A for the multilayer device), also the maximum luminance was not increased significantly by using TFB as hole injection layer (maximum luminance of 336 cd/m² for the single layer device to 353 cd/m² for the multilayer device). Only the shoulder of the luminance at about 7 V can not be observed for the multilayer device anymore, moreover, the multilayer device shows a stable operation up to about 12 V. Unfortunately, the usage of TFB increases the onset again (from 5,4 V to 6 V). Therefore the better hole injection into the HOMO of the PYCAB was not observed, rather than this, the insertion of TFB has a positive influence on the device stability. Due to microscope images, this is attributed to the better film formation of PYCAB on top of TFB.

Comparing the multilayer devices the extremely high onset for the CsSt device is noticeable at first, compared to the reference device the onset increases by 4 V (from 6 V to 10 V), in contrast the onset for the device with the additional PEG-PF layer is only increased moderately (onset at 7 V). Nevertheless, the current density is extremely high (maximum current density of 14,5 kA/m²) for the standard device, together with the low luminance (maximum luminance of only 353 cd/m²) the achieved maximum efficiency is very poor (0,046 cd/A), see also table 5.5. This indicates that the insertion of TFB does not influence the device performance at all, the already discussed issues concerning the device characteristic in the single layer approach are valid also now. Besides the negative effect of increasing the onset, the insertion of CsSt as well as using PEG-PF reduces the current density significantly (maximum current density of 8,9 kA/m² for CsSt device, 5,9 kA/m² for PEG-PF device). This once more would be a good explanation for the good hole blocking functionality of CsSt, which seems to influence the PYCAB device efficiency positively as well. When using PEG-PF, the best luminance values for PYCAB were achieved indicating that the electron injection from PEG-PF works better than with CsSt. The lowest onset for the standard device indicates that the work function of calcium matches the PYCAB LUMO best, but due to a missing electron injection/hole blocking layer, still a lot of holes leave the active layer without recombining with the electrons. Coherently the standard device using PEG-PF as EIL had the best efficiency values, see table 5.5. The location of the PYCAB LUMO seems to be unfavorable for all tested cathode modifications, revealing a high onset for all devices.

For all three multilayer devices the same blue emission was found, the corresponding CIE coordinates for this emission are depicted in the inset of the efficiency plot (table 5.5). The relevant device parameters (electroluminescence peak, onset voltage, maximum luminance) of all PYCAB devices are summarized in table 5.4. Besides this, the efficiency values as a function of bias are

5.3 Device performance of a dendrimer based light emitting diode utilizing cesium stearate aluminum (evaporated) double cathode

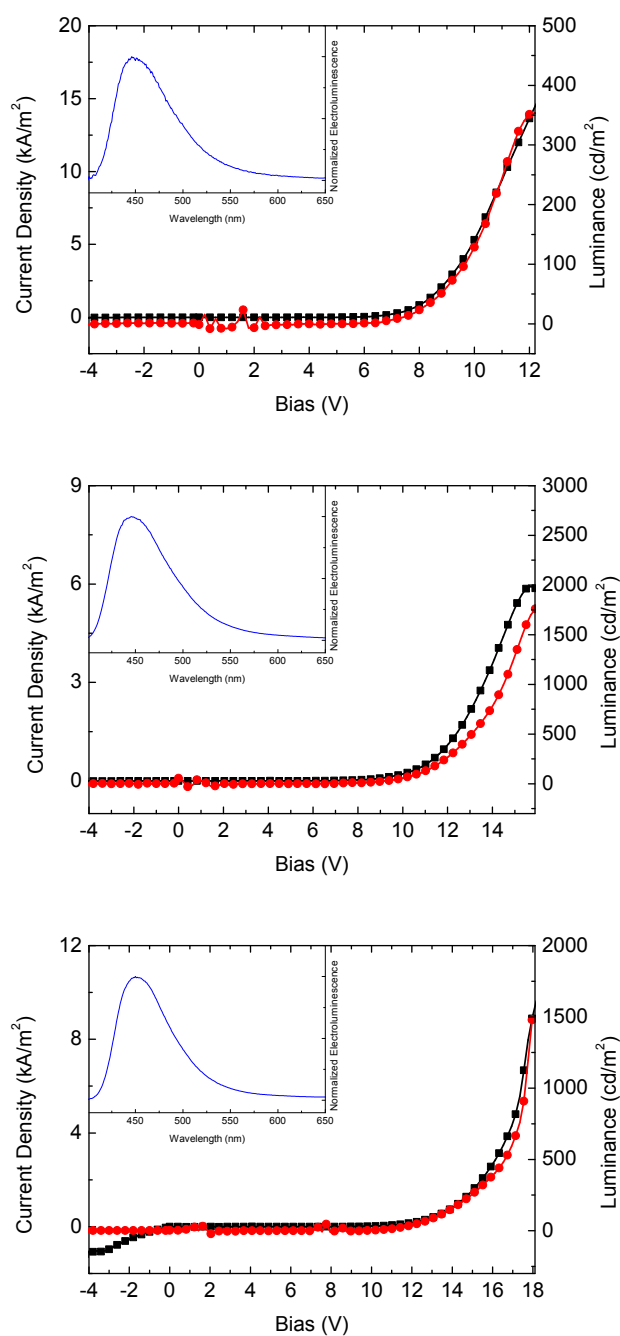


Figure 5.16: Current density (black) / luminance (red) as a function of the bias voltage in a ITO/PEDOT:PSS/TFB/PYCAB/Ca/Al device (top), a ITO/PEDOT:PSS/TFB/PYCAB/PEGPF/Ca/Al device (middle) and a ITO/PEDOT:PSS/TFB/PYCAB/CsSt/Al device (bottom). The insets show the electroluminescence emission spectrum of the devices at a current density of 1 kA/m².

5.3 Device performance of a dendrimer based light emitting diode utilizing cesium stearate aluminum (evaporated) double cathode depicted separately in table 5.5.

Table 5.4: Comparison of the relevant device parameters (electroluminescence peak, onset voltage, maximum luminance) of all PYCAB devices.

Device stack (substrate/anode/[hole injection layer]/ active layer/[electron injection layer]/cathode)	Onset voltage ^a [V]	Maximum luminance ^b [cd/m ²]	EL peak ^c [nm]
glass/ITO/PEDOT:PSS/PYCAB/Ca/Al	5,4	336	440
glass/ITO/PEDOT:PSS/TFB/PYCAB/Ca/Al	6,0	353	449
glass/ITO/PEDOT:PSS/TFB/PYCAB/CsSt/Al	10,0	1479	450
glass/ITO/PEDOT:PSS/TFB/PYCAB/PEG-PF/Ca/Al	7,0	1778	452

^a voltage at a luminance of 1 cd/m²; ^b value of maximum efficiency; ^c at a current density of 1 kA/m²

Table 5.5: Comparison of the achieved device efficiencies and CIE coordinates for the multilayer PYCAB devices utilizing cesium stearate and the reference devices.

Device stack and used symbol	Efficiency and CIE coordinates
<div> <div>glass/ ITO/ PEDOT:PSS/ TFB/ PYCAB/ Ca/ Al</div> <div>glass/ ITO/ PEDOT:PSS/ TFB/ PYCAB/ CsSt/ Al</div> <div>glass/ ITO/ PEDOT:PSS/ TFB/ PYCAB/ PEGPF/ Ca/ Al</div> </div> <div> <div>■</div> <div>◆</div> <div>▲</div> </div>	

Time dependent spectral behavior

Also the influence of CsSt on the time dependent spectral behavior of the devices was analyzed. Therefore the luminance of a device at a constant current density was measured in a short interval for a period of 5 minutes. The measured time dependent spectrum for the standard multilayer device, compared to the multilayer device using CsSt are depicted in figure 5.17.

According to figure 5.17 the insertion of CsSt does influence the emission spectrum as already described previously, but no change in the emitted color can be observed over time, so a stable device operation is possible using PYCAB combined with CsSt, only the emission is slightly red shifted.

5.3 Device performance of a dendrimer based light emitting diode utilizing cesium stearate aluminum (evaporated) double cathode

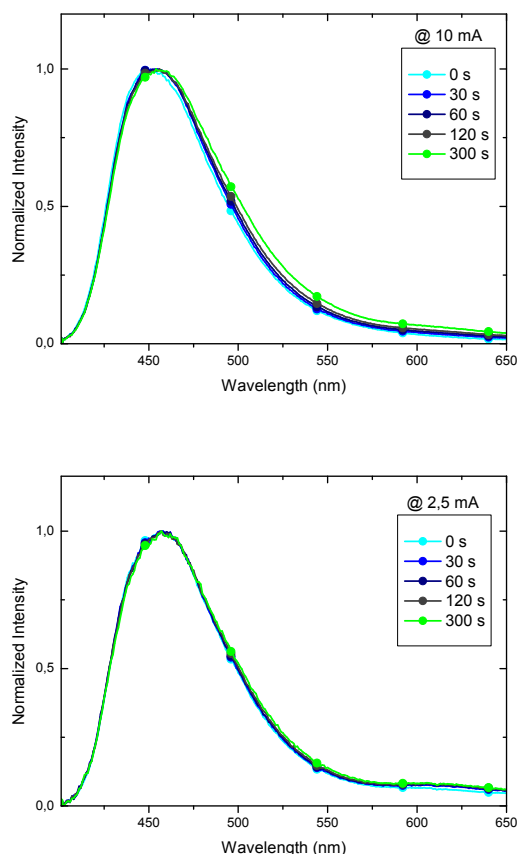


Figure 5.17: Electroluminescence emission spectrum of ITO/PEDOT:PSS/TFB/PYCAB/Ca/Al device (top), and ITO/PEDOT:PSS/TFB/PYCAB/CsSt/Al device (bottom) at a constant current density measured over 5 minutes continuous operation. The applied current is written inside the individual graphs.

5.3.4 UPS studies on PYCAB cesium stearate interface

In order to explain the increased efficiency and maximum luminance of the devices when using cesium stearate as well as the dramatically increased onset, the device interfaces have been investigated using ultraviolet photo electron spectroscopy (UPS). UPS gives the possibility to measure the energy levels. The corresponding UPS data for the single layer device using cesium stearate as electron interlayer are depicted in figure 5.18. In this case especially the cathode energy barriers between PYCAB and CsSt is investigated. Comparing the UPS data for PYCAB with (green curve) and without (blue curve) cesium stearate, at the first glance no significant change in the UPS spectrum can be observed. Looking at the low binding energy region (valence band; left side of figure 5.18) both times the same two rather small features are visible. So clearly the

5.3 Device performance of a dendrimer based light emitting diode utilizing cesium stearate aluminum (evaporated) double cathode

ionization energy for PYCAB can be determined with 5,8 eV and 7,15 eV. The 5,8 eV can be attributed to the HOMO level of the pyrene core of the dendrimer. This fits the results observed by Qin et al. [55]. From these results one can conclude that the hole injection barrier at the anode side is relatively high, a possible explanation for the high onset of the device.

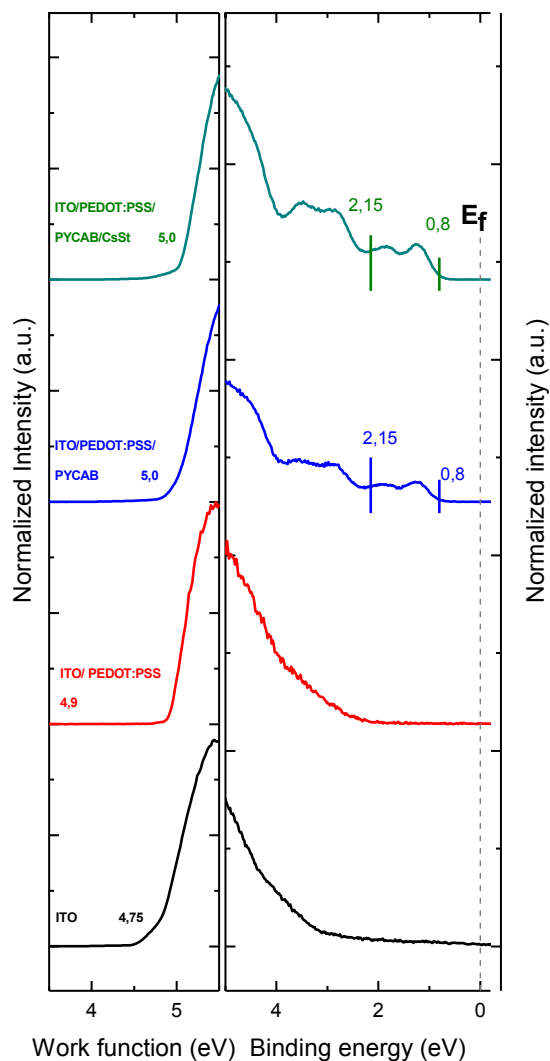


Figure 5.18: SECO (left) and valence region UPS spectrum (right) of ITO, ITO covered with PEDOT:PSS, PYCAB on top of PEDOT:PSS and CsSt on top of PYCAB.

5.3 Device performance of a dendrimer based light emitting diode utilizing cesium stearate aluminum (evaporated) double cathode

From these results only, one would suggest that either no CsSt is present on the sample, or that at least on the investigated region of the sample no CsSt was present. Taking a look at the XPS spectrum, that can measure the elemental composition of the investigated sample, clearly the cesium 4d peaks can be observed for the sample with CsSt on top. The XPS spectrum for the selected region is depicted in figure 5.19. According to this, an influence of the CsSt should be clearly visible in the UPS spectrum. Even though cesium stearate is an insulator, a charging of the device during the measurements can be excluded as the cesium stearate layer is inhomogeneous. Charging would negatively influence the measurements and therefore annihilate the expressiveness. Therefore in a next step the valence band region for the sample with and without cesium stearate was investigated in more detail. This is depicted in figure 5.20.

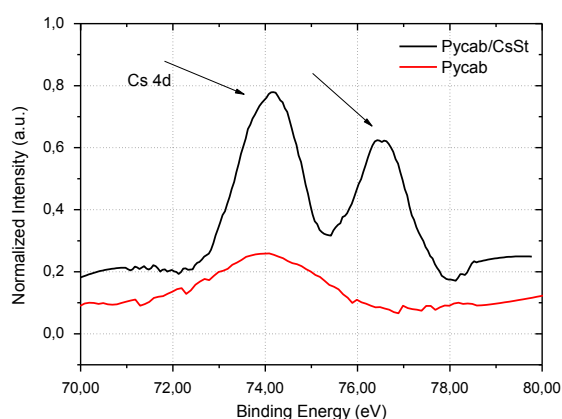


Figure 5.19: XPS spectrum (right) of PYCAB on top of PEDOT:PSS (red) and CsSt on top of PYCAB (black) in the region around 75 eV binding energy. The 4d peaks of Cesium are clearly visible.

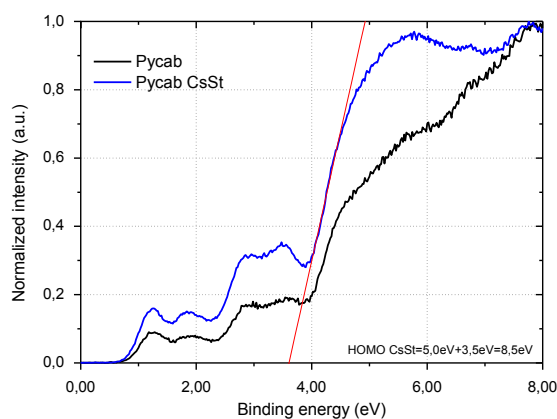


Figure 5.20: Direct comparison of the valence region UPS spectrum of PYCAB on top of PEDOT:PSS (black) and CsSt on top of PYCAB (blue).

5.3 Device performance of a dendrimer based light emitting diode utilizing cesium stearate aluminum (evaporated) double cathode

Now clearly a difference in the third peak in the valence band region is observable. This peak arises for the sample including a subsequent cesium stearate layer and therefore the ionization energy for CsSt was determined to be 8,5 eV. The high value measured for the ionization energy (8,5 eV) can be attributed to stearate according to literature [37]. An influence of the CsSt was not determined. This can either be explained by a decomposition of the CsSt on the surface, where the cesium dopes the active layer or by the high influence of the long hydrocarbon chain on the electronic behavior of the material. All together these measurements are in total contrast to the argumentation by Wetzelaer et al. [77]. They assumed that by using CsSt the electrode gets pinned to the LUMO of the active material [77]. Due to the extremely high LUMO for PYCAB of 1,7 eV (calculated from the absorption of the material) and the work function of the aluminum electrode (about 4,2 eV) the injection barrier for the electrons is very high. This explains perfectly why the device onset was increased dramatically in the case of PYCAB multilayer devices using cesium stearate (see figure 5.16 for more details). Also the better efficiency for the device using PEG-PF is explained easily by the more appropriate location of the PEG-PF LUMO. Moreover, the relatively moderate onset increase when combining ADS232 and CsSt is explained due to these results, as the LUMO of ADS232 is located lower than the LUMO of PYCAB. The good efficiency results for all devices using CsSt can therefore be attributed to the good hole blocking functionality of CsSt.

5.4 Influence of cesium stearate on polyfluorene color stability

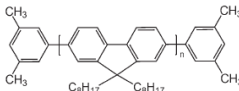
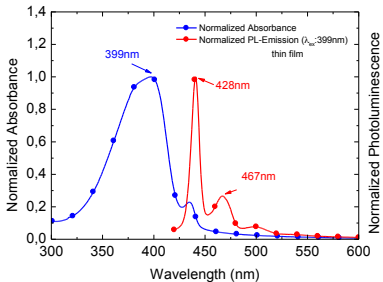
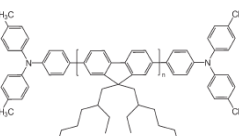
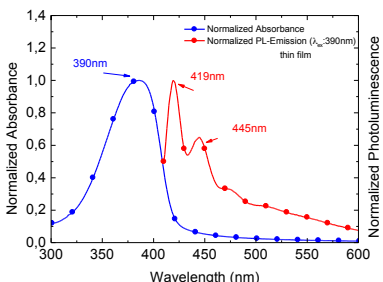
5.4.1 Different polyfluorene materials and there properties

Stable, easily produceable blue emitters with a reasonable luminance and lifetime are especially interesting for the display market. Especially blue emitters are known for their weaker lifetime performance [30]. In the case of polyfluorene devices, an interface induced green shift due to the incorporated oxygen during the cathode evaporation process [29] is known from literature. Besides this, also a device degradation under operation as a result of keto defect sides, which lead to a low energy emission band, is known for polyfluorene [58].

Therefore it can be concluded that a stable and long lasting blue emission is primarily a matter of the chemical stability of the device, but also influenced by the balanced charge carrier injection and a balanced transport of the charge carriers towards the active layer [51]. Moreover, an effective pinning of the recombination zone towards the center of the active layer is desirable [51]. As already mentioned previously, in the case of single layer devices incorporating cesium stearate the recombination zone is expected to be near the active layer cesium stearate interface. Even though this is not favorable, for the purpose of testing the influence of cesium stearate on the polyfluorene color stability, effects on the emission resulting for an anode side influence can be excluded. Keto defects are unlikely in this case, as they are more related to the active material, than to device assembly. In contrast, interface related defects in polyfluorene as reported by Gamerith et al. [29] are possible for cesium stearate. Therefore the behavior of devices with and without cesium stearate is investigated. The reference device was fabricated using calcium aluminum as cathode. Due to the good controlled evaporation process of the cathode on top of the active material, a behavior, as reported by Gamerith et al. [29] was not at all observed for the reference devices.

Several blue emitters based on polyfluorene were investigated, thereby it was investigated if the polymer design has an influence on the cesium stearate polyfluorene interaction. The chemical structure, absorption and photoluminescence spectra of the investigated devices are summarized in table 5.6.

Table 5.6: Summary of the investigated polymer materials and their main properties.

Polymer (short name)	Chemical structure	Normalized Absorption and normalized PL-Emission of a thin polymer film on quartz solution in THF
Poly[9,9-dioctylfluorenyl-2,7-diyl] - End capped with Dimethylphenyl (ADS129)		
Poly[9,9-di-(2-ethylhexyl)-fluorenyl-2,7-diyl] - End capped with N,N-Bis(4-methylphenyl)-aniline (ADS331)		
Poly[(9,9-dioctylfluorenyl-2,7-diyl)-co-(4,4'-(N-(p-butylphenyl)) diphenylamine)] (ADS259) (TFB)	see figure 3.5	see figure 3.7

5.4.2 Device performance for the different polymers utilizing cesium stearate aluminum (evaporated) double cathode

ADS129

First a standard polyfluorene with dimethylphenyl end caps was investigated. The actual device data are depicted in figure 5.21. When comparing the device incorporating cesium stearate at the electrode (right side) with the reference device (left side) a tremendous change in the electroluminescence emission spectra is observable (figures at the bottom). Moreover, an increased device efficiency, the reduced current density and increased luminance for the device using cesium stearate are noticeable. As a result of the extreme change in the device color upon changing the bias voltage, an adequate comparison of the device results is not possible. A good impression about the observable color change upon increased bias voltage is depicted in figure 5.22, where

images of an OLED under operation with increased bias voltage (increasing from the left to right side) are shown.

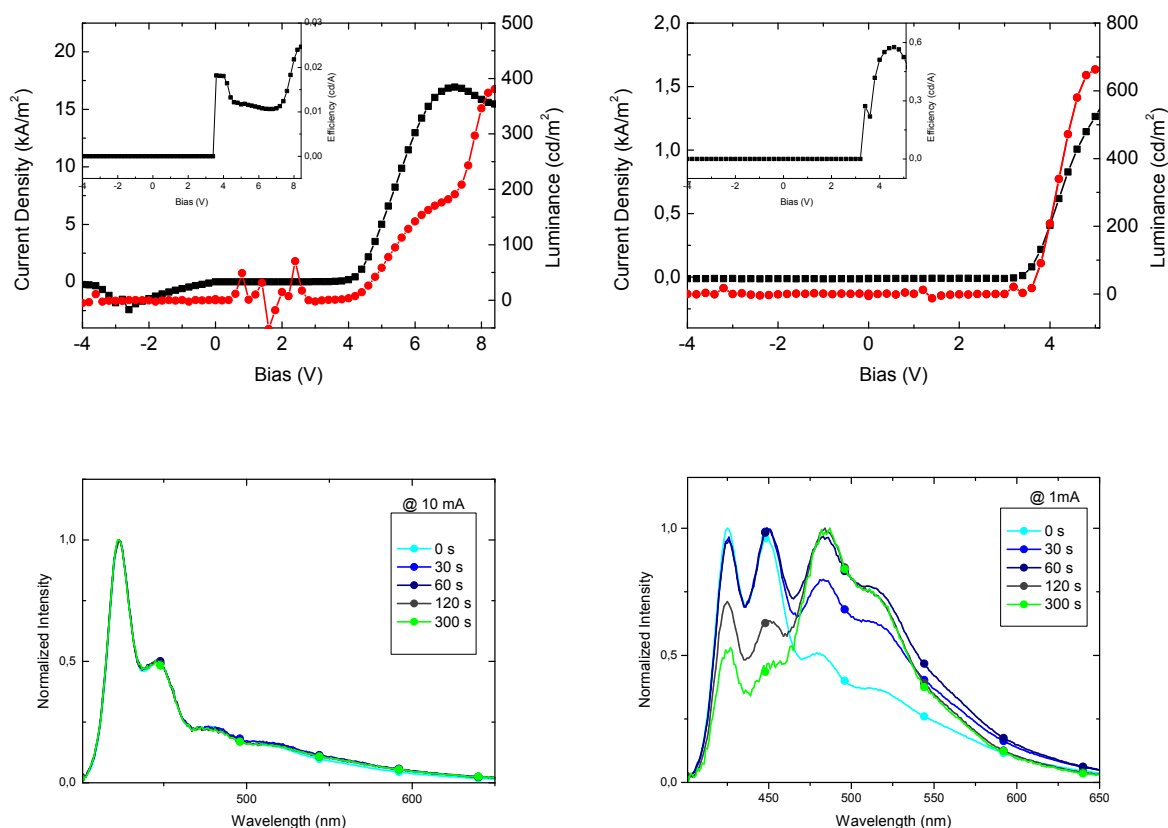


Figure 5.21: Current density (black) / luminance (red) as a function of the bias voltage in an ITO/PEDOT:PSS/ADS129/Ca/Al device (top left) and an ITO/PEDOT:PSS/ADS129/CsSt/Al device (top right). The insets show the device efficiencies as a function of the bias voltage. The corresponding electroluminescence emission spectra of the devices at a constant current density measured over 5 minutes continuous operation are shown at the bottom (Ca/Al cathode - bottom left; CsSt/Al cathode - bottom right). The applied current is written inside the individual graphs.

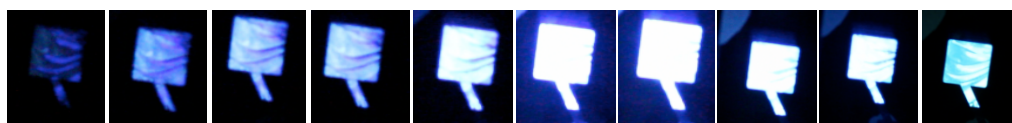


Figure 5.22: Images of an OLED with ADS 129 as active material and cesium stearate as cathode interlayer under operation. The applied voltage was increased, with lowest applied voltage on the left side of the image.

Gamerith et al. attributed the emission interface related defects to an oxidative degradation of the polymer due to interaction of residual oxygen and the metal electrode [29], a comparable situation

is possible for the polyfluorene cesium stearate interface as well.

ADS331

ADS331 was investigated together with cesium stearate in the single layer approach in order to systematically analyze whether or not the color change at the polyfluorene cesium stearate interface is a result of an oxidative degradation process, as described previously. Therefore ADS331 with the branched alkyl chains at the 9,9 position of the polyfluorene as well as the N,N-Bis(4-methylphenyl)-aniline end caps as steric hindrance units was chosen. A preferred reaction between the incorporated nitrogen and the residual oxygen from the cesium stearate is expected. Moreover, the interaction between the polyfluorene unit and the residual oxygen is expected to be reduced by the steric hindrance units. As depicted in figure 5.23, the introduction of steric hindering units is a successful way to reduce the interaction between the polyfluorene and the cesium stearate interlayer and therefore only small changes in the spectral behavior were observed. When comparing the corresponding electroluminescence emission spectra (left for the reference device and right for the device incorporating cesium stearate), an increased background as well as evolving peaks at 445 nm, 475 nm and 507 nm are observable. These are known peak positions of interface related defects, see Gamerith et al. [29]. Comparing the current density as well as the luminance characteristics, an extreme increase for both values was observed when cesium stearate was used. Due to the changed device color, the actual device results can not be compared adequately. Nevertheless an extremely reduced maximum current density (from 12 kA/m² to 1,13 kA/m²) for the device using cesium stearate instead of calcium indicates once more the good hole blocking functionality of cesium stearate.

ADS259

In order to investigate the influence of cesium stearate on copolymers including fluorene-copolymer the single layer device behavior of ADS259 was observed and compared with a standard device with Ca/Al cathode. The hole transport material ADS259 or better known as TFB, the chemical structure is depicted in figure 3.5, was already previously introduced. A stable emission without any changes of the device color was already shown for the fluorene-copolymer ADS232, the same behavior was expected in this case as well as TFB has no endcaps at all. The actual device data is depicted in figure 5.24. The current density and luminance values of the reference device are depicted on the top left position, the corresponding electroluminescence emission spectrum of the devices at a constant current are shown in the picture on the left bottom of figure 5.24, the same

5.4 Influence of cesium stearate on polyfluorene color stability

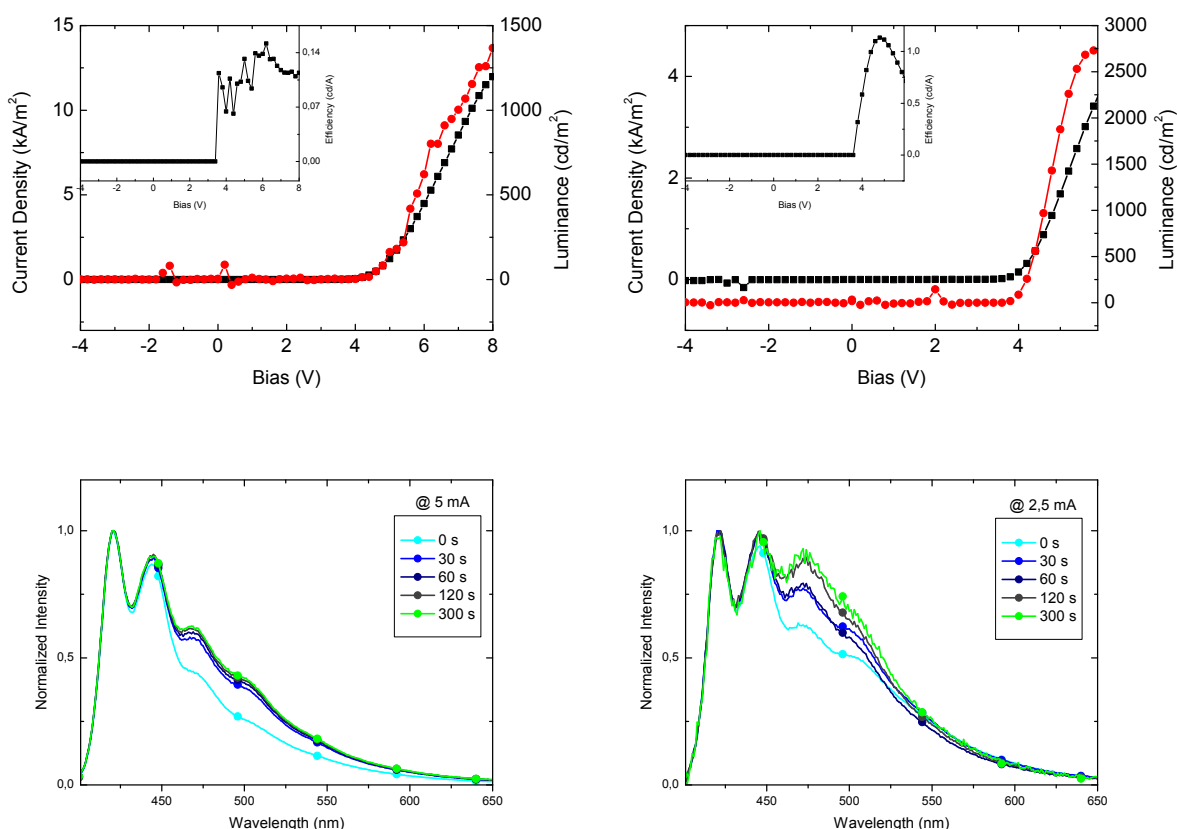


Figure 5.23: Current density (black) / luminance (red) as a function of the bias voltage in an ITO/PEDOT:PSS/ADS331/Ca/Al device (top left) and an ITO/PEDOT:PSS/ADS331/CsSt/Al device (top right). The insets show the device efficiencies as a function of the bias voltage. The corresponding electroluminescence emission spectra of the devices at a constant current density measured over 5 minutes continuous operation are shown at the bottom (Ca/Al cathode - bottom left; CsSt/Al cathode - bottom right). The applied current is written inside the individual graphs.

data for the single layer device replacing calcium by cesium stearate are shown on the right side of figure 5.24. When comparing the device data, two things are eye-catching, first the extremely increased luminance when cesium stearate is used and second that the emission spectrum is equal for both devices with a slightly increased background for the device using cesium stearate as interlayer.

In detail, the onset is in the same range for both devices, in contrast, the maximum luminance in contrast increases by a factor of 17 (from 192 cd/m² to 3265 cd/m² for the device using cesium stearate instead of calcium). Moreover, also the maximum current density is reduced from 14,5 kA/m² to 7,71 kA/m², which is still a relatively high value. This can be explained by

the unbalanced charge carrier injection, as TFB is normally well known as a good hole injection material rather than an active material.

According to the influence of cesium stearate on the device emission of TFB, it can be summarized that polyfluorene-copolymers like TFB are not sensitive to cesium stearate. Reasons here fore can be the different steric behavior of the copolymer compared to the bare polyfluorene. Another reason could be the high amount of nitrogen in the copolymer backbone, which would promote a reaction of the oxygen, incorporated into the CsSt and the nitrogen, incorporated into the copolymer backbone and therefore prohibit an oxidative degradation of the polymer due to a interaction of residual oxygen [29].

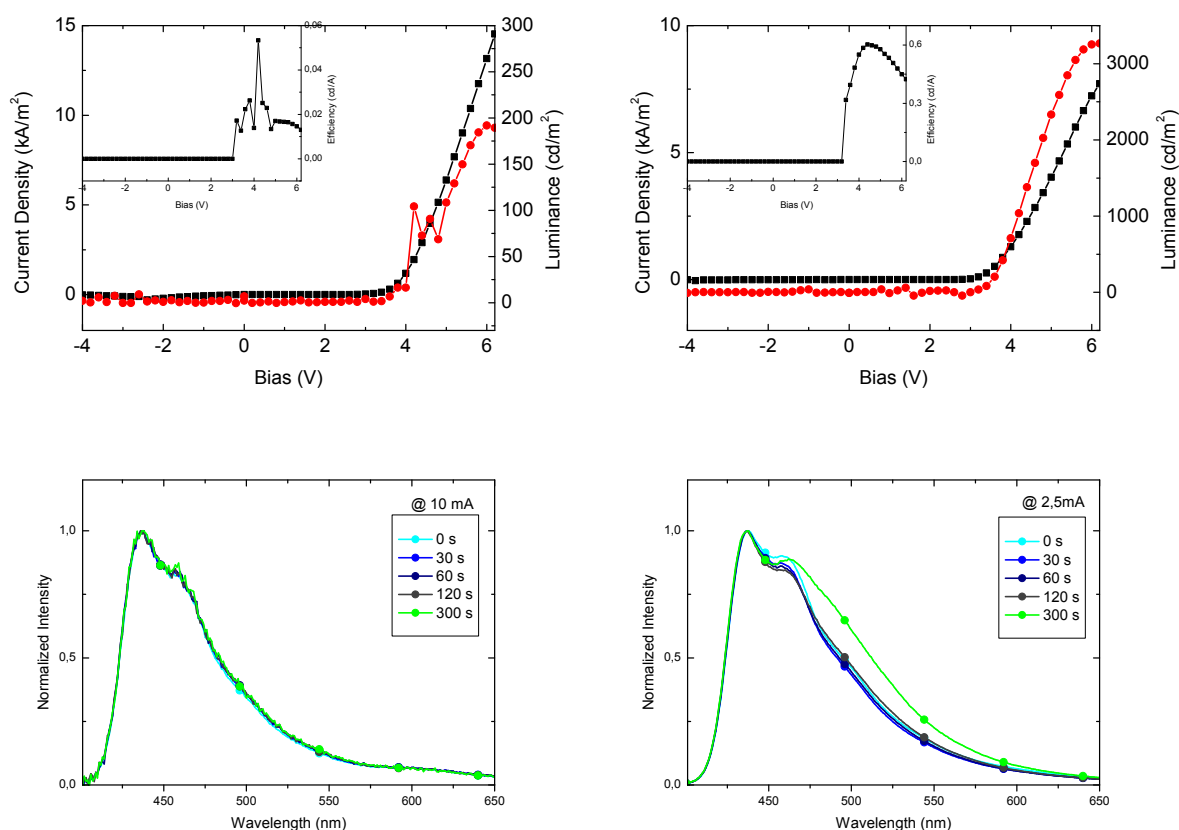


Figure 5.24: Current density (black) / luminance (red) as a function of the bias voltage in an ITO/PEDOT:PSS/ADS259/Ca/Al device (top left) and an ITO/PEDOT:PSS/ADS259/CsSt/Al device (top right). The insets show the device efficiencies as a function of the bias voltage. The corresponding electroluminescence emission spectra of the devices at a constant current density measured over 5 minutes continuous operation are shown at the bottom (Ca/Al cathode - bottom left; CsSt/Al cathode - bottom right). The applied current is written inside the individual graphs.

5.5 Conclusion

In general this chapter focused on a possible solution based cathode fabrication. The central material used for this purpose was cesium stearate. This material choice was motivated by the work of Wetzelaer et al. [77] where CsSt was introduced as a non-toxic solution processed cesium electrode material with a low work function. In a first approach, the layer formation of a 2g/l solution in ethanol was investigated. It was found that cesium stearate forms a flake like layer. The individual flakes have an approximate height of 10 nm and are likely to stack on top of each other, especially when the layer was formed with a slow spin speed.

In order to investigate the influence of cesium stearate on the device performance, single layer devices with cesium stearate were fabricated. These devices then were benchmarked using a standard cathode (calcium/aluminum). The active layer in this case was a polyfluorene-copolymer. For this material a slightly increased onset was measured. More importantly an extreme increase of the maximum device efficiency was observed as well (from 0,180 cd/A to 0,460 cd/A). Also for the device performance on flexible substrates, satisfying results were recorded. In a multilayer approach, the onset was slightly decreased whereas the maximum device efficiency was increased up to 0,829 cd/A. All important device parameters are summarized in table 5.1. The corresponding efficiencies are summarized in table 5.2 for the single layer devices and table 5.3 for the multilayer devices. These results clearly exhibit the positive effect of cesium stearate on the device performance and efficiency. From these results the primary mechanism for this enhanced device performance is not clear. To sum up these first results, the positive effect of cesium stearate on the device performance as already presented by Wetzelaer et al. [77], was also observed for ADS232 as active material. Even though the measured efficiency increase can not be explained reliably, an additional hole blocking mechanism is expected, especially when taking a close look at the multilayer device results.

Moreover, also a new dendrimer material consisting of a pyrene core and a carbazol surface group (PYCAB) was investigated in combination with cesium stearate. Here again, the device performance with and without cesium stearate in a single and multilayer approach was investigated. Again an efficiency enhancement was observed. In addition, the onset increased dramatically when cesium stearate was used on the cathode side (from 6 V up to 10 V in the multilayer device). To investigate this issue further, UPS measurements were carried out. There no electrode pinning of the LUMO, as suggested by Wetzelaer et al. [77] was observed. Instead the ionization energy of CsSt was found to be extremely high (8,5 eV). Combined with the extremely low LUMO of PYCAB, the high onset as well as the bad device performance can be explained by bad electron

injection. The efficiency enhancement is therefore a result of the good hole blocking functionality of CsSt. Besides this, also the time dependent behavior of PYCAB with and without CsSt was observed and it was found to be completely stable over a 5 minutes investigation.

In addition, the influence of cesium stearate on the color stability of several blue emitters based on polyfluorene were investigated. It was found that polyfluorene-copolymers are not influenced by the subsequent cesium stearate layer on top. In contrast, for bare polyfluorene (ADS129), a tremendous change in the electroluminescence emission spectra was observable. Systematically it was found that steric hindering units as well as the incorporation of nitrogen in the polymer backbone, reduce the influence of the CsSt layer on the emission color of the device.

6 INKJET PRINTED TOP CATHODE

Combining solution processed PLED (polymer light emitting diodes) with an inkjet printed top cathode is a key issue towards an industrial based low cost large area fabrication of OLEDs. Therefore several issues need to be considered, most of them discussed in detail in the experimental section on inkjet printing. When the inkjet printed metal is deposited on top of the whole OLED device stack, the exposure of the active material to ambient conditions, the layer formation, the solvent permeation into the layers underneath [82] and the interplay between micro-sized particles and organic layers with layer thicknesses in the nanometer range [82] need to be considered additionally. Recently, Zheng et al. [82] published an all solution processed OLED. There they tackled the previously mentioned problem of solvent penetration by applying an additional buffer layer between the active material and the inkjet printed silver. Still in this case, the electron injection barrier between the active material and the silver cathode is extremely high. The same group also reported in 2007 [81] on the subsequent deposition of PFNR2 (poly[9, 9-bis(3'-(N,N-dimethylamino)propyl)-2,7-fluorene-alt-2,7-(9,9-dioctylfluorene)]) as electron transport layer and silver ink. There the silver ink was not inkjet printed but dropped on top. A combination of solution processed low work function materials with inkjet printed metals on top, in order to prevent the low work function materials from oxidation under ambient conditions, has not been fabricated yet. Here the promising solution processed cathode interlayer, cesium stearate, was combined with inkjet printed silver. Another presented attempt was the combination of evaporated cesium carbonate and inkjet printed silver. Despite the standard devices, silver was used as cathode material instead of aluminum, even though it has a higher work function, which is unfavorable. This follows the fact, that there is no suitable aluminum ink for inkjet printing available on commercial basis, but recently, a group of scientists at the technical research centre of Finland (VTT), see also[56], are working on this issue. The device fabrication as well, in comparison to a vacuum deposited top cathode is presented. Besides this, the several defects and challenges for this promising method are discussed, as well as an outlook for further work in this field is given.

6.1 Layer formation of the silver ink on top of the device stack

The critical part in the case of top cathode printing is that the silver printing process is performed on top of the whole stack. Therefore, at first the compatibility of the used ink and the device surface needs to be checked. The print head and silver ink described in the experimental section were used. All prints were performed using just one nozzle, during the printing process the substrates were heated to 60 °C, the used resolution for all top cathode printings was 800 dpi. As the main goal was to achieve a closed layer, the layer thickness of the top cathode was not a limiting factor, in contrast to the inkjet printing process as described in section 4. The used device configuration was an ITO coated glass substrate, coated with PEDOT:PSS as anode. The used active material was ADS232 spin coated from toluene. The device fabrication was carried out as described in section 3.1.3. Three different configurations were tested.

First the silver ink was printed on top of **ADS232 without an additional low work function layer**. The resulting layer formation is depicted in figure 6.1. ADS232 was spin coated from toluene, whereas the silver nanoparticle are diluted in a polar solvents. With this configuration, no proper film formation was achieved as the individual droplets did not coalesce.

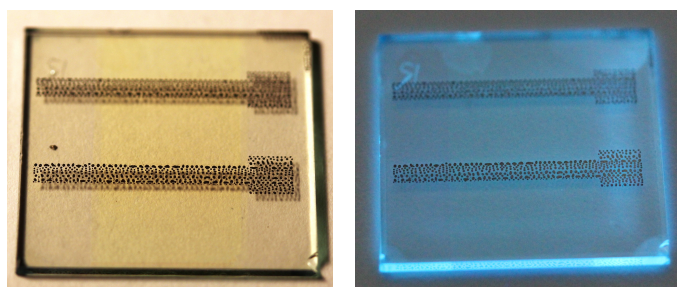


Figure 6.1: Test print of silver ink (Cabot CCI) on top of ADS232 (left), device illuminated with a UV lamp (right). The used process parameters are described in the text.

Next the layer formation of inkjet printed silver was tested on top of **ADS232 coated with an evaporated 5 Å layer of cesium carbonate (Cs_2CO_3)**. The combination of an evaporated layer underneath the solution processed silver was chosen because of the good electron injection behavior of a thin evaporated Cs_2CO_3 layer, see also [79], [31] and [51]. Again no proper film formation of the silver on top was achieved, as can be seen in figure 6.2. The thin noncontinuous layer of Cs_2CO_3 did not affect the surface tension to achieve a closed film formation.

Finally, the new solution processed cesium stearate was combined with the inkjet printed silver cathode in order to implement a fully solution processed bilayer top cathode. For this material combination a nicely homogeneous silver layer was achieved. The cesium stearate was, as

6.1 Layer formation of the silver ink on top of the device stack

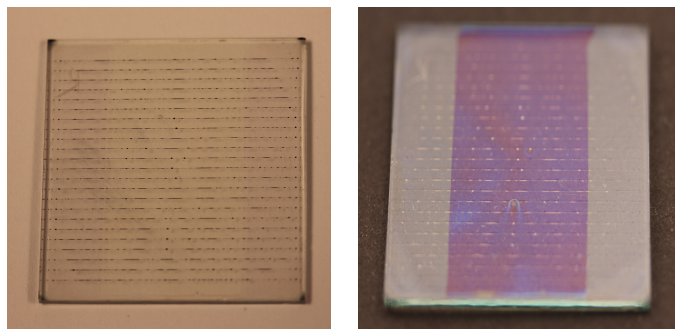


Figure 6.2: Test print of silver ink (Cabot CCI) on top of ADS232 and an evaporated 5 Å layer of cesium carbonate (Cs_2CO_3) (left), device illuminated with a UV lamp (right). The used process parameters are described in the text.

described previously, spin coated using ethanol as solvent. The test print for this case is depicted in figure 6.3. Even though the surface energy of plain ADS232 and **ADS232 spin coated with a cesium stearate layer** from ethanol solvent was measured to be nearly the same (33,93 mN/m respectively 30,15 mN/m), the layer formation was just accurate for ADS232 with CsSt on top. The influence of the flake size of the CsSt on top of the ADS232 polymer is assumed to be the reason for the divergence between surface tension measurements and layer formation of the silver ink. As no full coverage of CsSt was achieved, when CsSt was spin coated on top of the polymer, the values for the surface tension measurements are still highly influenced by the polymer layer underneath. That CsSt was spin coated from polar solvent and the silver nanoparticles are dissolved in a polar solvent as well, is maybe a second advantageous element for good film formation.

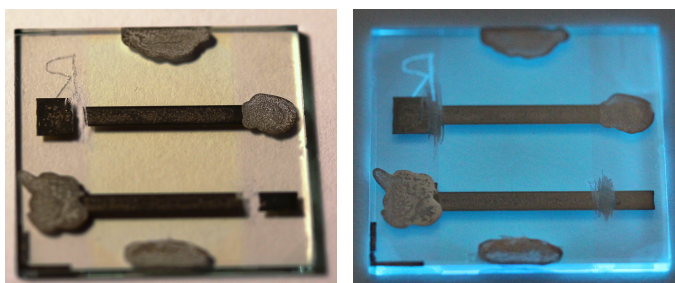


Figure 6.3: Test print of silver ink (Cabot CCI) on top of ADS232 and spin coated CsSt from ethanol solution (left), device illuminated with a UV lamp (right). The used process parameters are described in the text.

6.2 Device performance utilizing a fully solution processed bilayer top cathode with cesium stearate and silver

Because of the satisfying film formation of the silver ink on top of the ADS232 polymer spin coated with a cesium stearate layer, the device performance of OLEDs with such a cathode configuration was tested. To guarantee a good hole injection, on the anode side TFB was applied as an additional hole transport layer. The TFB layer was fabricated as described in the experimental section.

6.2.1 Influence of different curing conditions

First the influence of different curing conditions on the device performance was evaluated. According to the supplier [5], good adhesion and low resistivity of the inkjet printed silver can be produced by curing temperatures of 200 °C or above. During this baking step, the remaining solvent is removed and the silver nanoparticles sinter together. At our group we got good results by curing glass substrates at 200 °C for 2 h under inert atmosphere. As solution processing is a good method for the application on flexible substrates, lower curing temperatures were chosen this time.

Therefore two samples were fabricated identically, only the baking temperature was modified, using 150 °C for 2 h at inert atmosphere once and 100 °C for 2 h at inert atmosphere for the second sample. Microscope pictures of the two samples are depicted in figure 6.4 and 6.5. Apparently the silver ink pattern cured at lower temperatures (left picture) is less homogeneous than the one cured at 150 °C.

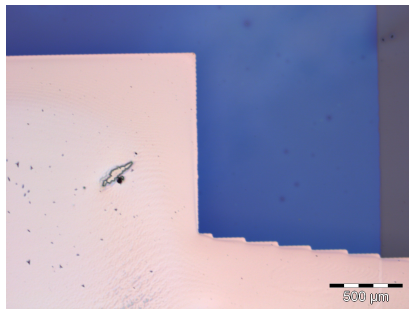


Figure 6.4: Microscope image of inkjet printed silver pattern cured at 100 °C for 2 h at inert atmosphere.

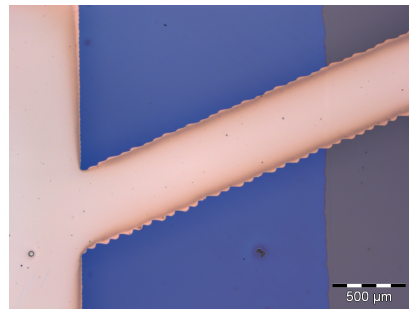


Figure 6.5: Microscope image of inkjet printed silver pattern cured at 150 °C for 2 h at inert atmosphere.

The U-I curves in the positive voltage range for different devices are shown in figure 6.6, a reference device with an evaporated aluminum layer is also added. For the device cured at higher

temperatures, a diode-like U-I characteristic can be observed, whereas for the device cured at 100 °C the electrical characteristic shows a nearly linear behavior. In the insert a picture of the device cured at 150 °C under operation is depicted. A low and inhomogeneous emission can be observed, the center of the device shows a poorer performance than the edges. The device size of 10 mm² and the higher ink amount at the center of the device, and a corresponding higher solvent amount, lead to a thicker silver film in the center. The solvent evaporation is slowest in the device center. According to the taken picture and following the quoted argumentation, the silver sheet resistance is highest in the center of the device. The U-I curves in figure 6.6 prove, that the device performance is best for the device with the higher curing temperatures. Following these results, the other samples with inkjet printed silver top cathode were cured at 150 °C for 2 h under inert atmosphere.

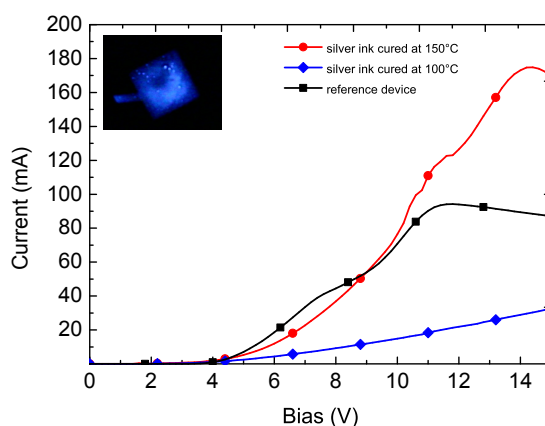


Figure 6.6: U-I curve of identically fabricated devices with different silver ink curing temperatures. The blue line represents the silver pattern cured at 100 °C for 2 h at inert atmosphere, red is the the silver pattern cured at 150 °C for 2 h at inert atmosphere. The device results are compared to a reference device with an evaporated aluminum cathode (black); insert: device cured at 150 °C under operation.

As both samples exhibited low luminance, the photocurrent was not measurable in both cases. The electroluminescence was detectable by cooling the CCD down to -50 °C and integrating the signal over a long time (some seconds). A device efficiency was not determined, as no photocurrent was measured. The corresponding electroluminescence spectrum as well as a standard spectrum for the same device stack with an evaporated aluminum layer are shown in figure 6.7. According to reference devices with the same device stack but an evaporated aluminum layer on top, the spectra are broadened and for the lower curing temperature even shifted towards higher wavelength. The red shift could be a result of the non fully evaporated solvent of the silver printing process. The cesium stearate layer is noncontinuous, therefore an interaction between the remaining solvent and the active layer is possible.

6.2 Device performance utilizing a fully solution processed bilayer top cathode with cesium stearate and silver

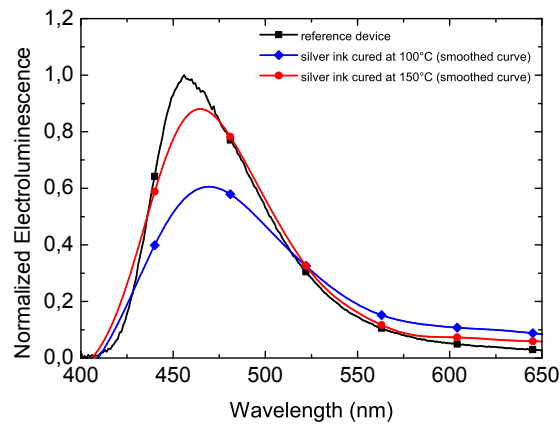


Figure 6.7: Electroluminescence spectra of identically fabricated devices with different silver ink curing temperatures. The silver pattern cured at 100 °C for 2 h at inert atmosphere (blue) and the silver pattern cured at 150 °C for 2 h at inert atmosphere (red) are compared to a reference device with an evaporated aluminum cathode (black).

The silver height on top of the device stack was measured to be about 900 nm. The measured profile is depicted in figure 6.8. The insert of figure 6.8 shows the exact region where the ink profile was measured. As already illustrated, the height of the silver print reduces towards the edges. Due to the thickness of the cured silver layer relative to the active layer thickness of about 50-60 nm, the solvent penetration for the active layer underneath is estimated to be immense and therefore the main reason for the poor device performance.

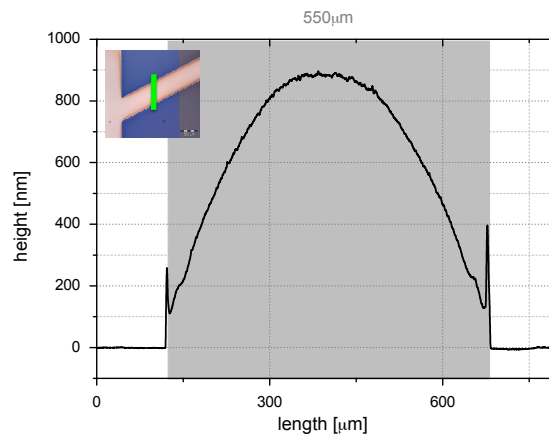


Figure 6.8: Height profile of the inkjet printed silver cured at 150 °C on top of the device stack, the insert shows the exact place where the height profile was measured.

6.2.2 Reduced solvent penetration of the active layer using a smaller top cathode patterning

In order to reduce the solvent penetration for the active layer, the design of the top cathode was modified. Instead of 8 devices with an active layer size of 10 mm^2 each, several thin lines were printed on top and afterwards connected together using conductive silver. In figure 6.9 on produced sample is depicted. The figure right shows the sample after the printing process, the left figure shows the sample including the electrode contacts. The summarized active layer was determined to be in the range of $10\text{-}12 \text{ mm}^2$ depending on the individual number of included lines. As the lines were printed on a one dot basis, the solvent penetration is estimated to be extremely reduced. One identification for this is the reduced cathode height of approximately 500 nm , measured again using a profilometer. The linewidth of one individual line was measured to be approximately $100 \text{ }\mu\text{m}$.

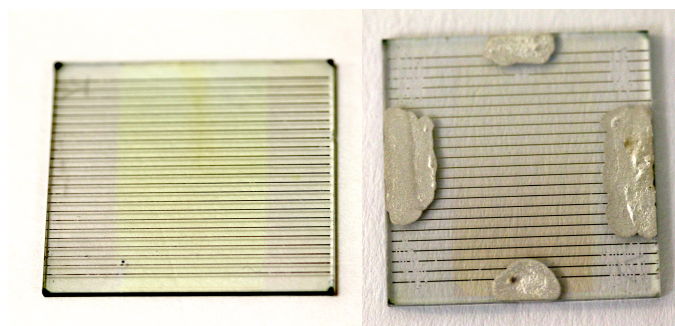


Figure 6.9: Image of an sample with line structured top cathode (right), image of the lines structured sample including electrode contacts (left).

When measuring the device characteristics, nonuniform electroluminescence was observed. An image of a device under operation is depicted in the center of figure 6.10. The printed silver lines were also analyzed using an optical microscope. The individual images for the center and edge region are also depicted in figure 6.10. In the center region of the line structures, a bumpy silver surface was observed. This was estimated to be a result of the chosen curing process and a result of an insufficient sintering process of the individual silver nanoparticles. For one individual line a resistance of $20 \text{ M}\Omega$ was measured at 10 V a direct evidence, for the bad conductivity of the silver lines. Therefore no electrical characteristic of the device with a line structured top cathode is presented. Nevertheless, one can conclude that the reduction of the solvent penetration for the active layer does not influence the device behavior in a positive way, due to the bad conductivity of printed silver on top of the device.

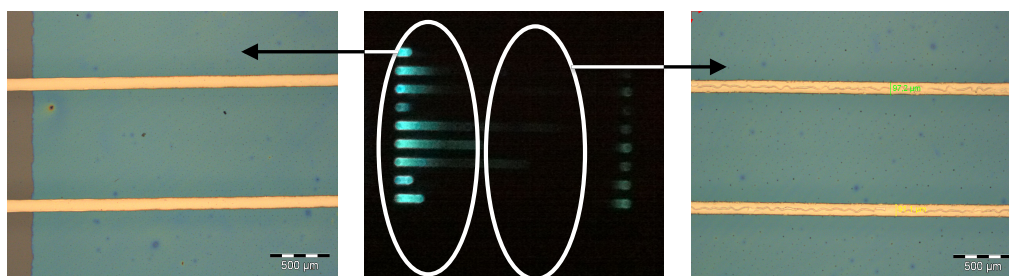


Figure 6.10: Image of a sample with line structured top cathode under operation (middle) and microscope images of the silver lines on the edges (left) and in the center (right).

6.3 Conclusion

Within this section the combination of spin coated cesium stearate with an also from solution processed cathode was presented. It was found that a continuous layer formation of the silver cathode on top of ADS232 is possible only if cesium stearate is spin coated underneath. A possible reason therefore is the compatibility of the used solvents. Both, the cesium stearate and the silver ink are present in polar solvents. Proving this by measuring the surface energy of the device with and without cesium stearate failed. Actually the received values were nearly identical. Due to a noncontinuous CsSt layer, the expressiveness of the surface energy results is unclear. Moreover the influence of the curing temperature was analyzed. After the inkjet printing, this step is necessary to remove the residual solvents. Two curing temperatures beneath the glass transition temperature for PET were tested, better device results have been observed for the higher curing temperature (150 °C). In general, the device results were quite poor. Possible reasons known from literature are the solvent penetration for the active layer, the residual solvent that did not vanish during the curing step and bad arrangement of the nanoparticles and therefore bad layer formation. Moreover the ambient conditions during the inkjet printing process are suboptimal. In order to reduce the solvent penetration into the active layer, a different top cathode design was tested as well. Several thin lines were printed and interconnected in order to have the same active device size. Unexpectedly, the device results were even worse. The reason therefore was the low conductivity of the inkjet printed silver. Summarizing this, using some sort of a smooth buffer layer between the active layer and the top cathode seems to be the most promising option. Besides this, also the surface energy of the buffer layer needs to fit the used silver ink. Using a laser curable ink is maybe another possibility, as the glass transition temperature would no longer be a limiting factor.

7 CONCLUSION

The scope of this thesis was the investigation of solution processed electrode materials on flexible substrate. On the anode side the technical realization on inkjet printed silver as a conductivity enhancing grid was carried out. The varying height profile of the printed grid was reduced using a transparent trench system. On the cathode side, a relatively new material was thoroughly investigated in terms of layer formation, compatibility with printing processes and various solution processed blue emitters including a new dendrimer material. In addition the electron structure was investigated using UPS.

At first the technical realization of inkjet printed silver as a conductivity enhancing grid was tested. In first tests evaporated grids with a height of 100 nm were combined with a conductive polymer and bench marked with ITO. For devices using evaporated small molecules as active layer a better efficiency (1,65 cd/A instead of 1 cd/A) was achieved than for ITO. The efficiency enhancement was found to be a direct result of the better charge carrier balance. The positive effect the grid had on the hole injection, was tested using a solution processed conjugated polymer materials as active layer. Comparing the bare conductive polymer with the same setup supported by the evaporated silver grid, a large increase in the efficiency was observed. Here, the better hole injection was found responsible for the increasing of all important device parameters. Ink jet printing silver grid on top of rigid sample as well as flexible substrates was carried out. The print profile was found highly influenced by the carrier substrates. Optimizing the inkjet printed grid a minimal grid height of 370 nm was measured. On PEN foil the minimal grid height was even more than 700 nm. In order to further process an OLED on top of this grid, the silver grid was additionally embedded. The thick positive chemically amplified photo resist AZ[®] was found to be a good embedding material, that is perfectly transparent in the optical range. The silver ink was then directly printed into the transparent trenches and a clear reduction of the average line height was investigated. However the fine tuning is still tricky and undesired "edge effects", as a result of the forces of the silver ink, are negatively influencing the printing behavior. Nevertheless this easy and straight forward embedding idea seems to be a clever way to implement ink jet printed silver grids in full devices.

In the next chapter cesium stearate was investigated as low work function cathode interlayer. This material was first used for OLED's by Wetzelaer et al. Analyzing the layer formation an uncontinuous flake like film of cesium stearate was found, with an approximate height of 10 nm for an individual flake. In order to investigate the influence of cesium stearate on the device performance, single and multilayer device using a polyfluorene-copolymer as active material were fabricated and investigated. For all devices incorporating CsSt instead of calcium, a better device efficiency was observed for the multilayer device the efficiency was increased up to 0,829 cd/A. Moreover also a new dendrimer material consisting of a pyrene core and a carbazol surface group (PYCAB) was investigated in combination with cesium stearate. Here again an efficiency enhancement was observed, besides this also a dramatically increased onset was measured (from 6 V up to 10 V in the multilayer device). To investigate this issue further UPS measurements were carried out. There the ionization energy of CsSt was found to be extremely high (8,5 eV), whereas the Pycab LUMO was measured to be extremely low. So the high onset can be explained by the bad electron injection and the efficiency enhancement is a result of the good hole blocking functionality of CsSt. Therefore it can be concluded, that cesium stearate is not a good low work function material but rather a good hole blocking material. In addition the influence of cesium stearate on the color stability of several blue emitters based on polyfluorene were investigated. It was found that polyfluorene-copolymers are not influenced by cesium stearate. The emission spectra of bare polyfluorene (ADS129) was total green shifted when CsSt was used in combination. Systematically it was found, that steric hindering units, as well as the incorporation of nitrogen in the polymer backbone, reduce the influence of cesium stearate on the emission color.

Finally spin coated cesium stearate was successfully combined with inkjet printed silver on top. Actually it was found, that a continuous silver layer was only formed, when cesium stearate was applied in combination. Besides this, the influence of the silver curing temperature on the device performance was investigated. Two curing temperatures beneath the glass transition temperature for PET were tested, the better device performance was archived for the higher curing temperature. Generally, the device results were quiet poor. By testing a smaller cathode structure the influence of the solvent penetration for the active layer was systematically analyzed. The reduced silver height also had a negative effect on the conductivity of the cathode. Moreover the ambient conditions during the inkjet printing process are critical. A stable and reproducible fabrication was not possible, due to the negative effects of the inkjet printed silver and the process conditions on the active material. In a further approach a buffer layer should be insert between the active layer and the cathode.

Bibliography

1. <http://oelectronics.weebly.com/organic-semiconductors.html> (accessed Feb11, 2014).
2. <http://wps.prenhall.com/wps/media/objects/724/741576/chapter01.html> (accessed Mar12, 2014).
3. <http://reefkeeping.com/issues/2006-05/sj/images/tnimage012jpg.jpg> (accessed Feb25, 2014).
4. <http://www.aglycon.at> (accessed Jan28, 2014).
5. <http://www.cabot-corp.com/wcm/download/en-us/nb/ATTH4YZ5.doc> (accessed Jan12, 2014).
6. <http://www.dupont.com/> (accessed Jan15, 2014).
7. Aernouts, T., Vanlaeke, P., Geens, W., Poortmans, J., Heremans, P., Borghs, S., Mertens, R., Andriessen, R. & Leenders, L. *Thin Solid Films* **451-452**, 22–25 (2004).
8. Ahlswede, E., Muhleisen, W., Wahi, M. W. b. M., Hanisch, J. & Powalla, M. *Appl. Phys. Lett.* **92** (2008).
9. Alzoubi, K., Hamasha, M. M., Lu, S. & Sammakia, B. **7**, 593–600 (2011).
10. Angmo, D. & Krebs, F. C. *J. Appl. Polym. Sci.* **129**, 1–14 (2013).
11. Auer, M. *Studies of Novel Polymer and Dendrimer Materials for Application in Organic Light Emitting Devices* MA thesis (Technische Universität Graz, 2013).
12. Burroughes, J. H., Bradley, D. D. C., Brown, A. R., Marks, R. N., Mackay, K., Friend, R. H., Burns, P. L. & Holmes, A. B. *Nature* **347** (1990).
13. Cahen, D. & Kahn, A. *Adv. Mater.* **15**, 271–277 (2003).
14. Cairns, D. R., Paine, D. C., Crawford, G. P. & Kukureka, S. N. *SID Symp. Dig. Tech. Pap.* **32**, 654 (2001).
15. Chang, Y., Wang, L. & Su, W. *Org. Electron.* **9** (2008).
16. Chen, M.-H. & Wu, C.-I. *J. Appl. Phys.* **104**, 113713 (2008).
17. Choi, H. W., Kim, S. Y., Kim, W.-K. & Lee, J.-L. *Appl. Phys. Lett.* **87**, 082102 (2005).
18. Condon, E. *Phys. Rev.* **32**, 858–872 (1928).

19. Do, H., Reinhard, M., Vogeler, H., Puetz, A., Klein, M. F., Schabel, W., Colsmann, A. & Lemmer, U. *Thin Solid Films* **517**, 5900–5902 (Aug. 2009).
20. Duan, L., Hou, L., Lee, T.-W., Qiao, J., Zhang, D., Dong, G., Wang, L. & Qiu, Y. *J. Mater. Chem.* **20**, 6392 (2010).
21. Duan, L., Member, S. I. D. & Xie, K. 453–461 (2011).
22. Einstein, A. *Annalen der Physik* **322**, 132–148 (1905).
23. Franck, D. E. G. *J. Trans. Faraday Soc.* **21** (1926).
24. Friend, R. *et al. Nature* **397**, 121–128 (1999).
25. Galagan, Y., Coenen, E. W. C., Zimmermann, B., Slooff, L. H., Verhees, W. J. H., Veenstra, S. C., Kroon, J. M., Jø rgensen, M., Krebs, F. C. & Andriessen, R. *Adv. Energy Mater.* **4** (2013).
26. Galagan, Y., Coenen, E. W., Sabik, S., Gortler, H. H., Barink, M., Veenstra, S. C., Kroon, J. M., Andriessen, R. & Blom, P. W. *Sol. Energy Mater. Sol. Cells* **104**, 32–38 (2012).
27. Galagan, Y., J.M. Rubingh, J.-E., Andriessen, R., Fan, C.-C., W.M. Blom, P., C. Veenstra, S. & M. Kroon, J. *Sol. Energy Mater. Sol. Cells* **95**, 1339–1343 (2011).
28. Galagan, Y. *et al. Adv. Energy Mater.* **2**, 103–110 (2012).
29. Gamerith, S., Nothofer, H.-G., Scherf, U. & List, E. J. W. *Jpn. J. Appl. Phys.* **43**, L891–L893 (2004).
30. Geffroy, B., le Roy, P. & Prat, C. *Polym. Int.* **55**, 572–582 (2006).
31. Hasegawa, T., Miura, S., Moriyama, T., Kimura, T., Takaya, I., Osato, Y. & Mizutani, H. *SID Symposium Digest of Technical Papers* **35**, 154–157 (2004).
32. Haskal, E. I., Curioni, A., Seidler, P. F. & Andreoni, W. *Appl. Phys. Lett.* **71**, 1151 (1997).
33. Huang, F., Wu, H. & Cao, Y. *Chemical Society Reviews* **39**, 2500–2521 (2010).
34. Huang, J., Li, G., Wu, E., Xu, Q. & Yang, Y. *Adv. Mater.* **18**, 114–117 (2006).
35. Huang, J., Xu, Z. & Yang, Y. *Adv. Funct. Mater.* **17**, 1966–1973 (2007).
36. Hung, L. S., Tang, C. W. & Mason, M. G. *Appl. Phys. Lett.* **70**, 152 (1997).
37. Inokuchi, H. & Seki, K. *Phys. Sricpta* **17**, 93–103 (1987).
38. Ishii, H., Sugiyama, K., Ito, E. & Seki, K. *Adv. Mater.* **11**, 605–625 (1999).
39. Kanitz, A., Patzold, R., Sarfert, W. & Suhonen, R. *U.S. patent 0085472* (2009).
40. Kasha, M. *Discuss. Faraday Soc.* **9**, 14–19 (1950).
41. Kim, J.-S., Friend, R. H., Grizzi, I. & Burroughes, J. H. *Appl. Phys. Lett.* **87**, 023506 (2005).

42. Kim, Y.-M., Yu, G.-C., Lee, T.-W. & Kim, Y. C. *Mol. Cryst. Liq. Cryst.* **491**, 109–113 (Sept. 2008).
43. Koch, N. *Phys. status solidi - Rapid Res. Lett.* **6**, 277–293 (2012).
44. Koren, K. *Synthesis and Characterization of Multifunctional Optical Sensor Particles* MA thesis (Technische Universität Graz, 2008).
45. Lean, M. H. & Chu, W.-P. L. *J. Phys. D. Appl. Phys.* **47**, 075303 (2014).
46. Li, Y., Zhang, D.-Q., Duan, L., Zhang, R., Wang, L.-D. & Qiu, Y. *Appl. Phys. Lett.* **90**, 012119 (2007).
47. Li, Y., Mao, L., Gao, Y., Zhang, P., Li, C., Ma, C., Tu, Y., Cui, Z. & Chen, L. *Sol. Energy Mater. Sol. Cells* **113**, 85–89 (2013).
48. Liu, H., Avrutin, V., Izyumskaya, N., Özgür, U. & Morkoç, H. *Superlattices Microstruct.* **48**, 458–484 (2010).
49. Marks, T., Veinot, J., Cui, J., Yan, H., Wang, a, Edleman, N., Ni, J, Huang, Q, Lee, P & Armstrong, N. *Synth. Met.* **127**, 29–35 (2002).
50. Martin, I. M. H. G. D. *Inkjet Technology for Digital Fabrication* (John Wiley and Sons, 2012).
51. Nau, S., Schulte, N., Winkler, S., Frisch, J., Vollmer, A., Koch, N., Sax, S. & List, E. J. W. *Adv. Mater.* **25**, 4420–4424 (2013).
52. Neyts, K., Real, A., Marescaux, M., Mladenovski, S. & Beeckman, J. *J. Appl. Phys.* **103**, 093113 (2008).
53. Niu, Y.-H., Liu, M. S., Ka, J.-W., Bardeker, J., Zin, M. T., Schofield, R., Chi, Y. & Jen, A. K.-Y. *Advanced Materials* **19**, 300–304 (2007).
54. Pauling, L. *J. Am. Chem. Soc.* **53** (1931).
55. Qin, T. *et al. J. Am. Chem. Soc.* **133**, 1301–3 (2011).
56. *Research and development activities in printed intelligence* tech. rep. (VTT TECHNICAL RESEARCH CENTRE OF FINLAND, 2006).
57. Sax, S., Rugen-Penkalla, N., Neuhold, A., Schuh, S., Zojer, E., List, E. J. W. & Müllen, K. *Adv. Mater.* **22**, 2087–2091 (2010).
58. Scherf, U. & List, E. J. W. *Adv. Mater.* **14**, 477–487 (2002).
59. Schlaf, R. <http://rsl.eng.usf.edu/Documents/Tutorials/TutorialsWorkFunction.pdf> (accessed Jan31, 2014).
60. Scott, J. C. *J. Vac. Sci. Technol. A Vacuum, Surfaces, Film.* **21**, 521 (2003).

61. Siemund, H., Bröcker, F. & Göbel, H. *Org. Electron.* **14**, 335–343 (2013).
62. Slawinski, M., Weingarten, M., Heuken, M., Vescan, a. & Kalisch, H. *Org. Electron.* **14**, 2387–2391 (2013).
63. Tang, C. W. & VanSlyke, S. A. *Appl. Phys. Lett.* **51**, 913 (1987).
64. Tomalia, D., Baker, H., Dewald, J., Hall, M., Kallos, G., Martin, S., Roeck, J., Ryder, J. & Smith, P. *Polym. J.* **17**, 117–132 (1985).
65. Trattnig, R., Jäger, M., Schlesinger, R. & Nardi, M. UPS measurements of serveral inks.
66. Trattnig, R. *Organic Light Emitting Devices based on Phosphorescent Organometallic Complexes in Blend- and Onchain Polymer Systems* MA thesis (Graz University of Technology, 2009).
67. Trattnig, R. *Solution Processed Organic Multilayer Devices for Light Emitting and Photovoltaic Applications* PhD thesis (Doktor Thesis, Graz University of Technology, 2013).
68. Trattnig, R. *et al. Adv. Funct. Mater.* **23**, 4897–4905 (2013).
69. Tseng, S.-R., Li, S.-Y., Meng, H.-F., Yu, Y.-H., Yang, C.-M., Liao, H.-H., Horng, S.-F. & Hsu, C.-S. *J. Appl. Phys.* **101**, 084510 (2007).
70. Tvingstedt, K. & Inganäs, O. *Adv. Mater.* **19**, 2893–2897 (2007).
71. (USGS)., U. G. S. <http://minerals.usgs.gov/minerals/pubs/commodity/indium/mcs-2012-indiu.pdf> (accessed Feb12, 2014).
72. Van de Wiel, H. J. *et al. Nanotechnology* **24**, 484014 (2013).
73. Wang, G., Jiu, T., Sun, C., Li, J., Li, P., Lu, F. & Fang, J. *ACS Appl. Mater. Interfaces* **6**, 833–8 (2014).
74. Wang, S. D., Fung, M. K., Lai, S. L., Tong, S. W., Lee, C. S., Lee, S. T., Zhang, H. J. & Bao, S. N. *J. Appl. Phys.* **94**, 169 (2003).
75. Wang, X., Zhi, L. & Müllen, K. *Nano Lett.* **8**, 323–7 (2008).
76. W.Brütting. *Physics of Organic Semiconductors* (WILEY-VCH Verlag GmbH and Co. KGaA, Weinheim, 2005).
77. Wetzelaer, G. A. H., Najafi, A., Kist, R. J. P., Kuik, M. & Blom, P. W. M. *Appl. Phys. Lett.* **102**, 053301 (2013).
78. Wohlgenannt, M., Tandon, K., Mazumdar, S., Ramasesha, S. & Vardeny, Z. *Nature* **409**, 494 (2001).
79. Wu, C.-I., Lin, C.-T., Chen, Y.-H., Chen, M.-H., Lu, Y.-J. & Wu, C.-C. *Appl. Phys. Lett.* **88**, 152104 (2006).

80. Xu, Q., Ouyang, J., Yang, Y., Ito, T. & Kido, J. *Appl. Phys. Lett.* **83**, 4695 (2003).
81. Zeng, W., Wu, H., Zhang, C., Huang, F., Peng, J., Yang, W. & Cao, Y. *Adv. Mater.* **19**, 810–814 (2007).
82. Zheng, H. *et al. Nat. Commun.* **4**, 1–7 (2013).
83. Zimmermann, B., Glatthaar, M., Niggemann, M., Riede, M., Hinsch, a. & Gombert, a. *Sol. Energy Mater. Sol. Cells* **91**, 374–378 (2007).